Ultra-Downsizing of DI hydrogen-fueled VCSR ICEs (H2-ICEs).

An Alternative to Fuel Cells EV (FCEV) and pure EV that is equally efficient, fully recyclable, inexpensive and significantly more reliable

Author Prof. PhD. ME Victor Gheorghiu
Affiliation RD4E & Hamburg University of Applied Sciences

Abstract

The Ultra-Downsizing (UD) is introduced here as an even higher stage of downsizing of ICEs. VCSR means Variable Compression and Stroke Ratios.

Ultra-Downsizing is implemented here by means of true Atkinson cycles using an asymmetrical crank mechanism (s. Appendix 1 and Appendix 2) with continuous (Volumetric Compression Ratio) **VCR** adapting capabilities, combined with two or more stages of high-pressure turbocharging and very intensive intercooling for pure GasDI-Hydrogen (or H2-CNG blends) fueled VCSR engines. This allow for an increase of ICE performance while keeping the thermal and mechanical strain strength of engine components within the current usual limits [1], [2].

The principal purpose of this investigation is to analyze, evaluate and compare the **ICE** with **VCSR** crank mechanism and **UD** Load Control (**LC**) to the actual classical **ICE**, the **FCEV** and pure **EV** as mobility drive systems. See [28] for R&D Milestones on VCSR ICE.

In the following, the thermodynamic and fluid dynamic processes from the cylinder of ICEs, which work according to the classic Seiliger and true Atkinson cycle will be presented and analyzed. By using an asymmetrical crank mechanism with continuously adapted **VCR** for load control (**LC**), it is possible to achieve the true-Atkinson cycles of turbocharged engines for part and full loads even when maintaining a stoichiometric **AFR** and without throttling or excessive **EGR** [1], [2]. In addition, by using a sequentially adapted hydrogen direct injection GasDI, s. Fig. 13, [8], s. 173, Fig. 6-20 and Fig. 14, [12], s. 26, Fig. 2.3, the raw NOx emissions can be diminished up to 95%. If the engine is also operated with stoichiometric AFR ($\lambda = 1$), the NOx emissions can be completely reduced, i.e. using a classic three-way catalytic converter for after-treatment.

Introduction

Reducing CO_2 emissions to limit global warming to less than 2 degrees Celsius by 2050 is the declared goal of all environmental organizations such as Fridays for Future, etc. Their participants are usually not sufficiently specialized or informed on those topics to be able to assess the rightness of their demands. [27], [29]
Friday for Future self-statement [see under FFFAQ]:
“We profoundly appreciate all efforts to find solutions to the climate crisis. Fridays for Future does not have the capacity or the competence to evaluate solutions. If you have a solution, we therefore urge you to send your contribution to those who do, so that it can be put to use.” Nevertheless, they outdo each other with proposals and demands for still more drastic measures to achieve climate targets! Anyway, they have an opinion, but opinion is not identical with expertise! Many politicians, e.g. the Greens, are surfing this wave for achieving their personal political goals!
One example is the **imaginary** finding of “**zero**” CO_2 emissions for **BEVs** (pure Battery **EV**) in the European Parliament and elsewhere. The European legislation falsely claims that the BEVs generate zero CO_2 emissions when in operation.
This setting is unachievable even for Norway, where electricity is generated almost emission-free with hydropower. The CO_2 emission from the production of vehicle and battery are deliberately ignored. In all other European countries and elsewhere, furthermore arise from charging batteries using the electricity from each country´s production mix of green energy and nuclear energy on the one hand and fossil fuels on the other, s. Fig. 1-6 to 1-8 & [6], [9].

The following facts are purposely ignored, [27]:

a) The worldwide raw material deposits for battery production are largely insufficient for broad-based electric mobility and for the storage of electrical energy from renewable sources sun and wind.

b) The extraction of raw materials for battery production pollutes and severely damages the environment in many poor regions of the world.

c) The processing of these raw materials for battery production is very energy-intensive and generates high CO_2 emissions at the production location.

d) An efficient and effective recycling rate, i.e. of more than 90% of the materials from used batteries has not yet been reached. The current processes are, like battery production, very energy-intensive and produce non-recyclable chemical end products.

e) Because of the high dead weight and lower power density, electric drives are actually unsuitable for trucks, locomotives, ships, air cabs, airplanes etc. As example, Andreas Renschler, a former Traton chairperson and VW board member, said: "There fully electric drive is not yet feasible for certain truck types. If you want to operate a large concrete mixer with batteries, it has to carry so many tons of batteries that there is not much weight left for the concrete. For the near future, the electric drive will not be economically feasible for such applications. Alternatively, take the heavy refuse trucks. They can be fully electric within the city, but our customers say: That's all well and good, but if the final destination for the garbage is 80 kilometers away, should we reload at the city limits?” FAS [71].
These briefly mentioned facts are presented, explained and evaluated in detail below.

Comparison and Evaluation of Alternatives to Sustainable Mobility

Zero or at least low CO_2 emissions can be achieved in the following three variants (s. also the legend of Figure 0):

1. VCSR ICE with UD LC vehicles
2. FCEV Fuel Cell Electrical Vehicles
3. EV pure Electrical Vehicles

These three variants are very different and therefore difficult to compare. Nine criteria are considerate below in order to be able to compare these variants. The results of this comparison are evaluated and presented in the form of a spider/radar diagram, s. Fig. 0.

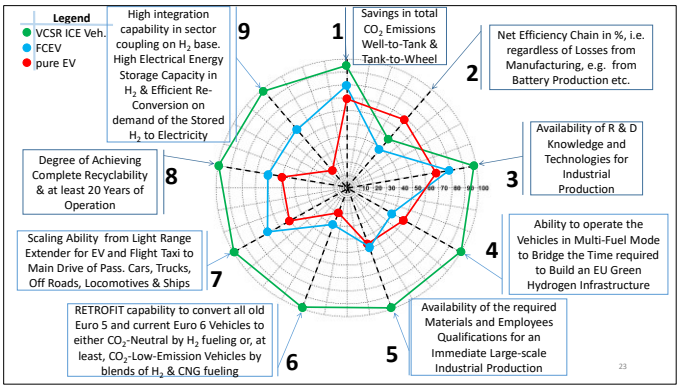

Figure 0. Graphic illustration of all nine criteria [4] applied to the three vehicle variants from legend.

The criteria are successively discussed and justified below.

*1st Criterion: Total CO_2 Emission Reduction, Well-to-Tank (WTT) & Tank-to-Wheel (TTW), s. Figures 1-**

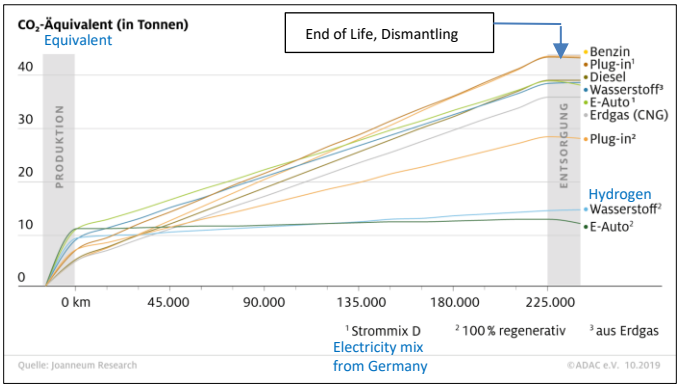

Figure 1-1-orig. The pure EVs (E-Autos) and the Plug-in are CO_2-neutral as the electricity for battery charging itself is. "Strommix D" is the electricity mix, by CO_2 emissions, of the electricity produced in Germany. Source (Joanneum Research, Austria 2019), [7]

The graphs from Fig. 1-1-orig and Fig. 1-2-orig show that the natural gas **CNG** in the VW Golf vehicle class has at this time a very good GreenHouse Gas **GHG** balance with 15 percent biomethane. Its greenhouse gas emissions over the entire life cycle (CO_2, CH_4, N_2O are summarized as $CO_2äq$, i.e. $CO_{2\text{-eq}}$) are below those of the electric car when using the German electricity mix. As well as below those of the fuel cell vehicle, which runs on hydrogen from steam reforming[3].

Even the plug-in hybrid, as a combination of a gasoline and electric motor, does not achieve any significant improvement when using the German electricity mix, even compared to the conventional gasoline engine. Its problem is the additional battery, which has a negative impact on the climate balance. Only when using renewable energy sources[2] does the electric car (EV) show the best greenhouse gas balance, closely followed by the fuel cell vehicle. The balance sheet of the plug-in hybrid vehicle also improves significantly when using renewable electricity sources. The graphs from Fig. 1-1-orig are updated after substituting the classical ICE by VCSR ICE with UD LC, which results in the entries from Fig. 1-1-feasible. An average efficiency improvement of at least 25% of VCSR ICE s. [1], [2] has been calculated, resulting in a minimum 25% reduction of TTW!

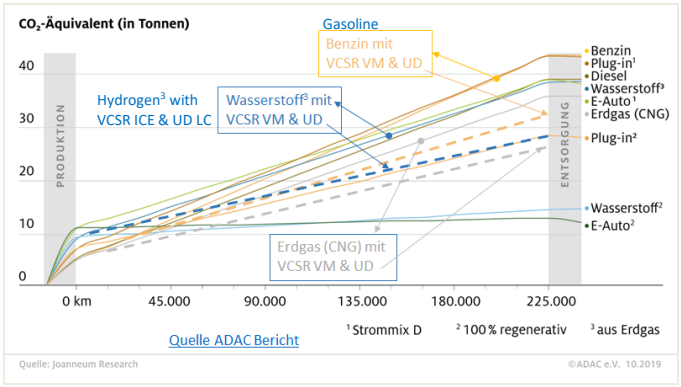

Figure 1-1-feasible. The **dashed** curves showing the CO_2 equivalent reduction potential by using ICE with UD LC are added by the author. That corresponds to a 25% reduction of TTW

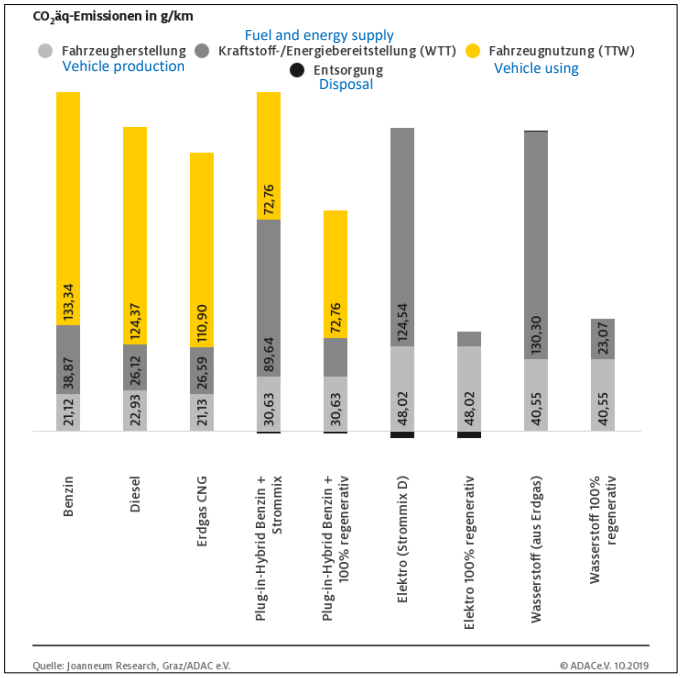

Figure 1.2-orig. The actual aggregated CO_2 emission over production, energy supply, vehicle use and disposal. Source (Joanneum Research, Austria 2019), [7]

The natural gas car could also benefit from biomethane produced from renewable sources. Nevertheless, these [7] calculations only take into account a biomethane share of 15 percent for the natural gas drive. That is roughly equivalent to the average biomethane share of natural gas sold at CNG filling stations in Germany. This is because 100% biomethane is only offered at some filling stations and is not available countrywide in Germany.

The columns with the VCSR entries in Fig. 1.2-feasible are added by the author and show the possible reduction in CO_2 emissions when VCSR ICE with UD load control (LC) is used. An average efficiency improvement of at least 25% has been calculated, resulting in a minimum 25% reduction of TTW.

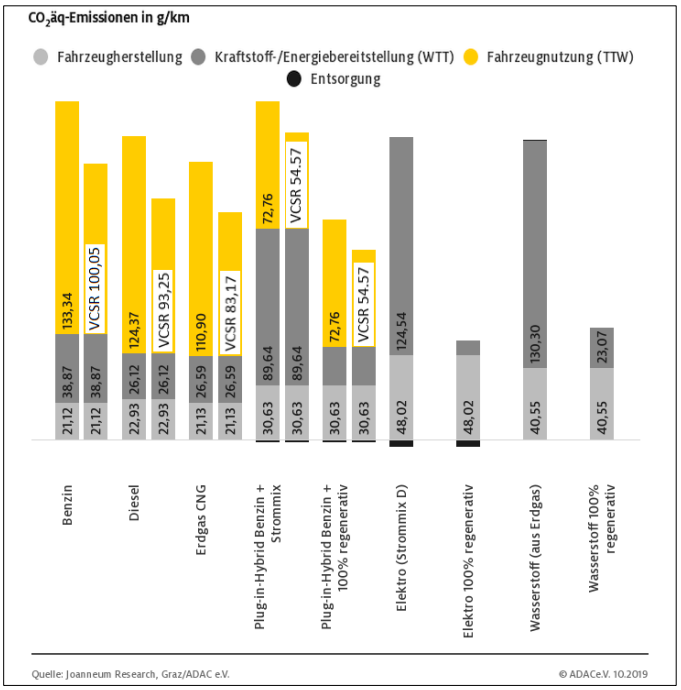

Figure 1.2-feasible. The aggregated CO_2 emission over production, energy supply, vehicle use and disposal. The columns with VCSR entries (added by author) show the CO_2 equivalent reduction potential when using VCSR ICE with UD LC. That corresponds to a 25% reduction of TTW

A new study of Plug-in-Hybrid EV, PHEV by ISI Germany [19] shows:

PHEV fuel consumption and tail-pipe CO_2 emissions during real-world driving test cycles, on average, are approximately two to four times higher than the values demanded by regulations! [19]

The evolution of the **GHG** emissions in Germany in the last 20 years is presented in Fig. 1-6.

The estimated electricity mix for Germany (DE) in 2030 will be around 430 $CO_{2\text{-eq}}$ / kWh and will likely decrease in 2050 to 285 $CO_{2\text{-eq}}$ / kWh. These values are added to the bar chart from Figure 1-3-orig.

Romare and Dahllöf (2017) [9] estimate that between 145 kg and 195 kg of $CO_{2\text{-eq}}$ are emitted per kWh battery capacity. For one Tesla battery of 75 kWh means additional CO_2 emissions from 10,875 kg to 14,625 kg CO_2. Given a battery life of ten years and a driving distance of 15,000 km per year, this implies that between 73 grams and 98 grams of CO_2-emissions must be applied for battery production and recycling per kilometer of driving distance.

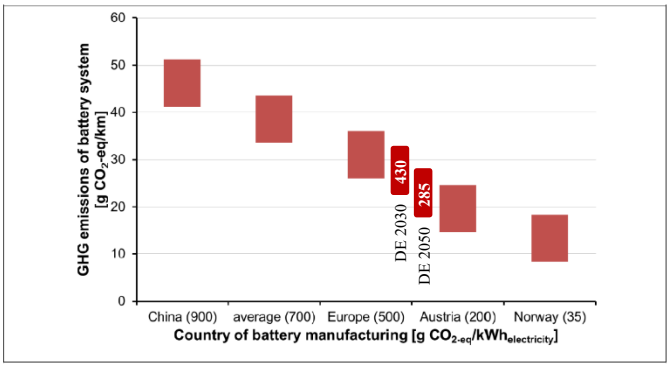

Figure 1-3.orig. & (added values for DE) Influence of the country-specific electricity mix for battery production on the estimated range of greenhouse gas GHG emissions Source (Joanneum Research, Austria 2019), [7], A/N: added for Germany (DE)

The energy required for production has a strong influence on the estimated greenhouse gas **GHG** emissions from automotive batteries. Explicitly per kWh of battery capacity are approximately 171 kg $CO_{2\text{-eq}}$ for recycling and 95 kg $CO_{2\text{-eq}}$ for stationary second life. Recycling s. Fig. 1-4 orig. has only a small impact, as the associated greenhouse gas emissions are roughly equivalent to the bonus points for the recycled materials, while the impact of second life is quite high, as it accounts for about half of the greenhouse gas emissions.

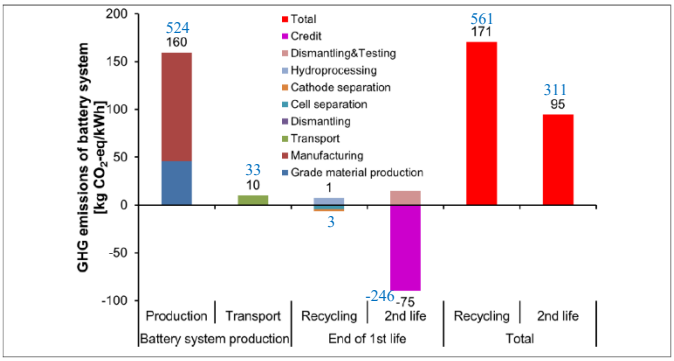

Figure 1-4.orig. & (added blue values for DE). Estimated average greenhouse gas GHG emissions of vehicle battery systems (black values) during their lifecycle (s. Fig. 6). A/N: The GHG emission values from the diagram multiplied by 3.28 give the estimated average cumulative primary energy expenditure of vehicle battery systems per kWh of battery capacity (s. blue values). Source (Joanneum Research, Austria 2019), [7]

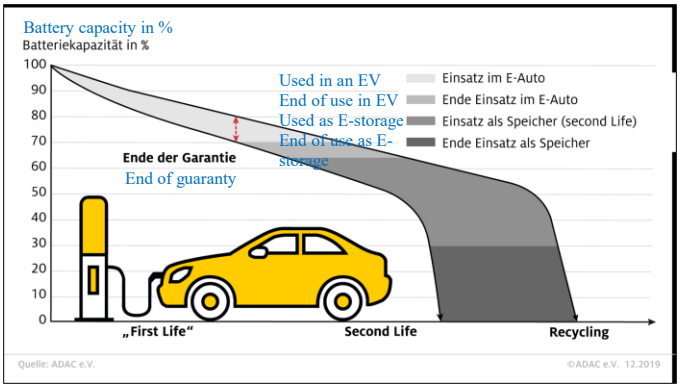

Figure 1-5.orig. Lifecycle of the EV battery systems Source [7]

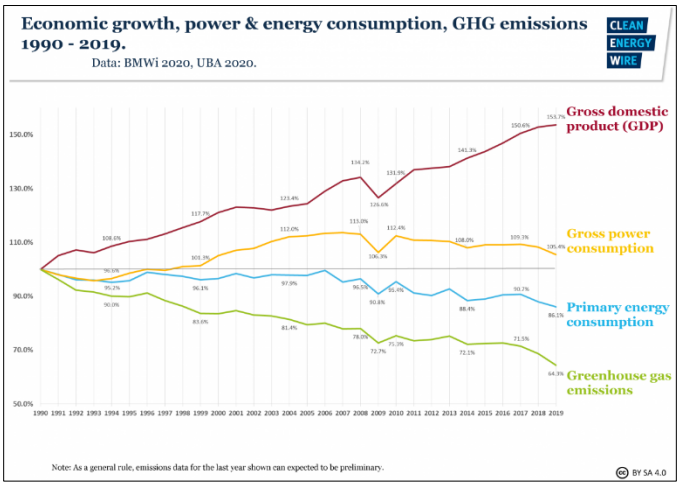

Figure 1-6. Evolution of the Economic growth, power & energy consumption as well as of the GHG emissions in Germany in the last 20 years

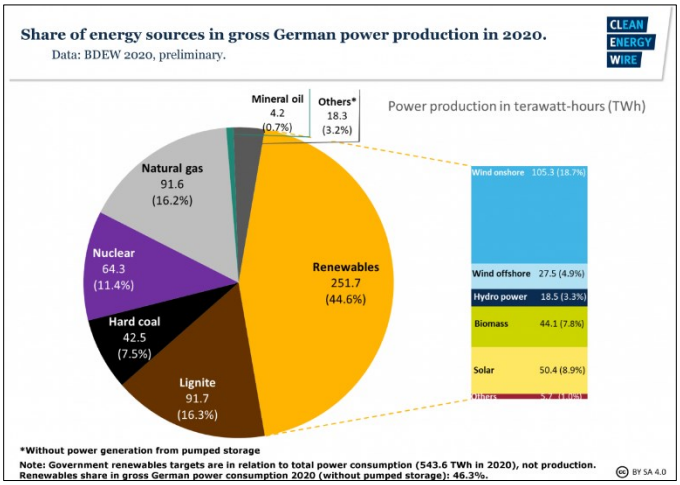

Figure 1-7 Germany electricity production mix of renewables energies – shared by source - and nuclear energy, and fossil fuels opposite.

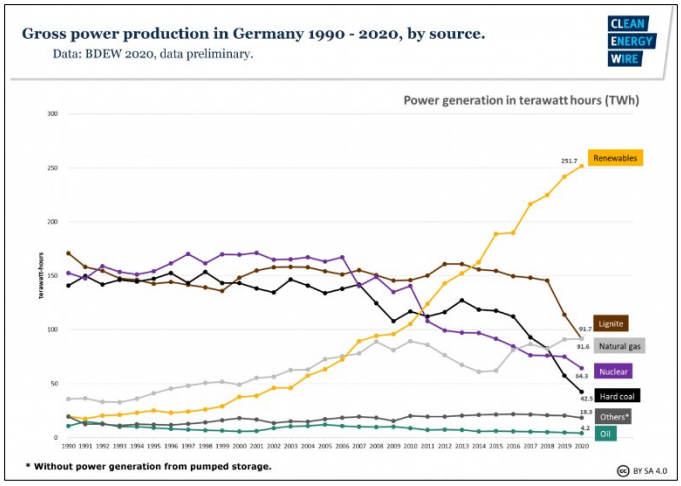

Figure 1-8. Germany electricity production mix evolution over the last 20 years.

*2nd Criterion: Net Efficiency Chain, i.e. Regardless of Losses from Manufacturing, e.g. from Battery Production etc. s. Figures 0 and 2-**

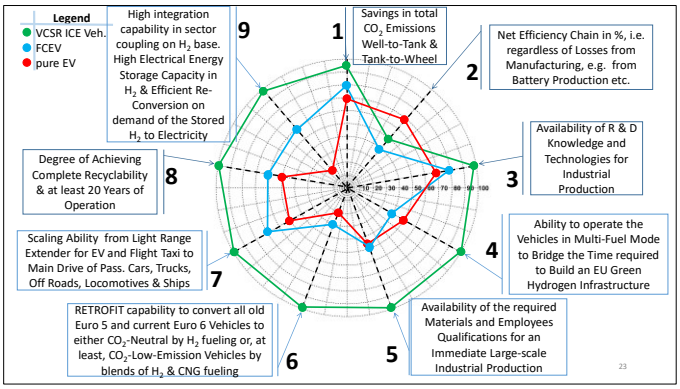

Figure 0. Graphic illustration of all nine criteria [4] applied to the three vehicle variants from legend. This figure is repeated here just as a reminder, i.e. only for improving the readability of the paper!

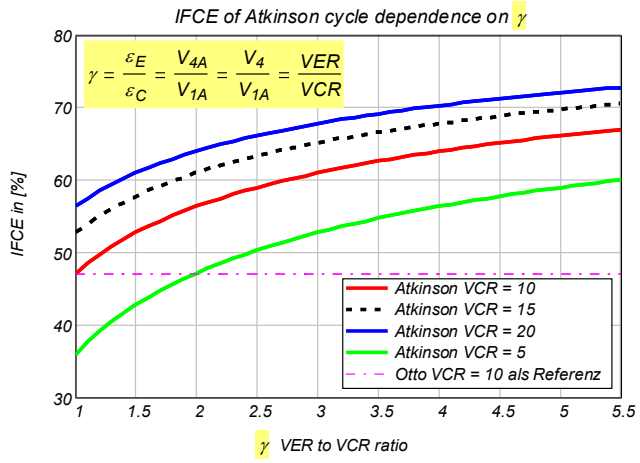

Figure 2-1. Indicated Fuel Conversion Efficiency IFCE over γ for a true Atkinson cycle for some VCR values, compared with a classic gasoline (Otto) cycle as reference. The potential for efficiency improvement if true Atkinson cycles with variable VCR are used instead of classic gasoline cycles (Otto, with VCR = 10) is clearly shown. VER is the Volumetric Expansion Ratio. See Appendix 1 for details.

The Values for the net efficiency chain from Figure 0 for the three analyzed variants originate from the right sided estimations: Net Efficiency Chain [%], i.e. regardless of Losses from Manufacturing, e.g. from Battery Production etc. high pressure PEM Electrolysis with Honda stack [15].

The Indicated Fuel Conversion Efficiency **IFCE**(VCR, γ) from Fig. 2-1 shows clearly the potential for efficiency improvement if true Atkinson cycles are used instead of classic gasoline cycles (Otto, with VCR = 10). A thermodynamic demonstration of it is presented in Appendix 1. The offered continuous variation of the **VCR** in the true Atkinson cycle of VCSR ICE allows the Ultra Downsizing UD load control LC even when the Air-Fuel-Ratio is kept stoichiometric, i.e. AFR = 1, see Appendix 2 or even [1], [2].

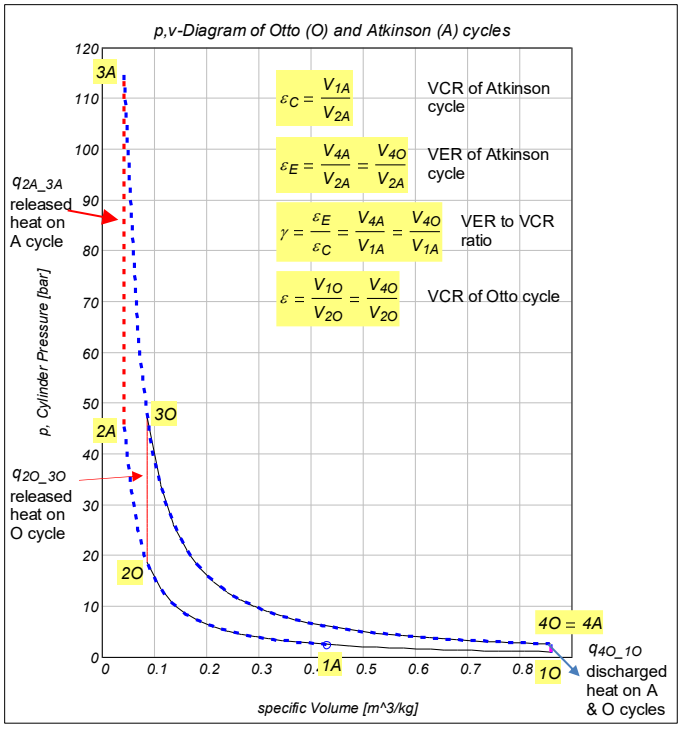

Figure 2-2. True Atkinson (A & index A) and Otto (O & index O) cycles in p,v-Diagram. For more details, s. below the Appendix 1.

Net Efficiency Chain in %, i.e. regardless of Losses from Manufacturing, e.g. from Battery Production etc.

Efficiency Chain for **VCSR ICE** Vehicle:
1. Electricity from renewable Energy
2. Short Haul of Electricity 95%
3. High pressure PEM Electrolyze 80%
4. Short Haul of Hydrogen 95%
5. IFCE of VCSR ICE 50%
6. Mechanical Drivetrain 95%

overall efficiency **35%**

Efficiency Chain for **FCEV**:
1. Electricity only from renewable Energy
2. Short Haul of Electricity 95%
3. High pressure PEM Electrolyze 80%
4. Short Haul of Hydrogen 95%
5. PEM 50%
6. Electric Motor 85%
7. Mechanical Drivetrain 95%

overall efficiency **29%**

Efficiency Chain for **EV**:
1. Electricity only from renewable Energy
2. Short Haul of Electricity 95%
3. Charge / Discharge 90%
4. Electric motor 85%
5. Mechanical Drivetrain 95%

overall efficiency **69%**

Figure 2-2b. List of net efficiency chain estimates.
Efficiency Values of the VCSR ICE were already presented in Fig. 2-1.
Efficiency Values of the EV were already presented in Fig. 1-1.
Efficiency Values of the FCEV are presented in Fig. 2-3 and Fig. 2-4.

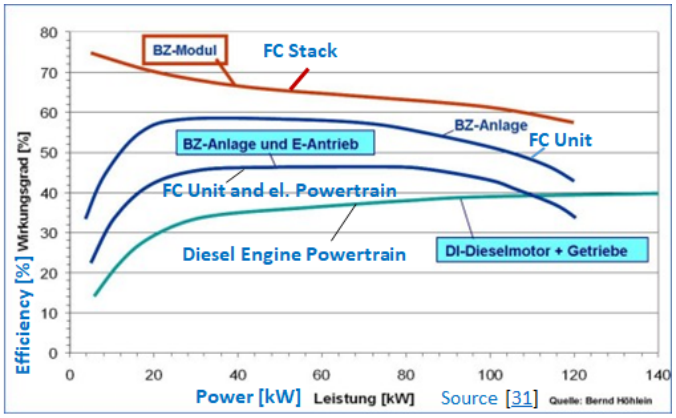

Figure 2-3. The Fuel Cells (here PEMFCs) are less efficient at high loads and, from this point of view, unsuitable for high-power level applications (i.e. Trucks, Locomotives, and Ships) [31]. A large part of the fuel energy is converted into heat in stacks. This heat is released at a low temperature (between 70 and 100 °C). Therefore, because of the low temperature difference to the environment, huge heat exchangers are needed to exhaust it.

At a pressure of 1 bar and a temperature of 25°C, the corresponding ideal DC voltage of a PEM FC is 1.23 volts. This voltage is a function of temperature, i.e. the same applies to efficiency. In the PEM FC stack, the efficiency is already reduced by Ohmic losses and over voltages, as losses due to mass transfer.

In practice, this results in a single cell terminal voltage of 0.7 V. If higher voltages are required, several cells are connected in series to form a fuel cell stack. In theory, any voltage can be achieved in this way. However, this is limited by cooling problems and flow losses during the supply of the reaction gases. The current density potential curves of an operational fuel cell resemble those in Figure 2-4. The figure shows that the Cell Voltage U decreases when Cell Current I increases. The released electrical power $-P^{FC} = |P^{FC}|$ reaches a maximum at a certain current $I_P = I_{max}$ (see point A). In this state, the exhausted heat Q´ is more than two times bigger than the released electrical power (see point B), [20].

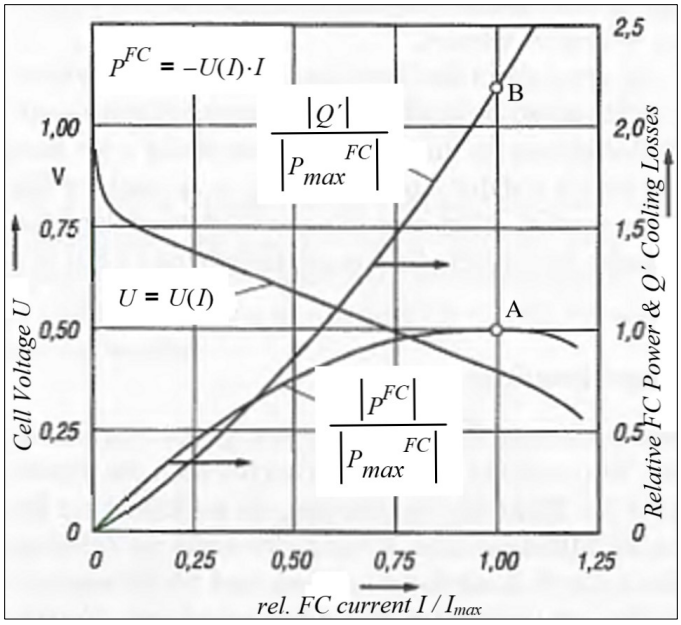

Figure 2-4. Characteristic Curves of a Fuel Cell FC. Electrical Voltage-Current U(I) characteristic (left axis). Relative FC Power P and relative Cooling Losses Q´ (right axis) as function of the relative Current of a FC, [20].

3rd Criterion: Availability of R & D Knowledge and Technologies for Industrial Production.

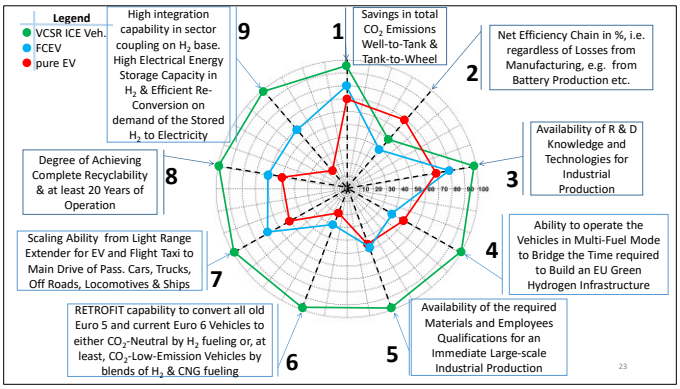

Figure 0. Graphic illustration of all nine criteria [4] applied to the three vehicle variants from legend. This figure is repeated here just as a reminder, i.e. only for improving the readability of the paper!

The availability of R&D knowledge regarding the VCSR ICE with DU LC is shown below for two layout variants of three cylinder engines: 3L & 3Y. In both variants, the flywheel can be linked to a classical clutch or replaced suitably by generators or flight propellers.

A special feature of the VCSR crank drive is that the torque can be delivered in parallel at two speeds via the flanges of the:

a) planet carrier (s. Fig. 3-1) at half speed (n/2) and
b) sun gear (s. Fig. 3-2) at twice the speed (2*n),

whereby n is the speed of the eccentric crank (EC, s. Fig. 3-3) of the true 4-stroke-Atkinson-cycle of the VCSR ICE. [1], [2], [10], [11].

The Variant 3L of the VCSR crank mechanism is briefly presented and explained in the Fig. 3-1, Fig. 3-2 and Fig. 3-3, s. [1] for several animations of this crank mechanism.

The Variant 3Y of the VCSR crank mechanism is briefly presented and explained in the Fig. 3-4 and Fig. 3-5, s. [23] for an animation of this crank mechanism.

The VCSR ICE in all Variants L, Y or V are able to operate in Multi-Fuel Mode, i.e. from pure H_2 to different blend combinations with CNG to bridge the time required for building an EU/World Green Hydrogen Net Infrastructure (s. 4th Criterion below).

Matlab® / Simulink / Simscape / Multibody Toolbox were used to model the VCSR crank drive, simulate the kinetics and complete the crank drive animations. The fluid and thermodynamic processes were modeled and simulated with the AVL BOOST® tool.

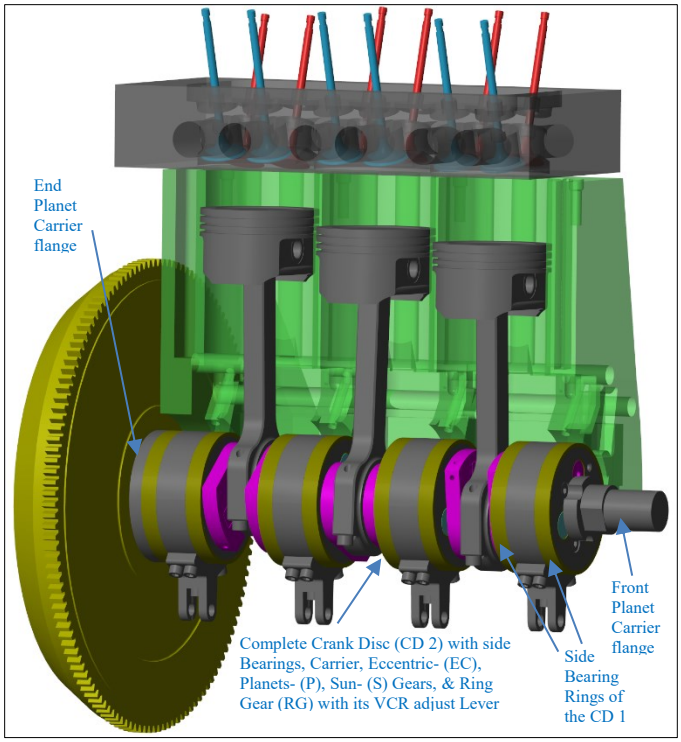

Figure 3-1. Full view of the 3L crank mechanism with its four crank disks (CD), their Slide- or Roll-bearing Rings and VCR adjust levers connected at each Ring Gears (RG), s. [1] for animations of this crank mechanism. The CDs act as shaft journals. Because the CDs have the half rotation speed of the eccentric cranks (EC) - like the camshaft of a classical engine – CDs can also carry the cams for valve actuating (not shown here).

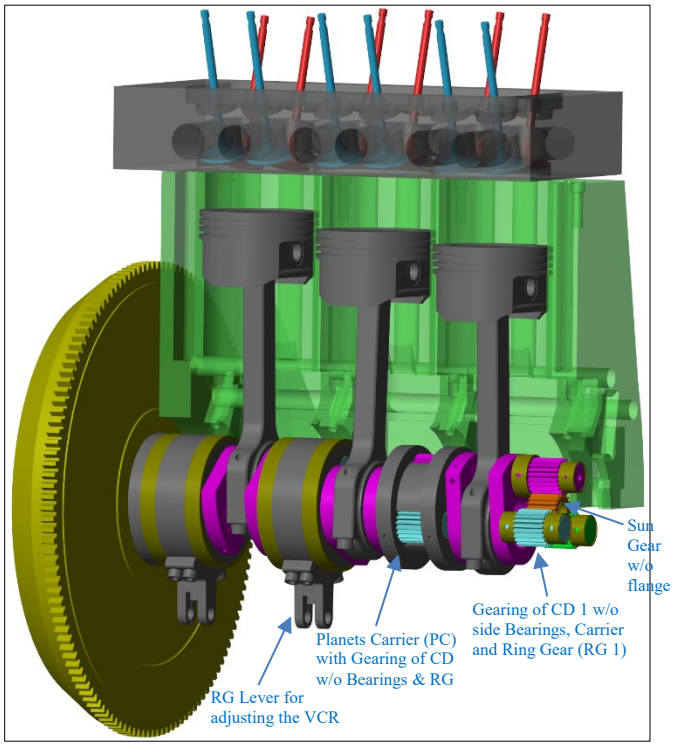

Figure 3-2. Some inward details of the 3L crank mechanism, such as the internal Gearing of CD 1 and the Planet Carrier (PC 2) and inner Gearing of CD 2.

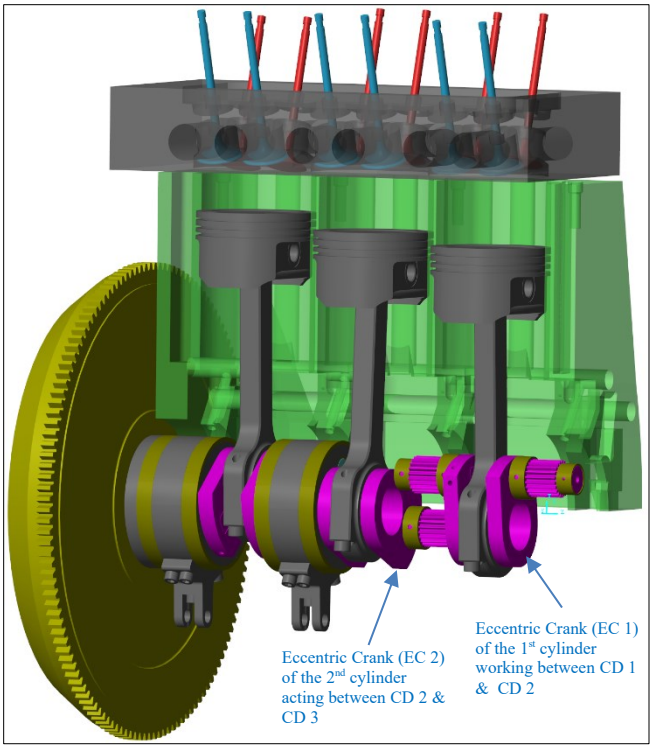

Figure 3-3. Some inward details of the 3L crank mechanism, such as the Eccentric Crank EC 1 of the 1st cylinder and the right side of EC 2.

Fig. 3-4 and Fig. 3-5 feature the 3Y Variant, s. [23] for an animation of this crank mechanism variant. Both variants use similar components. Therefore, a detailed description of variant 3Y is not necessary.

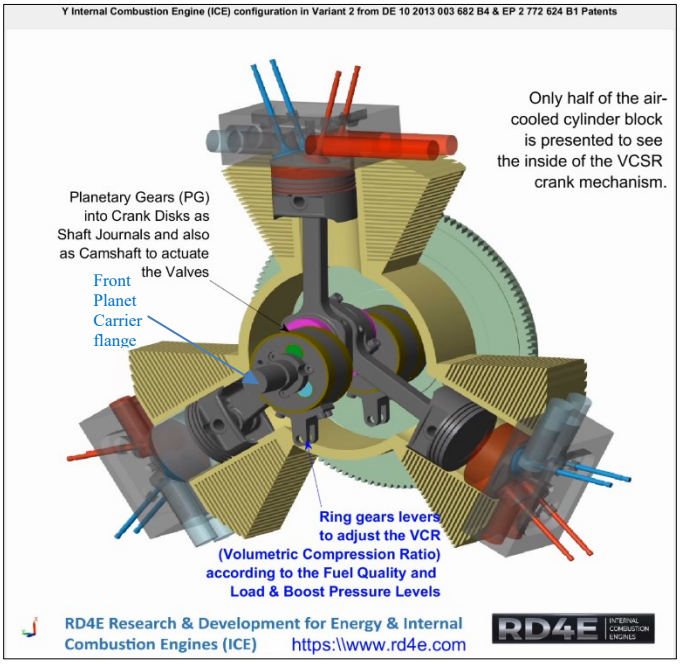

Figure 3-4. Full view of the 3Y crank mechanism, see a short video of it [23].

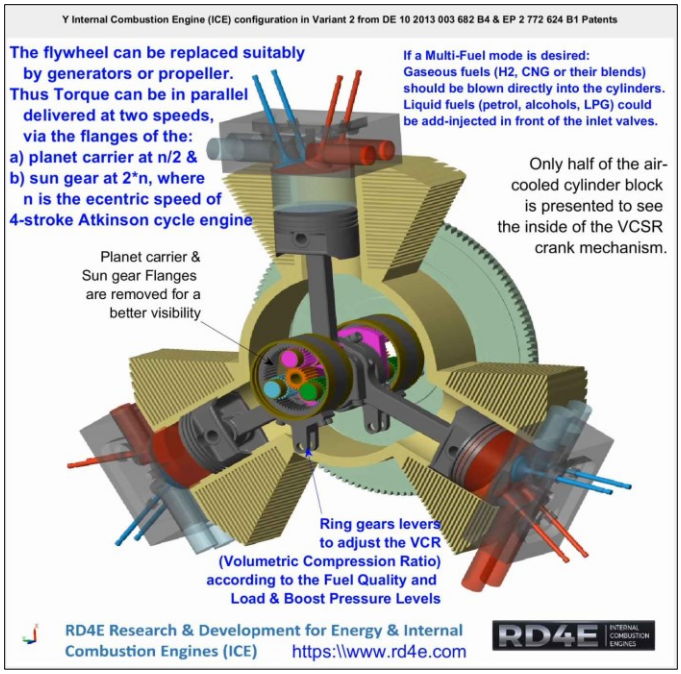

Figure 3-5. Some inward details of the Gearing of the 3Y crank mechanism.

The Crank Discs (CD), Ring Gears (RG) and their levers are identical in both 3L and 3Y variants. Only the cylinder arrangement is different.

The 3Y Variant is much more compact, has fewer moving components and Planet Gears (PG) than 3L and is therefore ideally suited as a Range Extender in electric vehicles EV or Flight Taxis.

4th Criterion: Ability to Operate Vehicles in Multi-Fuel Mode to Bridge the Time Required for Building an EU/World Green Hydrogen Infrastructure.

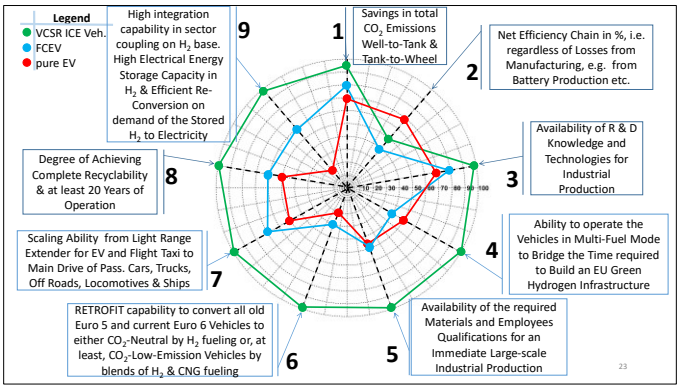

Figure 0. Graphic illustration of all nine criteria [4] applied to the three vehicle variants from legend. This figure is repeated here just as a reminder, i.e. only for improving the readability of the paper!

For EVs, the given value from Fig. 0 should be interpret as the possibility to supply Trucks and Buses with electrical energy via overhead lines (like Trams) instead of batteries.

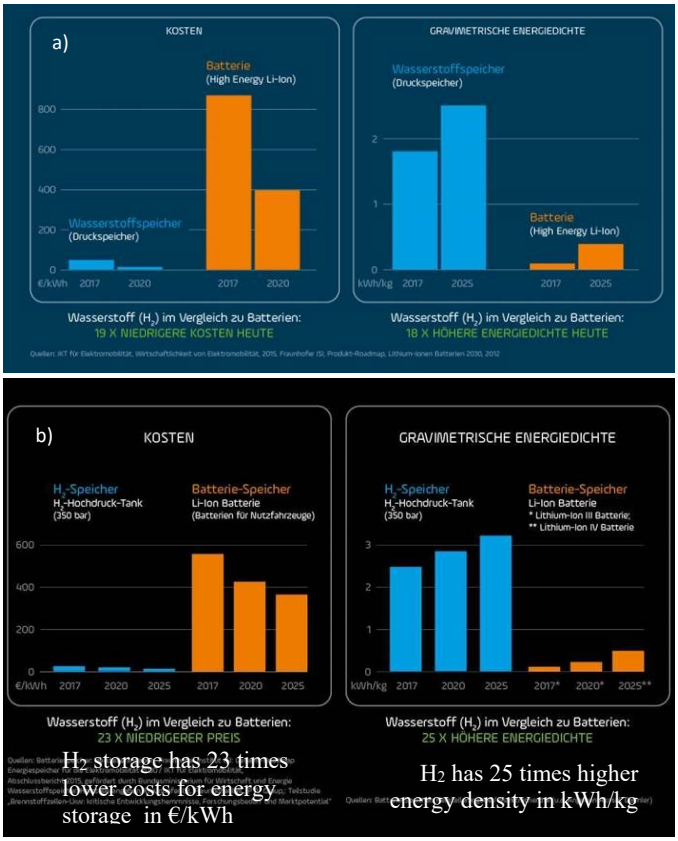

Figures 4-1. ISI Reports, a) 2012 and b) 2015. Costs on the left side versus gravimetrical energy density on the right side. Orange are the values for the batteries and the blue ones for H_2 storages, Source ISI. Additional information

Even the latest developments in battery research cannot fundamentally change the precarious position of batteries in relation to H_2 storage, s. Figures 4-1 a) and b). The latest magnesium-based batteries have energy densities of 400 Wh/kg, which are better than the classic Li-ion batteries (maximum of 250 Wh/kg), but remain far inferior to the more than 2500 Wh/kg offered by H_2 storages (with 35 MPa = 350 bar).

A brief comparison of the energy storage is provided in Fig. 4-1 a) and b).

For the usual option of 700 bar, the energy density reaches almost 4200 Wh/kg (due to the real gas behavior of H_2, it's not twice as much as 350 bar, see Fig. 4-2).

Below are some examples of Key DOE Hydrogen Program Targets from Conceptual H2@Scale energy system from USA EERE [21]:

I. $2/kg for hydrogen production and $2/kg for delivery and dispersing for transportation applications. (*Costs are so far unknown*)
II. $1/kg hydrogen for industrial and stationary power generation applications (*Costs are so far unknown*)
III. Fuel cell FC system cost of 80$/kW with 25,000-hour durability for long-haul heavy-duty trucks. (*Actually already possible, if VCSR ICE with UD LC are used instead of FC*)
IV. On-board vehicular hydrogen storage at $8/kWh, 2.2 kWh/kg, and 1.7 kWh/l (*First two requirements are already possible; see Fig. 4-1 a) and b)*).
V. Electrolyzer capital cost of $300/kW, 80,000-hour durability, 65% system efficiency (*System efficiency of more than 80% has already been reached by a Honda electrolyzer* [15], *but costs and durability are so far unknown*)
VI. Fuel cell FC system cost of $900/kW and 40,000-hour durability for fuel-flexible stationary high-temperature fuel cells. (*Actually already possible, if VCSR ICE with UD LC are used instead of FC*). Above in green are A/N.

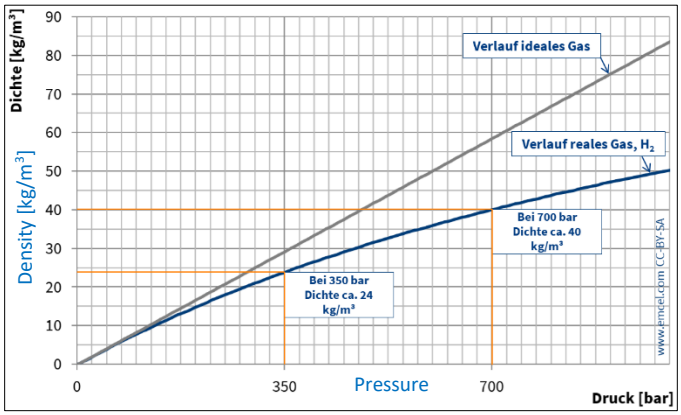

Figure 4-2. Density, Pressure diagram of hydrogen behavior as ideal and real gas.

The use of hydrogen H_2 in ICE has not yet been adapted to the current development possibilities. Fig. 9-6 shows the Conceptual H2@Scale energy system from USA EERE [21].

An overview of the advantages and disadvantages of the classical operation of an ICE with hydrogen H_2 can be found for example under EERE [21], Hydrogeit, Ford and Keyou.

a) Unlike every other fuels, ICE with hydrogen H_2 does not produce CO_2. It produce only harmless water vapor and raw nitrogen oxide emissions (NO_x).

b) The higher the combustion temperature and the oxygen O_2 concentration in the cylinder are, the higher the concentration of NO_x (raw emissions). Because the nitrogen concentration N_2 in the air is unchangeable, the only effective measures to reduce NO_x raw emissions are lowering the oxygen concentration and/or the combustion temperature. See more information under Energy Dictionary, UBA, ATK p. 2-3.

c) The trick is to solve the conflict between high power density and handling the raw NO_x emissions properly. A distinction is made here between 1) exclusive avoidance without exhaust after treatment and 2) predominant avoidance coupled with complete effective reduction of nitrogen oxide emissions NO_x by exhaust after treatment with an H_2-SCR catalytic converter; see Keyou, KIT PhD thesis J.P.Scott.

d) The classical solution in the lower partial load range was aimed at the predominant avoidance of NO_x raw emissions by a strong leaning of the H_2-air mixture to λ-values (AFR) of 3.0. While in the upper to full load the ICE is operated with decreasing λ-values to the stoichiometric ratio λ = 1 to achieve a high power density.

e) The ICE is operated in the whole load range, therefore the H_2-SCR catalyst or the classic 3-way catalyst in stoichiometric operation cannot be omitted. For this reason, it is pointless to rely too much on the avoidance of NO_x raw emissions in the lower load range. Being able to work without H_2-SCR catalytic converter is able only in the lower load range. That is comparable to the costly and senseless application test of HCCI on diesel engines to be introduced only for the lower partial load range or for city traffic [**65.1**], [**65.2**]).

f) The following investigations show the right way to operate the ICE using H_2 fueling:

- Internal Mixture Formation GasDI: The compressed H_2 from the tank is injected directly into the cylinder after closing the inlet valves, see Fig. 4-3, Ford, [**8**] etc., to eliminate the disadvantages of external mixture formation see N-1.x, N-2 and N-4 from Hydrogeit. See also Wikipedia.
- A controlled H_2 multiple direct injection known as combustion control, see [8], p.173, Figure 6-20, reduces peak pressure by 30%, pressure increases by 70% and NOx raw emissions by more than 90%! See also Fig. 4-5 & 4-6.
- The ignition can occur either as spark ignition, similar to gasoline engines, or more stable and flexible glow ignition, see Fig. 4-3, [8], p.173, Figure 6-20 and [WTZ Roßlau] for big ICEs. Compression ignition similar to diesel engines is also possible, see [WTZ Roßlau], [**8**], p. 175 and [D3], p. 62, but for various reasons is not suitable for operation.
- If the ICE is equipped with an asymmetrical crank drive VCSR mechanism, which offers an extended expansion stroke and the variation of the compression ratio VCR, it is possible to implement true Atkinson cycles and the original load control Ultra Downsizing UD LC, see [PDF] or [VIDEO].
- Thus the ICE with asymmetrical crank drive VCSR mechanism and UD LC has an efficiency more than 20% higher than that of a classic ICE s. SAE [2015].
- In addition, the ICE with the VCSR crank drive and UD LC can be operated with different fuels (i.e. as a multi-fuel engine) thanks to VCR capability.

Operating strategies for engine operation with H_2-CNG mixtures

In principle, there are several possible strategies for vehicle operation with H_2-CNG mixtures, s. also [**8**]. Of the following three variants, actually only variant III is recommended.

I. Hydrogen and CNG (mainly methane) are available in the vehicle in two separate storage tanks and are mixed according to the requirements on board. Due to the high costs of components and control system, this variant is of a more of theoretical nature.

II. Constant hydrogen content: Engines and vehicles are optimized for a specific, constant H2-CNG mixture, for example with 15-vol % hydrogen. This variant has been implemented in most current applications, but the supply of the relevant mixing ratio must be ensured at the filling stations. Ensuring the right mixing ratio of H2-CNG may be too complicated for regular filling stations.

III. Variable hydrogen content: Hydrogen and CNG are filled into the same pressure tank in any mixture. After each refueling, a sensor detects the mixture ratio and informs the engine control unit (ECU). Alternatively, the ECU calculates/estimates it from the other sensor information, such as sucked air mass, injected gas mass, lambda value and possibly even a CO_2 sensor etc. The ECU estimates a corresponding optimal parameter set for the engine control. The vehicle can be operated with different H2-CNG mixtures, from 0% to 100% hydrogen. Depending on availability, more or less pure hydrogen, methane, biogas or any mixture can be used. This concept allows the use of the infrastructure currently under development for both natural gas and hydrogen, and it allows a gradual habituation to using hydrogen as fuel. The Energy densities of Hydrogen and Methane are shown in Fig. 4-4.

Note: The basic structure of the fuel system of gas vehicles with tank systems, fuel lines and injection valves are independent of the gas in question. The essential difference lies in the materials used for the fuel-carrying components. The current materials can be used for H_2-CNG mixtures with up to 30-vol % hydrogen. For higher hydrogen concentrations, all components in contact with the fuel must be designed for the specific characteristics of hydrogen, such as hydrogen embrittlement, low lubricity and high diffusion capacity. Suitable materials include austenitic stainless steels.

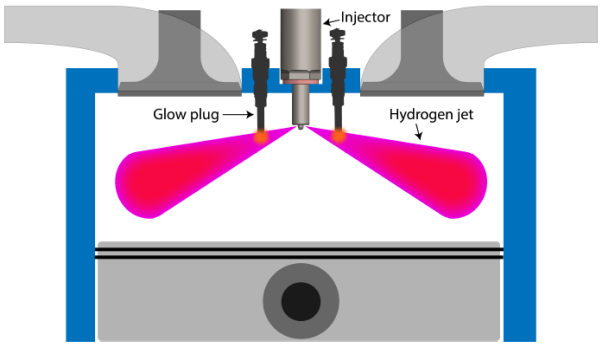

Figure 4-3. Schematic of the glow plug assisted ignition of hydrogen direct injection [24].

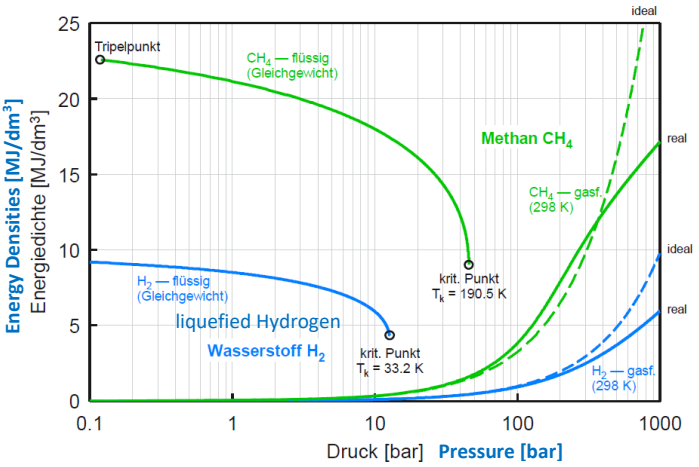

Figure 4-4. Energy densities of Hydrogen and Methane [8]. The figure shows the two fuel gases above the logarithmically plotted pressure. The values for the compressed gases at 25°C were determined taking into account the real gas behavior; the dashed curves correspond to ideal gas behavior. At high pressures, the real gas behavior cannot be neglected. A comparison of the energy density curves in the compressed and liquefied state. Compressed H_2 at 700 bar and 25°C has a higher Energy Density than liquefied H_2 in its critical state, i.e. by -271°C, 33.2 K and 12.84 bar. In Table 4-1 and 4-2 are more thermodynamically properties presented.

Note: The values for compressed gases at 25°C, 298 K were determined taking into account the real gas behavior; the dashed curves correspond to ideal gas behavior. At high pressures, the real gas behavior cannot be neglected. H2NG20 denotes a mixture of 20 vol % hydrogen and 80 vol % methane, see Table 4-2.

For the injection of fuel into the engine, but also for gas burners in general and for safety reasons, it is important to know how fast the fuel gas flows through an opening cross-section and how much energy is conveyed. If the pressure ratio between the gas pressure (at rest) and the cylinder (back) pressure exceeds a critical value ψ, the gas flows out of a cross-section at the speed of sound a.

This critical value depends on the isentropic exponent κ and is for κ = 1.4 around ψ = 1.9 for many gases (air, hydrogen etc.). Assuming ideal gas behavior, the following applies to the speed of sound a:

$$a = \sqrt{\kappa \cdot \frac{R_m}{M} \cdot T} = \sqrt{\kappa \cdot \frac{p}{\rho}}$$

with $\kappa = \frac{c^\circ_p}{c^\circ_v}$ Isentropic exponent as the ratio of the isobaric c°_p to isochoric c°_v spec. heat capacities, $\kappa := 1.4$ for air

$$\psi = \frac{p}{p_{cr}} \qquad \psi = \left(\frac{\kappa + 1}{2}\right)^{\frac{\kappa}{\kappa - 1}} \qquad \psi = 1.893$$

$R_m = 8314.472 \cdot \frac{J}{kmol \cdot K}$ molar gas constant

M molar mass [kg/kmol]

T Kelvin (absolut) temperature [K]

p pressure [Pa]

The mass flow m´ exiting through the opening A of a gas injector corresponds to the product of gas density, speed of sound a, and its area cross-section A.

Although the critical speed a cannot be exceeded, the mass flow through a cross section A increases as pressure rises due to the increasing density. If the mass flow is multiplied by the gravimetric lower calorific value H_u, see Table 4-1, the energy flowing out E´ in a unit of time is obtained:

A area cross-section

$\rho = \frac{p}{T} \cdot \frac{M}{R_m}$ density [kg/m³]

$m' = \rho \cdot a \cdot A$ mass flow [kg/s]

$E' = H_u \cdot m'$

$$E' = \rho \cdot \sqrt{\kappa \cdot \frac{p}{\rho}} \cdot A \cdot H_u$$

Table 4-1. Thermodynamic properties for the energy throughput of hydrogen H_2 and methane under normal atmospheric conditions, 1 bar and 300 K.

Gas	M [kg/kmol]	ρ [kg/m³]	κ [-]	a [m/s]	H_u [MJ/kg]
Wasserstoff H_2	2,016	0,08	1,405	1315	120
Methan CH_4	16,04	0,64	1,306	449	50

Due to its low molar mass, the speed of sound of hydrogen is almost three times higher than that of methane. The density of hydrogen is almost one order of magnitude below that of methane, which is why mass flow rate of hydrogen at the speed of sound is significantly lower.

Due to the high gravimetric lower heating value, H_u this difference is almost equalized. Therefore, the energy throughput through an opening of the same gas injector cross section A at the same gas pressure is the same for hydrogen and methane.

The energy throughput of a gas through a cross section A of a gas injector is determined by the energy flow rate according to DIN 51857, which is derived from the volumetric Wobbe index W_o, calorific value at normal conditions, and the root of the relative density of the flue gas into air. As with the calorific value, the Wobbe index distinguishes a lower and an upper value, depending on whether the heat of condensation of the water in the flue gas is included or not:

$$W_o = \frac{Ho\_vol}{\sqrt{d}}$$ Wobbeindex [MJ/Nm³]

where

$$H_{o\_vol} = \rho \cdot H_o$$ upper volumetric heating value of the fuel gas

$$d = \frac{\rho_{gas}}{\rho_{air}}$$ relative density [-]

ρ_{gas} density of the fuel gas [kg/m³]

ρ_{air} air density [kg/m³]

According to the above correlations, two gases at the same pressure and flowing through the same opening cross-section A at the same Wobbe index W_o result in equal energy throughputs at critical discharge, if the influence of different isentropic exponents is neglected.

Table 4-2 shows the (upper) Wobbe indices of methane, natural gas in Austria, various H_2NG mixtures and hydrogen, where H_2NG20 denotes a mixture of 20 vol % hydrogen and 80 vol % methane [8].

Table 4-2. Upper volumetric heating values $H_{o\,vol}$ and Wobbe indices W_o of the fuel gas under normal atmospheric conditions at 0°C and 1.013 bar.

	CH_4	Erdgas in Österreich	H_2NG15	H_2NG30	H_2NG50	H_2NG80	H_2
$H_{o\,vol}$ [MJ/Nm³]	39,91	39,86	35,38	31,76	26,33	18,18	12,75
W_o [MJ/Nm³]	54,00	53,01	52,01	50,02	47,48	44,87	48,66

The similar values for the Wobbe index of methane and hydrogen mean that, for the same energy throughput, a natural gas injector for hydrogen can be used without having to change the opening cross section A or opening time. However, it remains to be determined, whether the construction and the materials are suitable for hydrogen use.

A major advantage of H_2NG mixtures is that as the hydrogen content increases, the C/H ratio of the fuel mixture decreases, thus reducing greenhouse CO_2 emissions. An estimation of the CO_2 emission reduction potential can be made using the ideal combustion equations.

The combustion of 1 mol CH_4 produces 1 mol CO_2, which corresponds to 2.75 kg CO_2 per kg CH_4 or, at a lower heating value of 13.9 kWh/kg (50 MJ/kg), about 200 g of CO_2 per kWh, which means a reduction of more than 25% compared to petrol or diesel. For hydrogen with a lower heating value of 120 MJ/kg, no CO_2 is produced. The molar CO_2 formation is reduced to the extent that hydrogen is added in vol % [8].

Engine operation strategies for H_2 multi injections to reduce drastically the NO_x raw emission.

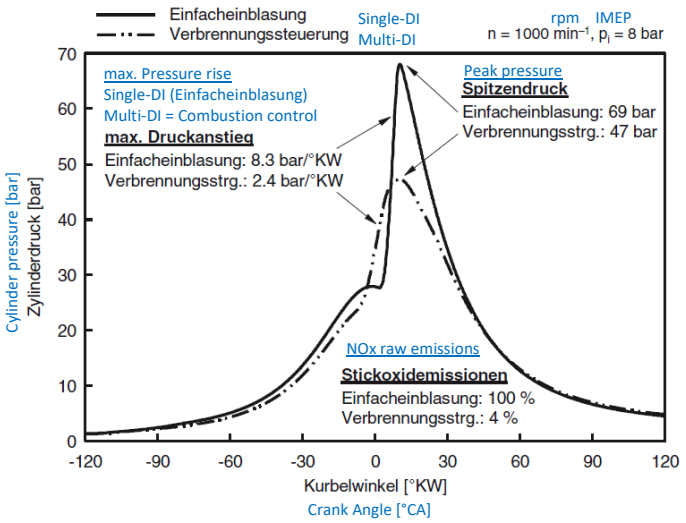

Figure 4-5. Potential for improvement through combustion control according to [8]

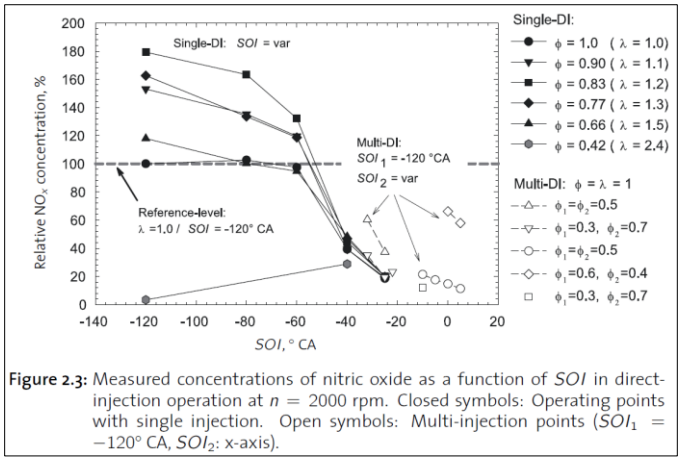

Figure 2.3: Measured concentrations of nitric oxide as a function of *SOI* in direct-injection operation at n = 2000 rpm. Closed symbols: Operating points with single injection. Open symbols: Multi-injection points (SOI_1 = −120° CA, SOI_2: x-axis).

Figure 4-6. Potential for improvement through combustion control according to [12]

Regarding future engine strategies, the significance of multi-injection, partial diffusion-flame operation has to be considered. Present results show a slight decrease of the engine efficiency in this operation mode; however, peak in-cylinder pressures and combustion anomalies are remarkably reduced. This type of combustion, i.e. multi-DI, is adequate in conjunction with a highly compressed supercharged engine with variable VCR in order to control all load operations.

5th Criterion: Availability of the Required Materials and Employees Qualifications for Immediate Large-scale Industrial Production

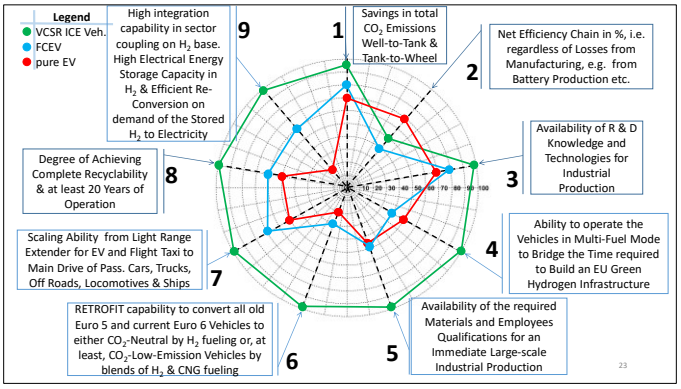

Figure 0. Graphic illustration of all nine criteria [4] applied to the three vehicle variants from the legend. This figure is repeated here just as a reminder, i.e. only to improve the readability of the paper!

The extreme scarcity of the Materials required for battery production is so pronounced that Germany demand alone within the Scope of "Sustainable Mobility & Energy Transition in a Changing Climate" **nMnEW** for the Manufacturing of the Electrical Energy Storage exceeds its share of the Global Production Values by 100% or even 1.000% see **UBA** (Table 2, p.33) [**16**], further down presented as Table 5-1.

The need for materials required only for producing batteries for EVs is presented on the **E-Mobility** column of Table 5-1.

FCEVs are very expensive because they require:

a) Relevant rare materials (s. Table 5-1),
b) Very special manufacturing processes,
c) Very special qualification of employees for production and maintenance,
d) High sensitiveness in operation because of its difficult maintenance, no freezing state after shutdown, vulnerability of the used electrodes & membranes used, and consequently in a short service life
e) High purity level for hydrogen and air (w/o carbon monoxide CO)

The scheme of Fig. 5-1 should be taken into consideration regarding the H_2 mobility chains of Table 5-1, (p. 57 of [**16**]). The electro mobility scenario considers five different propulsion systems involving battery electric vehicles, hybrid vehicles and vehicles connected to overhead cables. The inventory covers all vehicles, from cars of various sizes to lorries and buses. This resulted in a total of around 43.4 million vehicles with a combined battery capacity of around 1,067 GWh.

The hydrogen mobility scenario differs from the e-mobility one in that it assumes that electric vehicles are used in addition to hydrogen vehicles: H_2-vehicles are deployed for longer distances and EVs for shorter ones. Fig. 5-1 provides a schematic representation of the H_2 chains for hydrogen mobility.

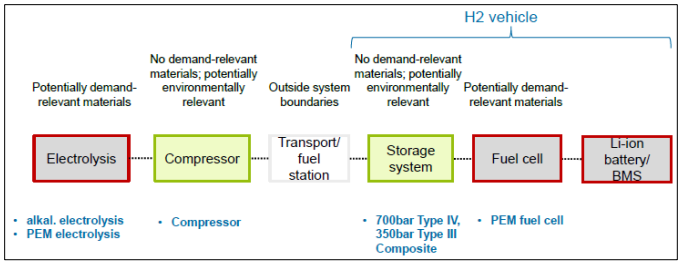

Figure 5-1. Scheme for H_2 chains for mobility using only FCEV from [**16**]. The red boxes are built with potentially demand-relevant materials from Table 5-1. Electrolysis is an exception because it can either alkaline or done by PEM. In the case of PEM, the compressor could even prove superfluous [**15**].

The values originate from Table 5-1, (p. 57 of [**16**]) and show clearly that these two types of sustainable mobility are not feasible due to insufficient materials for their production, operation and maintenance.

The criterion of demand relevance is defined in the present study [**16**] as the proportion of world production of a particular element or raw material in the year 2020 that is used in innovative Energy Storage Systems (ESS). This is determined initially by current production, which is taken to be an approximate indicator of world consumption. With regard to the future scenario of 80% renewable energy and the future mobility scenarios, it is also determined by the increase in material requirements as a result of annual economic growth. The future development of world production must therefore be considered; demand relevance is calculated in relation to world production in the year 2020.

The share of the ESS in world production in 2020 is calculated from the world production data for 2020 and the maximum material requirements of the ESS (using the values for the overall results of the ESS, see Table 5-1). These shares of the ESS in 2020 world production are the values used to rate the demand relevance of each raw material.

A striking fact that emerges from the results (Table 5-1) is that for some materials/elements, the ESS share of world production exceeds 100% or even 1000%. This means that the maximum material requirement of these materials/elements for the ESS alone is higher or even several times higher than the entire world production in 2020. This is the case for cobalt, lithium, titanium, vanadium, platinum, iridium and graphite. Because of this special situation, these seven elements are classed as demand-relevant. The applications of these seven demand-relevant materials in the innovative ESS and their percentage shares of the 2020 world production are described briefly below.

- Iridium (1,285%): used only in PEM electrolyzers (as metal or oxide)
- Lithium (990%): Used in li-ion batteries (as a component of chemical compounds, not in elementary form); by far the largest requirement is in LTO-LFP
- Cobalt (376%): greatest requirement for C-LNMC li-ion batteries; additional relevant requirement in other ESS (as oxide)
- Platinum (145%): used in PEM fuel cells and PEM electrolyzers (as metal)
- Graphite (135%): used in all batteries except LTO-LFP and Zn-air and in PEM fuel cells (in elementary form)

‣ Titanium (110%): greatest requirement for LTO-LFP li-ion batteries (in oxide form), otherwise only used in PEM electrolyzers (as metal)
‣ Vanadium (105%): only used in V-V redox flow batteries (in oxidized form).

Table 5-1. Percentage share of Energy Stored System ESS in 2020 world production for all electricity supply and mobility applications (selected materials) [16] p. 57

	Batteries, stationary	H2, stationary	H2, mobile	E-mobility	ESS total
Al	n/a	n/a	n/a	n/a	n/a
Co	10%	0%	126%	367%	**376%**
Cr	2%	0%	0%	0%	2%
Cu	0%	0%	2%	6%	6%
Fe	n/a	n/a	n/a	n/a	n/a
Li	26%	0%	330%	964%	**990%**
Mn	0%	0%	1%	2%	2%
Ni	0%	1%	14%	17%	19%
P	0%	0%	2%	5%	5%
Pb	0%	0%	0%	0%	0%
Ti	3%	0%	37%	107%	**110%**
V	105%	0%	0%	0%	**105%**
Zn	0%	0%	0%	0%	0%
Pt	0%	7%	139%	0%	**145%**
Ir	0%	140%	1145%	0%	**1285%**
La	8%	0%	0%	0%	8%
Graphite	3%	6%	46%	125%	**135%**
Au	0%	0%	0%	0%	0%
Ag	0%	0%	0%	0%	1%
F	0%	0%	1%	4%	4%

The scheme of Fig. 5-1 should be modified as follow:

a) The electrolysis and the compressor can be substituted by PEM electrolysis from Honda [15] with its H_2 output by 700 bar, 70 MPa.
b) The PEM fuel cell FC can be substituted by VCSR ICE with UD LC. In this case, potentially relevant materials are no longer needed.
c) A hybrid vehicle with VCSR ICE in place of PEM FC needs a much smaller battery. The best example is the Toyota Prius II, which has only a nickel-metal-hydride battery with 21 kW output [17].

The components of the VCSR ICE with UD LC, i.e. operated stoichiometrically with H_2 or in a Multi-Fuel Mode, are well known when their principal parts are taken separately. Their structure and design, with the cylinders arranged in line L, V or Y, are almost identical to the current ICEs.

Only their VCSR Crank Drive contains multiple planetary gears like those from the current vehicle automatic transmissions.

That means no special materials are required and the employees qualifications for an immediate large-scale industrial production are available.

Some figures of a three cylinder (as 3L or 3Y arranged) VCSR ICE are already presented in Fig. 3-1 to Fig. 3-5.

6th Criterion: RETROFIT capability to convert all old Euro 5 and current Euro 6 Vehicles to either CO2-Neutral by H2 fueling or, at least, CO2-Low-Emission Vehicles by blends of H2 & CNG fueling

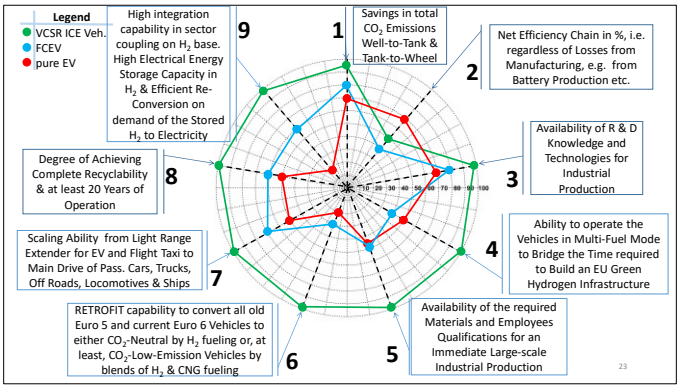

Figure 0. Graphic illustration of all nine criteria [4] applied to the three vehicle variants from legend. This figure is repeated here just as a reminder, i.e. only to improve the readability of the paper!

All the current diesel and gasoline engines of Euro 5 and Euro 6 vehicles can be completely replaced by or retrofitted to VCSR ICE with UD LC, i.e. operated stoichiometrically and fueled by H_2 (either pure or blended with CNG).

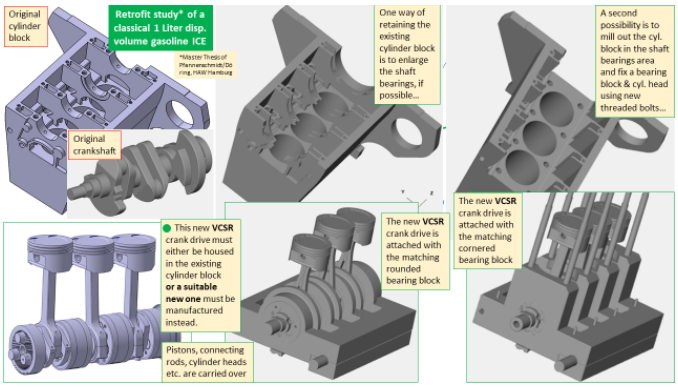

Figure 6-1. Retrofit study [18] of a classical SI 1L displacement volume ICE

The more than 1.5 million new cars registered in Germany between 2017 and 2020 (see Fig. 6-2) can be inexpensively converted to CO_2-neutral vehicles by means of retrofitting, see Fig. 6-1, and H_2 fueling instead of being completely scrapped!

Scrapping them would cause severe damage to both the environment and the economy!

Whether replaced or retrofitted, these vehicles should be equipped supplementary with the following parts:

a) H_2 tanks,
b) H_2 sequential direct injection (**GasDI**) system,
c) suitable Engine Control Unit (**ECU**) and
d) Three-way catalyst (if not already present) must be added in order to convert them to CO_2-Neutral/Poor vehicles!

If the developments presented here are introduced across the EU or only in some willing Member States within the next five years, the EU climate targets for 2050 can be achieved already 10 to 20 years ahead of schedule!

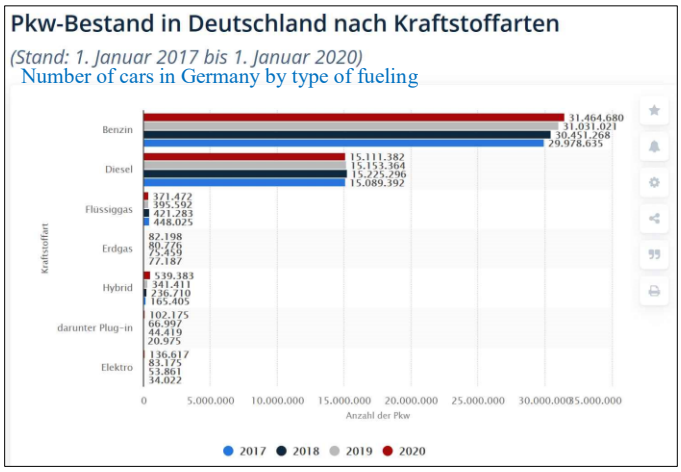

Figure 6-2. Evolution of the number of cars in Germany by fuel type

The development and manufacturing of new vehicle models with VCSR ICE, UD load control and fueled by H_2 (either pure or blended with CNG), as well as the retrofitting of the current Euro 5 and 6 vehicles will create thousands of jobs or secure existing ones for a long time.

Most of the retrofitting of the current Euro 5 and 6 vehicles should be done either directly by the vehicles automakers or by their suppliers.

The biggest political question is whether automakers should recall and retrofit their vehicles voluntarily or have to be forced by governments by means of drastic CO_2 taxation?!

A large number of SMEs should specialize in this field, which will be a driving force for the automotive industry in particular, as well as sustainable mobility in general.

The EU and its Member States should support such retrofitting conversions with grants (as is currently and undeservedly done for EVs, s. 1st Criterion for the explanation). The vehicle owners should also shoulder some of the cost (because their vehicles will be thoroughly renewed and both their value and service life will increase significantly). In any case, the retrofitting should be profitable for the retrofitters.

Large Photovoltaic (PV) fields and wind turbines (on- or off-shore) entities, alkaline or better PEM electrolyzers, huge H_2 storage capacity and ICE Power Plants can be built, e.g. in the decommissioned lignite mining areas or off-shore, in order to convert the stored energy back into electricity on site.

This means that the former staff of the closing brown coal mining industry can find new employment on site without special and expensive retraining.

The goals are to decentralize and distribute the storage and reconversion of sustainable electricity without having to add expensive, new and unpopular high-voltage networks across the EU and its Member States (or anywhere else).

7th Criterion: Scaling Ability from Light Range Extender for EV and Flight Taxi to Main Drive of Passenger Cars, Trucks, Off Roads, Locomotives and Ships

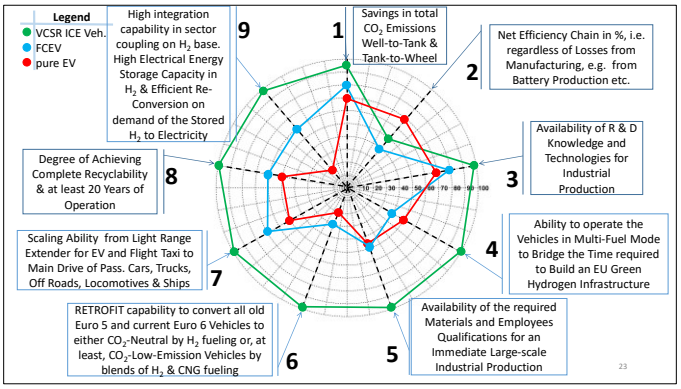

Figure 0. Graphic illustration of all nine criteria [4] applied to the three vehicle variants from legend. This figure is repeated here just as a reminder, i.e. only to improve the readability of the paper!

Electric mobility is suitable for light vehicles; see as well the comment in Introduction under e) of Andreas Renschler, former Traton chairman and VW board member, FAS [71].

A possible transformation of a FCEV into a VCSR ICE Vehicle is presented in Fig. 7-1. One of the battery blocks in the bottom design is superfluous. The fuel cell FC block can be replaced with a VCSR ICE. The hydrogen storage unit remains preserved.

The new drive unit is composed of an VCSR ICE with electrical Generator/Motor a battery stack for recuperation of break energy and for short pure electrical drive, e.g. start/stop capability, parking or creep drive behavior. The powertrain can be carry out either purely mechanical or better as full hybrid, like [17].

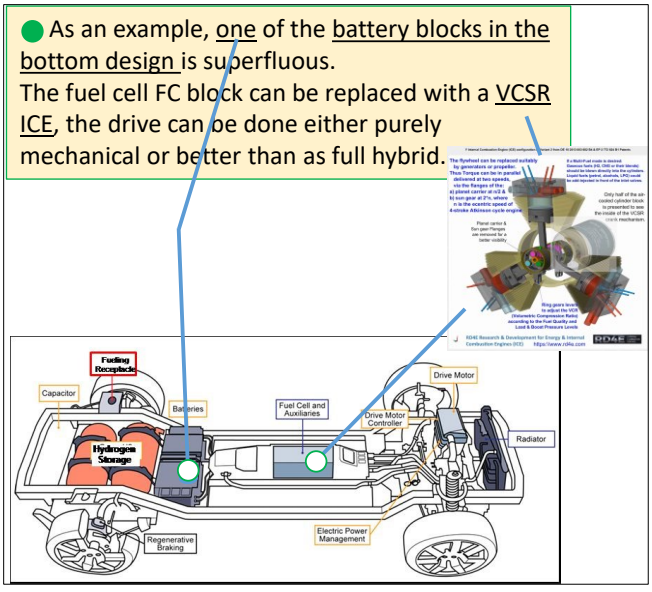

Figure 7-1. A possible transformation of a FCEV into VCSR ICE Vehicle

A possible transformation of the Volocity / Volocopter from pure EV to hydrogen fueled VCSR ICE is presented in Fig. 7-2. For this purpose, a part of its actual batteries is superfluous. The adding of H_2 Tanks (see below in white between his hooves) and the VCSR ICE Range Extender lead to reducing the vehicle's own weight, as well as increasing its flight range, flight time and load weight considerably.

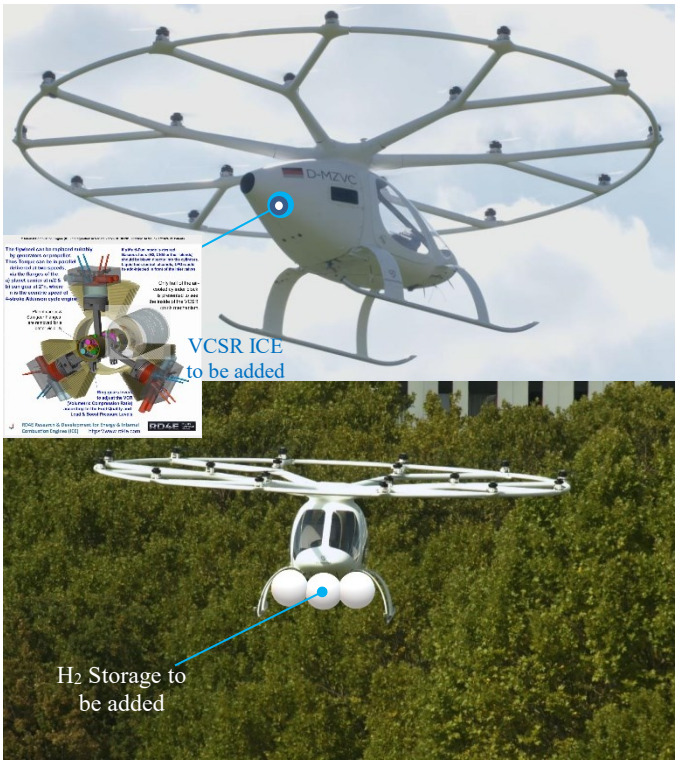

Figure 7-2. Proposed new Design of Volocopter, Volocity Flight-Taxi.

The range and autonomy specs of the Volocity s. Fig. 7-3 are modest.

1 General	
Capacity	2 pax incl. hand luggage
Aspired Certification	EASA SC-VTOL, category enhanced
Power type	Electric / batteries
2 Performance	
Max. take-off mass (MTOM)	900 kg
Max. payload	200 kg
Operating weight empty (OWE)	700 kg
Range	35 km
Max. airspeed	110 km/h
3 Structures	
Materials used	Composite
Overall height	2,5 m
Diameter of the rotor rim incl. rotor	11,3 m
Diameter of the rotor rim excl. rotor	9,3 m
Diameter of a single rotor	2,3 m
Number of rotors	18
4 Powertrain	
a) Power supply & battery	
Power supply	9 battery packs
Battery type	Lithium-ion
Battery system	Exchangable rechargable batttery packs
Battery swapping time	5 mins
b) Motors	
Engine type	Brushless DC electric motor (BLDC)
Number of motors	18

Figure 7-3. Actual Specifications of Volocopter, Volocity Flight-Taxi.

Another example and competitor of Volocity is shown in Fig. 7-4 for the CityAirbus Flight-Taxi.

The design modifications proposed for the Volocity / Volocopter are valid as well for the CityAirbus Flight-Taxi. By implementing of these modifications, the range and autonomy of the Flight-Taxis increase tenfold or more, s. Fig. 7-5.

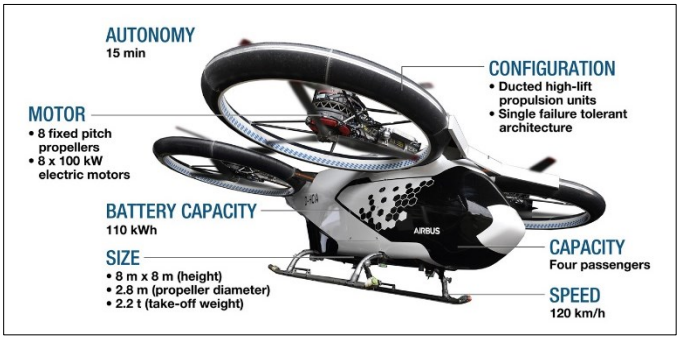

Figure 7-4. The Design and the specifications of CityAirbus Flight-Taxi.

Henry Fords's optimistic 1940 prediction that passenger cars will soon be able to fly has proven wrong so far.

Even the current hype about the purely electrically operated Flight-Taxis, as shown in Fig. 7-2, Fig. 7-4, Fig. 7-6 and Table 7-1, seems to be unfounded when using the currently available batteries.

Some reasons for the failure of air taxis in the pure eVTOL configurations, i.e. without a range extender, are presented below:

- The wingless eVTOL have a low specific energy density of the actual batteries, that leads to a high batteries mass (estimated, without their cooling system) for one or maximal two pax, 15 minute and maximum 50 km fly autonomy.
- The winged eVTOL have considerably higher flight ranges, capacity (number of pax/seats) and autonomy (flight time), see [22] for more details and comments.
- The energy of the batteries is not sufficient to assure an emergency restart (i.e. touch and go maneuver) without a recharge. The particularly scarce energy of the batteries is not sufficient to carry out a safe flight under severe atmospheric conditions (strong frontal winds or crosswinds).

Table 7-1. Published, estimated, assumed and computed parameter of some Flight-Taxis eVTOLs.

Parameter	Unit	Symbol	E-Hang 184	CityAirbus	Volocity	Lilium [22]	Source
Maximum E Motors Power	kW	P_EM	106	800	270	360	estimated
Number of E Motors (Fans)		n_EM	8	8	18	36	published
Total Batteries Energy	kWh	E_batt	14.4	110	39	95	
Battery Power = P_batt_m *m_batt	kW	P_batt	67.4	515.0	182.6	610.1	computed
Net Mass	kg	m_net	260	1800	700	1700	
Capacity, Number of Pax + Pilot		n_pax	1	4	2	5	
Rated Payload Weight (RPW)	kg	m_pax	100	400	200	500	
Maximal Take-off Mass (MTOM)	kg	m_max	360	2200	900	2200	
Autonomy, Total Flight Time	min	t_flight	23	15	15	55	
Flight Range	km	L_range	35	35	35	245	
Averaged Flight Speed, Cruise Speed	km/h	v_cruise	100	120	110	290	
Battery Mass = E_batt / E_batt_m	kg	m_batt	92	701	248	830	assumed
Battery energy specific density	kWh/kg	E_batt_m	0.157	0.157	0.157	0.157	by Tesla
Battery power density	kW/kg	P_batt_m	0.735	0.735	0.735	0.735	by Tesla
E_batt/m_max	kWh/kg		0.040	0.050	0.043	0.043	estimated
P_EM/m_max	kW/kg		0.29	0.36	0.30	0.16	
single E Motor Power	kW	P_1EM	13.25	100	15	10	
m_batt/m_net	%		35.3	38.9	35.5	48.8	

Potential Hydrogen Fueling Capacity of the Volocopter (an estimation)

$W_{hooves} := 2 \cdot m$ Distances between hooves

$L_{hooves} := 2.1 \cdot m$ Hooves lenght

$H_{hooves} := 0.7 \cdot m$ Hooves high

$V_{H2} := W_{hooves} \cdot L_{hooves} \cdot H_{hooves}$ Maximal Hydrogen Tanks volums between the hooves

$V_{H2} = 2.94\, m^3$

$\eta_{iVCSR} := 0.5$ indicated Efficiency of the VCSR ICE

$\eta_m := 0.95$ mechanical Efficiency of the VCSR ICE and electric motors and other losses

$\eta_e := \eta_{iVCSR}\, \eta_m$ $\eta_e = 0.475$ effective Efficiency

$H_{uH2} := 120 \cdot \frac{MJ}{kg}$ H_2 lower heating value, see Table 1

$\rho_{H2\_350bar} := 24 \cdot \frac{kg}{m^3}$ Hydrogen Density at 350 bar, see Fig. 12

$\rho_{H2\_700bar} := 40 \cdot \frac{kg}{m^3}$ Hydrogen Density at 700 bar, see Fig. 12

$m_{H2\_350bar} := V_{H2} \cdot \rho_{H2\_350bar}$ $m_{H2\_350bar} = 70.56\, kg$ available H_2 Mass

$m_{H2\_700bar} := V_{H2} \cdot \rho_{H2\_700bar}$ $m_{H2\_700bar} = 117.6\, kg$

$E_{H2\_350bar} := m_{H2\_350bar} \cdot H_{uH2} \cdot \eta_e$ $E_{H2\_350bar} = 1.117 \times 10^3\, kWh$ available H_2 Energy

$E_{H2\_700bar} := m_{H2\_700bar} \cdot H_{uH2} \cdot \eta_e$ $E_{H2\_700bar} = 1.862 \times 10^3\, kWh$

CityAirbus reachs with 110 kWh battery capacity a range of 35 km.
The situation by Volocity is nearly the same! That means the ranges by using VCSR ICE and Hydrogen in place of battery could be:

$Range_{350bar} := \frac{E_{H2\_350bar}}{110 \cdot kWh} \cdot 35 \cdot km$ $Range_{350bar} = 355.473\, km$

$Range_{700bar} := \frac{E_{H2\_700bar}}{110 \cdot kWh} \cdot 35 \cdot km$ $Range_{700bar} = 592.455\, km$

Figure 7-5. Estimated specifications for CityAirbus or Volocity/Volocopter or other Flight-Taxis, by using a hydrogen-fueled VCSR ICE Range Extender.

Figure 7-6. Lilium Jet five-seater geometry.

8th Degree of Achieving Complete Recyclability & at Least 20 Years of Operation

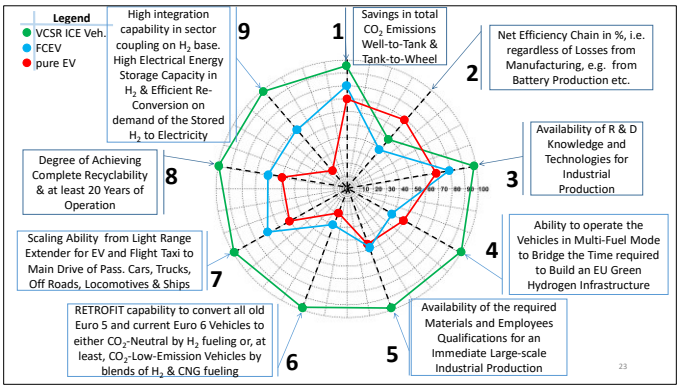

Figure 0. Graphic illustration of all nine criteria [4] applied to the three vehicle variants from legend. This figure is repeated here just as a reminder, i.e. only to improve the readability of the paper!

The recycling of a VCSR-ICE and hydrogen high-pressure storage unit is similar to that of a conventional vehicle. This means that full recycling is relatively easy and familiar. The batteries of EVs and the membranes and electrodes of PEM FCs lose efficiency relatively quickly due to obsolescence. However, obsolescence is not a relevant issue for the VCSR-ICE, i.e. this is similar to the current vehicles.

The recycling of EV batteries focuses on these substances:

- A drive battery contains a lot of aluminum, steel and plastics.
- There is a battery of around 400 kilograms with a capacity of 50 kWh.
- 6 kg lithium, 10 kg of manganese, 11 kg cobalt, 32 kg of nickel, 100 kg graphite.

In order to achieve the highest possible recovery rate in future recycling, battery design must be largely standardized and the recycling process should have several precisely planed steps:

- It starts with manual disassembly of a battery system.
- This is followed by sorting, shredding and thermal melting.
- At the end of the process, there is material separation (purely chemical or electro-chemical).
- A large part of the battery materials can already be recovered using today's technology and methods, but some of the process steps are still too energy consuming, too expensive and too polluting for the environment.
- The recycling process must be designed in such a way as to be economical.
- The questions are:
    - Where does the money come from?
    - Does the value of the products matter?
    - Should every entity that puts battery in circulation pay a disposal fee to the recycling company?

To simplify the process of drawing conclusions, the resources/environment ratings were combined, as were the function/characteristics ratings.

The results from 2016 are shown in Fig. 6, S. 69, of [**16**] for the following batteries and Fig. 8-1:

1. Lithium-ion C - LNMC / LMO: (carbon - lithium-nickel-manganese-cobalt oxide / manganese oxide)
2. Lithium-ion C-LNMC / LNCA: (Carbon - lithium-nickel-manganese-cobalt oxide / manganese oxide / lithium-nickel-cobalt-aluminum oxide)
3. Lithium-ion C - LFP: Carbon - lithium iron phosphate
4. Lithium-ion LTO - LFP: titanium oxide - lithium iron phosphate
5. Redox flow: Cr-Fe with aqueous acidic electrolytes (iron-chromium)
6. Redox flow: V-V with aqueous-acidic electrolytes (vanadium-vanadium)
7. Sodium-sulfur: Na-S
8. Zinc-air: Zn-air

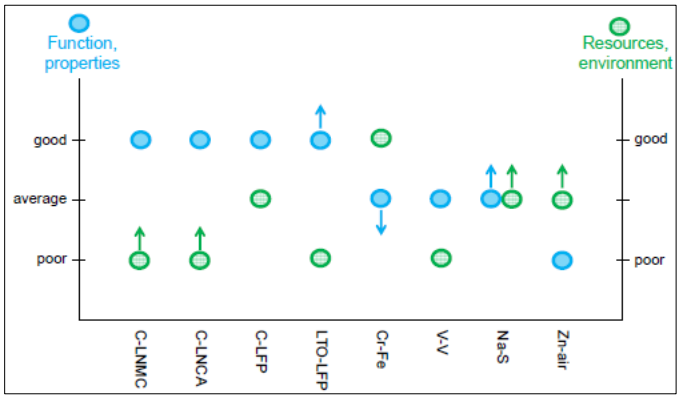

Figure 8-1. Diagrammatic representation of the ratings of the stationary short-term storage systems (batteries). Source [16], Fig. 6, S. 69

If one starts by considering the LTO-LFP li-ion battery, which scores best on functionality and characteristics, one notices that this battery also scores worst in terms of resource-related and environmental criteria. On the other hand, the Cr-Fe redox flow battery, which stands out as the best in terms of resources and the environment, is the second-worst in terms of characteristics and functionality, having the second-worst efficiency and the highest costs. Consideration of battery characteristics and functionality, which the assessment focused on first, shows that it is the Li-ion batteries that perform best. Apart from LTO-LFP, treated above, C-LFP represents a good compromise. Unlike all the other Li-ion batteries, C-LFP is at least rated neutral in terms of demand relevance. After the Li-ion batteries, Na-S has the next-best efficiency and is the best of all the batteries from the point of view of resources. After the Li-ion batteries, Na-S therefore represents a good alternative. Of all the innovative battery systems considered, the V-V and Zn-air batteries are the worst rated [**16**].

Li-ion batteries for mobility

In the mobility field, the four different Li-ion batteries were compared and rated as possible options.
All four variants score equally well on the very important criterion of efficiency. However, specific energy is a key consideration in mobility applications.
LTO-LFP has a very low specific energy and is therefore of limited usefulness in connection with battery-powered electric vehicles. However, its high charge/discharge rate means that it is likely to be used in hybrid vehicles. For all-battery vehicles, the LTO-LFP battery's 50 Wh/kg is the worst, while at 102 Wh/kg the C-LNCA battery performs best. This means that for an LTO-LFP battery to store the same amount of energy as a C-LNCA one, it needs to be twice as heavy. A 40 kWh LTO-LFP battery for an all-electric car would weigh around 800 kg. In addition and as explained above in

connection with stationary batteries, LTO-LFP is the worst performing of all the batteries in terms of resource and environmental criteria. In light of these considerations, therefore, LTO-LFP is not a candidate for use in mobility, or at least not in all-electric vehicles. Among the remaining three Li-ion batteries, the assessment of stationary batteries has already identified C-LFP as the best option. From the point of view of resources, this rating remains correct. In mobile applications, however, C-LFP is the second-worst option in terms of specific energy since, with a specific energy of only 76 Wh/kg, it performs worse than all the other options except LTO-LFP. C-LNCA has the highest specific energy at 102 Wh/kg (C-LNMC 92 Wh/kg). In addition, C-LNCA requires less cobalt, lithium and graphite than C-LNMC. C-LNCA is therefore to be preferred over C-LNMC [**16**].

9th High Integration Capability in Sector Coupling on Hydrogen H_2 base. High Electrical Energy Storage Capacity by H_2 Production & Efficient Re-Conversion on Demand of the Stored H_2 to Electricity by Means of ICE Power Plants Based on VCSR ICE and Driven Electrical Generators

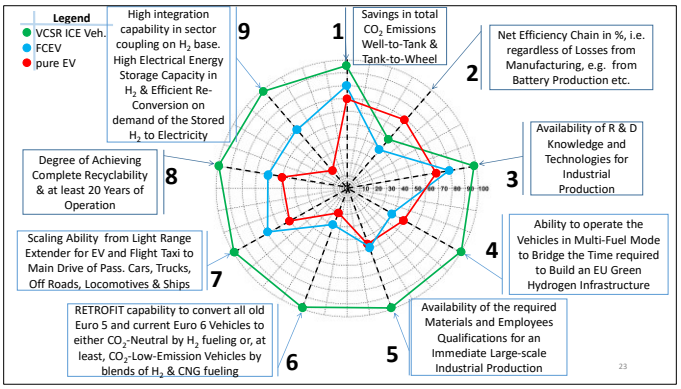

Figure 0. Graphic illustration of all nine criteria [4] applied to the three vehicle variants from legend. This figure is repeated here just as a reminder, i.e. only to improve the readability of the paper!

Some Facts about ICE Power Plants:

- Reliable: ICE Power Plants guarantee a safe and stable power supply everywhere: from vibrant cities to remote locations.
- Efficient: The efficiency of ICE Power Plants is up to 95 percent in cogeneration, i.e. electric energy and district heating generation, applications.
- Sustainable: ICE Power Plants operate with very low emission levels and are CO_2-neutral with biofuels and especially with stored hydrogen.
- Responsive: Ready, steady, go: The energy supplied by ICE Power Plants corresponds dynamically with actual energy demand.
- Fast: ICE Power Plants provide energy right away at any time even in emergencies.
- Modularity: The integration of more and more intermittent renewable energy into, e.g. the European, electricity grid generates the need for a very flexible and fast backup solution to ensure the supply when no sufficient energy can be generated from sun and wind. This task can easily be performed by ICE Power Plants, which are running within minutes of start up and can provide the correct electricity needed, thanks to their modularity.

From base-load security to intelligent backup: The role of the ICE Power Plant has changed over the past few years. Today, it still serves to secure the base load, but it has also become an indispensable backup that compensates for weather-related fluctuations of renewable energy sources. The engines are usually intended to run at 80% load and thus to generate electricity and district heating and the remaining 20% serving as a variable reserve.

The output of the engines can be increased at any time to compensate for grid fluctuations and can be throttled back when the weather conditions are favorable. Thanks to this setup, ICE Power Plants, see Fig. 9-2, Fig. 9-3 and Fig. 9-5 can exploit the full potential of renewable energy while guaranteeing maximum grid stability.

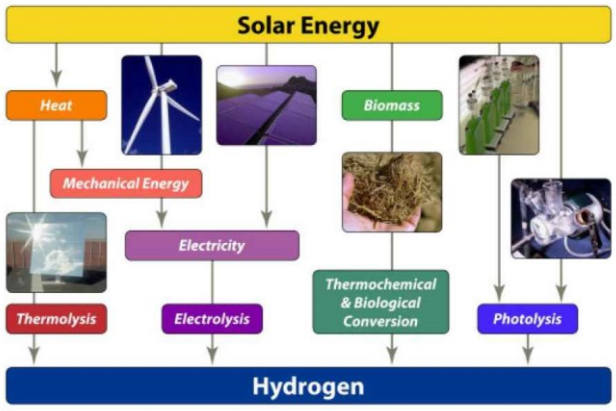

Figure 1. Renewable pathways for hydrogen production.

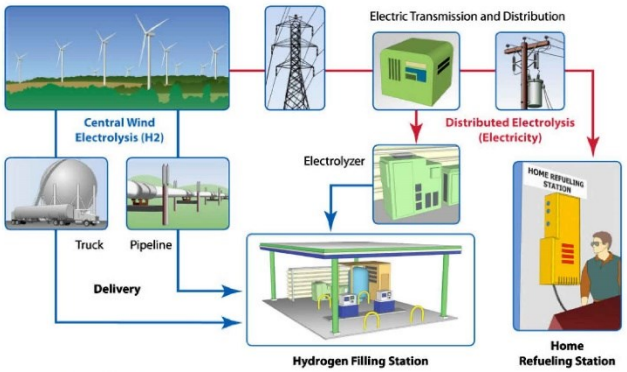

Figure 3. Central hydrogen production *versus* distributed hydrogen production *via* electrolysis.

Int. J. Energy Res. (2007)
DOI: 10.1002/er

Figure 9-1, Renewable pathways for hydrogen production and distribution in 2007, source (s. details on the figure below)

Figure 9-2, ICE Power Plant of MAN SE is a part of the microgrid of the Faroe Island energy system. The isolated energy system in the Faroe Islands is an impressive example of how all available energy resources can be integrated into an intelligent and innovative microgrid.

Figure 9-3. ICE power plant. Floating or onshore ICE power plants can be used in the bays near the offshore wind turbines. When there is no wind, these can produce electricity from the stored hydrogen and thus compensate for the resulting lack of electricity in the network and greatly reduce or avoid fluctuations in electricity production.

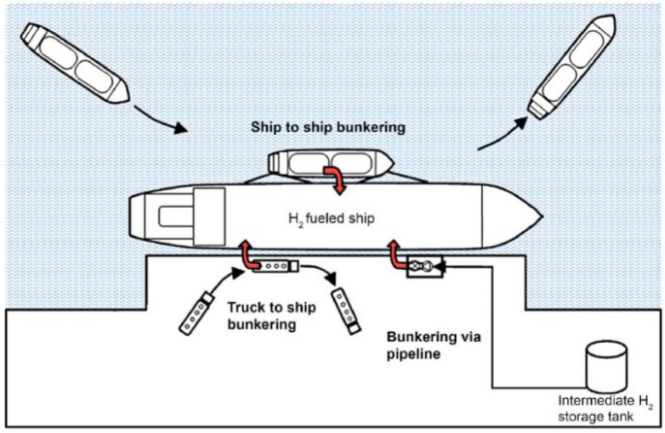

Figure 9-4. Three possible ways of bunkering conceivable for hydrogen.

Figure 9-5, Interplay between ICE Power Plant of MAN SE and LNG terminal in the port of Gibraltar

	Transportation Applications	Chemicals and Industrial Applications	Stationary and Power Generation Applications	Integrated/Hybrid Energy Systems
Existing Growing Demands	• Material-Handling Equipment • Buses • Light-Duty Vehicles	• Oil Refining • Ammonia • Methanol	• Distrubuted Generation: Primary and Backup Power	• Renewable Grid Integration (with storage and other ancillary services)
Emerging Future Demands	• Medium-and Heavy-Duty Vehicles • Rail • Maritime • Aviation • Contruction Equipment	• Steel and Cement Manufacturing • Industrial Heat • Bio/Synthetic Fuels	• Reversible Fuel Cells • Hydrogen Combustion • Long-Duration Energy Storage	• Nuclear/Hydrogen Hybrids • Gas/Coal/Hydrogen Hybrids with CCUS • Hydrogen Blending

Figure 9-6, Existing and emerging demands for hydrogen, CCUS means carbon capture, utilization, and storage on 2020; source Figure1, p. 9, [**21**]

Key Aspects of the Hydrogen Energy System see Fig. 9-8

CONVERSION: To be useful, the energy carried by hydrogen must be converted into a different form, such as electricity or heat, and this can be accomplished through electrochemical conversion using fuel cells, or via combustion using turbines or **reciprocating engines**. Hybrid systems, such as natural gas/other fuel combined cycle fuel cell systems offer high efficiencies and reduced emissions compared with conventional technologies.

Needs and Challenges see Fig. 9-6

• Low-cost, more-durable, and more-reliable fuel cells that can be mass-produced
• Turbines that can operate on high concentrations of hydrogen or pure hydrogen
• Development and demonstration of large-scale hybrid systems
• Design for recyclability and waste reduction
• Current consumption, Table 2, p.14, [**21**], shows today's total hydrogen demand is 10 million metric tonnes (MMT)/year.
The future expected economic consumption of hydrogen in the United States in 2050 for transportation alone, will reache 17 MMT/year, while the overall demand will be 41 MMT/year.

Hydrogen Production Targets: see Fig. 9-1 and Fig. 9-7

Affordable hydrogen from diverse domestic resources:

• <$2/kg for transportation and uses
• <$1/kg for industrial and bulk power/polygeneration applications

Hydrogen Delivery Targets: see Fig. 9.4

Large-scale hydrogen delivery, distribution, and dispensing at:

• <$5/kg for transportation and uses in early markets
• <$2/kg for ultimate market expansion for high value products

Hydrogen Storage Targets: see Fig. 9-4 and Fig. 9-5

• Onboard hydrogen storage systems for transportation: $8/kWh stored at 2.2 kWh/kg and 1.7 kWh/L
• Rechargeable portable power systems: $0.5/kWh stored at 1.0 kWh/kg and 1.3 kWh/L
• High-volume cost of high-strength carbon fiber for tanks: $13/kg

Hydrogen Combustion Targets:

• Enable wider range of acceptable hydrogen concentrations (up to 100%) in simple and combined cycles
• Improve understanding of combustion behavior and optimization of component designs for low NOx combustion
• Apply and develop advanced computational fluid dynamics with reacting flows
• Develop advanced manufacturing techniques for combustors
• Develop new materials, coatings, and cooling schemes
• Optimize conversion efficiency
• Improve durability and lifetime and lower costs, including for operations and maintenance
• Develop system-level optimization and control schemes
• Assess and mitigate moisture content effects on heat transfer and ceramic recession
• Develop and test hydrogen combustion retrofit packages
• Enable combustion of carbon neutral fuels (i.e., NH3, ethanol vapor)

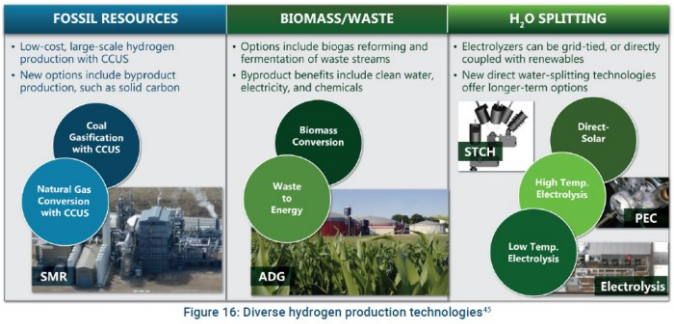

Figure 16: Diverse hydrogen production technologies[45]
(SMR= steam methane reforming; CCUS= carbon capture, utilization, and storage; ADG= anaerobic digester gas; STCH= solar thermochemical hydrogen; PEC= photo-electrochemical water splitting)

Figure 9-7, Diverse actual and future Hydrogen Production Technologies, source Figure 16, p.19, [21].

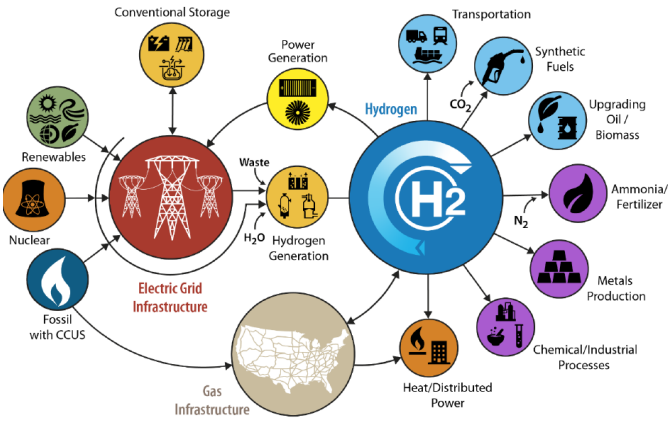

Figure 9-8, Conceptual H2@Scale energy system; source Figure 3, p.13, [21].

PEMFC Target for Long-Haul Trucks:

• $80/kW fuel cell system cost
• 25,000-hour durability

Common RD&D Thrusts for PEMFCs:

• Reduce platinum group metal catalyst loading, through materials R&D
• High-temperature tolerant, low-cost, and durable membranes
• Improved component-design and materials integration to optimize manufacturable and scalable electrode structures for membrane electrode assemblies
• Internal reforming of carbon neutral fuels for directly fed fuel cells
• Accelerated stress tests, improved understanding of degradation mechanisms, and mitigation approaches
• Improved balance-of-plant (BOP) components, including compressors and power electronics
• Standardized, modular stacks and systems for multiple heavy-duty applications
• Improved hybridization and optimized system design

SOFC Target for Stationary Power Generation:

• $900/kW fuel cell system cost
• 40,000 hour durability

Common RD&D Thrusts for SOFCs:

• Materials R&D to reduce cost and address issues related to high-temperature operation
• Management of heat and gas flow across the stack
• Addressing stack and BOP systems integration, controls, and optimization for load following and modular applications
• Improved BOP components, including compressors and power electronics
• Standardized, modular stacks
• Improved understanding of impacts of impurities on materials and performance
• System design, hybridization and optimization, including for reversible fuel cells

Common RD&D Thrusts for Hydrogen and Related Technology Applications

• Development of rigorous application-specific targets for hydrogen utilization
• Materials compatibility issues in diverse end uses
• Reduced cost and improved durability and efficiency in industrial-scale electrolyzers, fuel cell systems, combustion turbines and engines, as well as in hybrid systems
• Component- and system-level integration and optimization, including balance of plant components and systems
• Optimized controls of integrated systems, including cybersecurity
• Manufacturing and scale-up, including process intensification
• Harmonized codes and standards, including refueling protocols
• Capacity expansion models to identify value propositions for use of hydrogen in new applications

References

1. Gheorghiu, V. "VCSR-aided Ultra-Downsizing of Internal Combustion Engines", Presentation (pdf), 2019
2. Gheorghiu, V. "Ultra-Downsizing of Internal Combustion Engines", SAE 2015-01-1252, World Congress, April 2015, Detroit, USA, doi:10.4271/2015-01-1252.
3. Gheorghiu, V. „Thesis 10: The VCSR ICE solution is at least 25% more effective than the classic ICE one. Proof of the increased efficiency of VCSR ICE in relation to classic ICE, Short Presentation (pdf), (so far only in German), 2020
4. Gheorghiu, V. „Thesis 07: Justification of the economic viability of the proposed solution and Efficiency advantage of the VCSR ICE with UD Load Control operated with H2 as the main drive source for sustainable mobility, instead of EV and FCEV, as well as for the Re-Conversion of stored H2 to electricity. Short Presentation as Spider- or Radar-Chart". (pdf), (so far only in German), 2020
5. Gheorghiu, V. "Sustainable Mobility & Energy Transition in a Changing Climate" Presentation (html) (so far only in German), 2019
6. Buchal, C., Karl, H.D., Sinn H.W. „Kohlemotoren, Windmotoren und Dieselmotoren: Was zeigt die CO_2-Bilanz? Coal engines, Wind engines and Diesel engines: What does the CO_2 balance?" 2019 (in German)
7. ADAC, DE, Joanneum Research AT, "The EV need the energy transition: the climate balance", 2019 (in German)
8. Eichlseder, H., Klell, M., „Wasserstoff in der Fahrzeugtechnik", Springer Link, 2018, doi:10.1007/978-3-658-20447-1
9. Romare, M. und L. Dahllöf (2017), "The Life Cycle Energy Consumption and Greenhouse Gas Emissions from Lithium-Ion Batteries: A Study with Focus on Current Technology and Batteries for Light-duty Vehicles", Swedish Environmental Research Institute, Stockholm.
10. Gheorghiu, V. „Verfahren zur Laststeuerung und Zylinderabschaltung einer Brennkraftmaschine arbeitend nach dem realen Viertakt-Atkinson-Zyklus", „Method for load control and cylinder deactivation of an internal combustion engine operating according to the true four-stroke Atkinson cycle", Patent DE102013003682B4, 2018
11. Gheorghiu, V. „Brennkraftmaschine arbeitend nach dem realen Viertakt-Atkinson-Zyklus und Verfahren zu ihrer Laststeuerung", „Internal combustion engine operating according to the true four-stroke Atkinson cycle and method for load control", Patent EP 2 772 624 B1, 2020
12. Gerke, U. "Numerical analysis of mixture formation and combustion in a hydrogen direct-injection internal combustion engine", PhD Thesis, 2007, doi:10.3929/ethz-a-005540349
13. Martinsa, D., Frank, T., et al. "Reconfigurability in Mechanisms for Atkinson Cycle Engines", ScienceDirect, Mechanism and Machine Theory 00 (2016), Published by Elsevier Ltd, Springer Link.
14. BMW Hydrogen Storage. CCH_2 –Cryogenic Gas Denser than LH_2
15. Development of 70 MPa Differential-pressure Water Electrolysis Stack, Article of Honda R&D Technical Review Vol.28 No.1
16. UBA Umwelt Bundes Amt, „Ableitung von Recycling und Umweltanforderungen" 07, 2016, UBA German Federal Environment Agency, „Derivation of Recycling and Environmental Requirements", 07, 2016
17. Muta, K. et al. „Development of New-Generation Hybrid System THS II – Drastic Improvement of Power Performance and Fuel Economy", Toyota Motor Corp., SAE 2004-01-0064
18. Pfannenschmidt/Döring, M. „Implementation of the VCSR crank mechanism on an existing 3 cylinder gasoline engine" Master Thesis, HAW Hamburg University of Applied Sciences, 2015
19. Plötz, P., Moll, C., Bieker, G., Mock, P., Li, Y., "Real-world usage of plug-in hybrid electric vehicles – Fuel consumption, electric driving, and CO2 emissions", Fraunhofer Institute for Systems and Innovation Research ISI, 2020
20. Baehr, H. D., Kabelac, S. " Thermodynamic", Springer, 2016, doi:10.1007/978-3-662-49568-1
21. Hydrogen Program Plan. US Department of Energy.2020
22. Bacchini, A., Cestino, E. Electric VTOL Configurations Comparisons, Aerospace-06-000.26, doi:10.3390/aerospace6030026
23. Short Video of 3Y Variant of VCSR engine doing by using of Matlab, Simulink, Simscape simulations.
24. Ho Lung Yip et al., "A Review of Hydrogen Direct Injection for Internal Combustion Engines: Towards Carbon-Free Combustion", MDPI, 2019.
25. Schutting, E., Neureiter, A., Fuchs, Ch., Schwarzenberger, T. et al., "Miller- and Atkinson-Cycle for Supercharged Diesel Engines", MTZ 06, 2007 (German).
26. Schutting, E., Dumböck, O., Eichlseder, H., TU Graz, Austria, Hübner, W., Schmidt, Ch., BMW Forschung und Technik GmbH, München. "Diagnostics of Spark an Ignition Engine with Extended Expansion – Challenges and Approaches", Internationales Symposium für Verbrennungsdiagnostik, Baden-Baden 2014.
27. Gheorghiu, V. „Thesis 00: "Theses on sustainable mobility & sustainable energy system transition against global warming" Presentation (2021)
28. Gheorghiu, V. "Milestones on the R&D path to VCSR ICE" short Presentation (2021)
29. Gheorghiu, V. "Sustainable Mobility by use of H2 fueled ICE" short Presentation (2021)

Contact Information

Victor GHEORGHIU

Prof. Emeritus PhD ME

Hamburg University of Applied Sciences, Faculty TI
Dpt. of Mechanical Engineering
Berliner Tor 21
20099 Hamburg, Germany
victor.gheorghiu@haw-hamburg.de
https://www.victor-gheorghiu.de/
https://www.rd4e.com
grg@rd4e.com
Mailing address
Berner Str. 64
22145 Hamburg, Germany
Tel.: +49 40 6489 2585

Abbreviations

Internal Combustion Engines	**ICE**
Electrical Vehicle	**EV**
Fuel Cell Electrical Vehicle	**FCEV**
Variable Compression and Stroke Ratios	**VCSR**
Ultra-Downsizing	**UD**
Load Control	**LC**
Air Fuel Equivalence Ratio	**AFR**
Volumetric Compression Ratio	**VCR**
Volumetric Expansion Ratio	**VER**
Indicated Fuel Conversion Efficiency	**IFCE**
Indicated Mean Pressure	**IMEP**
GreenHouse Gas emissions	**GHG**
Specific (i.e. related to mass)	**sp.**
stoichiometric	**stoich.**
relative (non-dimensional)	**rel.**
Calorical Equation	**CE**
State Equation	**SE**
Law of Thermodynamics	**LoT**
First Law of Thermodynamics	**1.LoT**
Second Law of Thermodynamics	**2.LoT**
Turbocharger	**TC**
Turbine of TC	**T**
Compressor of TC	**C**
True Atkinson cycle	**A cycle**
Otto (Gasoline engine) cycle	**O cycle**
Gas Turbine cycle	**TC cycle**
proportional	**∼**
Top Dead Center	**TDC**
Bottom Dead Center	**BDC**
Gas exchange TDC	**gasex. TDC**
Gas exchange BDC	**gasex. BDC**
intake valve open	**io**
intake valve closed	**ic**
exhaust valve open	**eo**
exhaust valve closed	**ec**

Foot Indices

p	isobaric
v	isochoric
t	technical
c	compression
e	expansion
0	environment state
A	Atkinson cycle
O	Otto cycle
TC	Gas Turbine (TC) cycle
1, 2, 3, 4	thermodynamic states

Head Indices

°	Ideal Gas Behavior

Definitions

Symbol	Meaning	Unit
v	specific Volume	m^3/kg
T	absolute (Kelvin) Temperature	K
p	Pressure	Pa, bar, MPa
m	Mass	kg
c^o_v	specific isochoric Heat Capacity	kJ/kg/K
c^o_p	specific isobaric Heat Capacity	kJ/kg/K
c	flow Speed	m/s
s	specific Entropy	kJ/kg/K
u	specific internal Energy	kJ/kg
h	specific Enthalpy	kJ/kg
q	specific Heat	kJ/kg
w_v	specific volume change Work	kJ/kg
w_p or y	specific pressure change Work	kJ/kg
w_t	specific technical Work	kJ/kg
j	specific irreversible Work	kJ/kg
R	Gas Constant of Air as Ideal Gas	kJ/kg/K
κ	isentropic Exponent	-
ε_c	**VCR** (Volumetric Compression Ratio)	-
ε_e	**VER** (Volumetric Expansion Ratio)	-
λ	Air Fuel Equivalence Ratio **AFR**	-
δ	Pressure-Rise Ratio during the heat release = combustion	-
γ	Compression to Expansion Volumetric Ratios, **VCR**/**VER**	-

Appendix 1. Comparison of the ideal cycles:

Comparison of the thermal efficiencies of the true Atkinson (A) and gasoline classic Otto (O) ICE ideal cycles, both with Bryton/Joule Gas Turbine ideal cycle (particular TC), while maintaining the same Temperature at the Exhaust beginning in all three cycles (i.e. under the same conditions)

In order to perform a suitable comparison of the efficiencies of the **Otto and Atkinson Cycles**:

a) The **VCR**, the isentropic exponent κ, a stoichiometrically **AFR**, and the pressure-rise ratio δ should be kept identical in both cycles.
b) As a consequences, the compression and expansion curves overlap, which inevitably leads to different amounts of released heat during the cycles!
c) In the true Atkinson Cycle, the fresh charge (air) for suction into **VCSR ICE** cylinders will be pre-compressed by means of high-pressure **T**urbo**C**harging (**TC**). The processes from **TC** are simulated here by means of the Brayton/Joule cycle.
d) The start of compression in the true Atkinson Cycle lays on the isentropic compression curve of the Otto Cycle, according to a) and b).
e) All cycles are designed so that the temperature upon entering the turbine (**T**) i.e. at the start of Exhaust, reaches about 1000°C.
f) The goal was to select the maximum exhaust gas temperature, which the turbine blades could tolerate without special cooling measures.

It is well known that the thermal efficiency of the **Otto Cycle** (i.e. of the Ideal Cycle of Gasoline ICEs) depends only on the Volumetric Compression Ratio ε_c (VCR) and the isentropic exponent κ of the working gas (air). Its thermodynamic efficiency is independent of the charging level, i.e. in the case of (turbo) charging, the states in the Otto Cycle are only shifted to higher temperatures and pressures, but its thermodynamic efficiency remains unchanged. That is the main weakness of the Otto Cycle, since in its case no direct heat recovery via turbocharging (TC) is available.

The Gas Turbine cycle is introduced here as representation of the processes within the TC (s. Figure A1-1); its heat release part is only assumed in order to close the cycle.

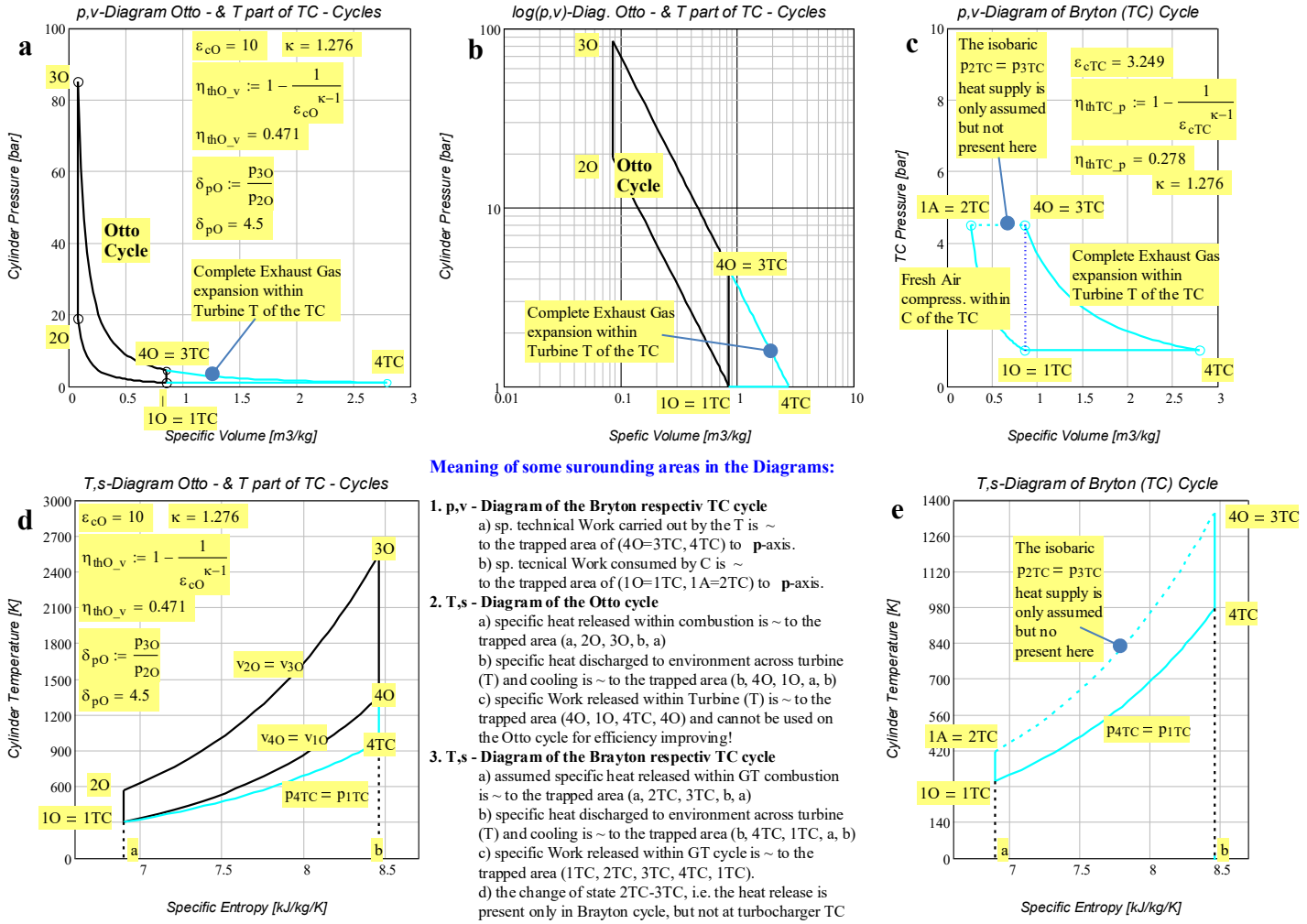

Meaning of some surounding areas in the Diagrams:

1. p,v - Diagram of the Bryton respectiv TC cycle
a) sp. technical Work carried out by the T is ~ to the trapped area of (4O=3TC, 4TC) to **p**-axis.
b) sp. tecnical Work consumed by C is ~ to the trapped area of (1O=1TC, 1A=2TC) to **p**-axis.

2. T,s - Diagram of the Otto cycle
a) specific heat released within combustion is ~ to the trapped area (a, 2O, 3O, b, a)
b) specific heat discharged to environment across turbine (T) and cooling is ~ to the trapped area (b, 4O, 1O, a, b)
c) specific Work released within Turbine (T) is ~ to the trapped area (4O, 1O, 4TC, 4O) and cannot be used on the Otto cycle for efficiency improving!

3. T,s - Diagram of the Brayton respectiv TC cycle
a) assumed specific heat released within GT combustion is ~ to the trapped area (a, 2TC, 3TC, b, a)
b) specific heat discharged to environment across turbine (T) and cooling is ~ to the trapped area (b, 4TC, 1TC, a, b)
c) specific Work released within GT cycle is ~ to the trapped area (1TC, 2TC, 3TC, 4TC, 1TC).
d) the change of state 2TC-3TC, i.e. the heat release is present only in Brayton cycle, but not at turbocharger TC

Figure A1-1. Graphic representation of the Otto and Gas Turbine cycles in p,v (pressure, specific volume) and T,s (Temperature, specific entropy) diagrams.

The true Atkinson Cycle results as an overlapping of Gas Turbine and Otto Cycles, where the common parts of both cycles merge. In the Atkinson cycle, a big part of the released specific work of the Turbine is fed back on the cycle as specific work for air pre-compression. As a result, the compression stroke can be significantly shortened and, thus, it starts from the pre-compression state, i.e. the compression stroke part from environment state to the pre-compression state can be omitted. However, the expansion strokes of the Atkinson and Otto cycles end in the same state (s. Figure A1-2). The thermodynamic substantiation is presented in Figures A1-3-1 to A1-3-3.

For a suitable comparison of the efficiencies of the **Otto & Atkinson Cycles**, some more conditions need to be discussed below:

In a **1st Comparison Variant**, the **pressure-rise ratios** $\delta_{pA\_v} = \delta_{pO\_v}$ during the **isochoric** (v) heat release are kept **identical** in Atkinson & Otto Cycles. This leads to a) very high-pressure peak p_{3A} and b) much higher released heat on the Atkinson Cycle (s. area a-2A-3A-b-a) compared to the Otto Cycle (s. area a-2O-3O-b-a in T,s-diag.). Although the isochoric amount of heat released is not explicitly present in the IFCE formulas, the **1st Comparison Variant** could be debatable because of the different high pressure peaks! Thus, the IFCE of the Atkinson cycle in this 1st Variant can be interpreted as its **upper** limit. In this variant, the IFCE value of Atkinson cycle is over 30% higher compared to the IFCE value of the Otto cycle.

In a **2nd Comparison Variant**, the **maximal pressure** values are kept **identical** in both cycles, which implies an **isobaric** (p) heat release on the Atkinson cycle. That leads to moderate heat release on the Atkinson Cycle (s. area a-2A-**3O=3Ap**-b-a in T,s-diagram) compared to the Otto Cycle. The δ_{pO_v} during the isochoric heat release of the Otto cycle appears this time explicitly in the IFCE formula of Atkinson cycle, because δ_{pO_v} governs the maximal pressure level on both cycles. Thus, the IFCE of the Atkinson cycle in this 2nd Variant can be interpreted as its **lower** limit. Even in this worst-case heat release variant, the IFCE value of Atkinson cycle is over 13% higher compared to the IFCE value of the Otto cycle (s. the bottom half of Figure A1-3-3).
Just a reminder: **All three cycles are designed to reach a temperature of around 1000°C at the start of exhaust**, i.e. upon entering the turbine (T). See above e) and f) for comparison conditions.

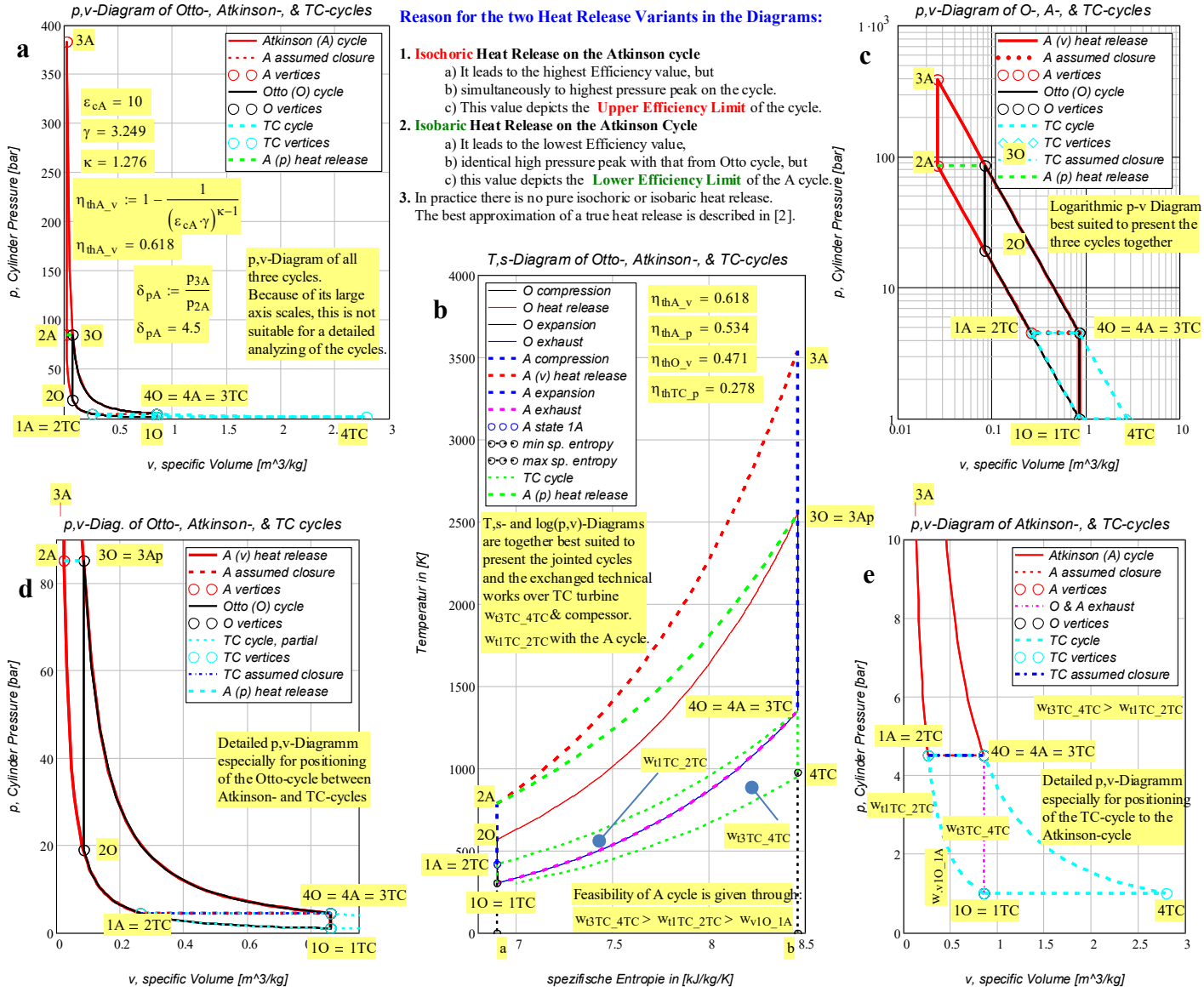

Figure A1-2. Graphic representation of the Atkinson, Otto and Gas Turbine cycles in p,v - and T,s - diagrams.

The thermodynamic background for all diagrams from Figures A1-1 and A1-2 is presented in detail in the Figures A1-3-1 to A1-3-3.

The p,v-diagram **a** from Figure A1-1 shows neatly the Otto (O) cycle and the complete exhaust gas expansion within the turbine (T) of the Turbocharger (TC). The large axis scales are not convenient for a detailed illustration of these processes. Thus, an appropriate illustration, using logarithmic axes, is featured in diagram **b** of Figure A1-1.

The Gas Turbine cycle is presented in detail in diagram **c** of Figure A1-1 and is introduced here as the basis for describing the processes taking place within the TC. The isobaric heat release (2TC-3TC) as combustion simulation in the Gas Turbine cycle is only assumed for TC, i.e. for a formal completion of the cycle. The trapped area under (4O=3TC, 4TC) to **p**-axis is proportional (~) to the specific technical Work w_{t3TC_4TC} carried out by the Turbine (T) and the trapped area under (1O=1TC, 1A=2TC) to **p**-axis is ~ to the specific technical Work w_{t1TC_2TC} consumed by the Compressor (C) for the pre-compression of the air.

The T,s-diagrams of the O and TC cycles are presented in **d** and **e** of Figure A1-1. The meaning of some of the surrounding areas in these diagrams is already described in Figure A1-1.

The pre-compressed air in the C from TC is prepared for suction into the cylinders where the Atkinson (A) cycles run. Consequently, the pre-compression (i.e. the low-pressure) part of the A cycle is completed by the TC cycle, while the high-pressure part of the A cycle serves as the combustion part and, thus, as the natural way for the TC cycle to complete. This symbiosis of the two cycles is presented in detail below in the diagrams from Figure A1-2.

All three cycles, i.e. Otto (O), Atkinson (A) and Turbocharger (TC) are presented together in the diagrams of Figure A1-2. In the p,v-diagram **a** from Figure A1-2, the 2nd Comparison Variant of the A cycle depicted there is difficult to recognize because of the large scale. The 1st and 2nd Comparison Variants are presented properly in the logarithmically scaled p,v-diagram **c** and in the detailed p,v-diagram **d**, namely the 1st is labeled as "A (v) heat release" and the 2nd one as "A (p) heat release". Both Comparison Variants are already introduced above Figure A1-2 and, for these reasons, not described again here. They determine the upper and the lower IFCE limits for the Atkinson cycle. The detailed p,v-diagrams **d** and **e** of the A and TC cycles show perfectly the symbiosis of the two cycles. The isobaric state change (1A=2TC, 4O=4A=3TC) as well as the isochoric one (4O=4A=3TC, 1O=1TC) do not exist, but are depicted solely as interfaces between the two cycles.

Diagram **e** of Figure A1-2 helps visualize and understand the size of the works exchanged between T, C, and piston during the gas exchange processes. As mentioned above: The trapped area under (4O=4A=3TC, 4TC) to **p**-axis is proportional (~) to the specific technical work w_{t3TC_4TC} carried out by the Turbine (T), while the trapped area under (1O=1TC, 1A=2TC) to **p**-axis is ~ to the specific technical work w_{t1TC_2TC} consumed by the Compressor (C) for pre-compressing the air. In addition, the trapped area under (1O=1TC, 1A=2TC) to **v**-axis is ~ to the specific volume change work w_{v1O_1A}, that the piston would have to make, in the absence of the TC, to compress the air from the environment to the pre-compression state 1A.

The T work w_{t3TC_4TC} is clearly approximately three times higher than the C work w_{t1TC_2TC} while the latter is ca. 25% higher than the required piston work w_{v1O_1A}. The numerical values from the top of Figure A1-3-3 confirm these visual estimates. The explanation for the last assignment is as follows: the work required to compress a gas in any gas flow machine between two given pressures is (κ-1)*100 % higher than the work required to do that in a closed cylinder with a piston.

The T,s-diagram **b** of Figure A1-2 is best suited to represent the O and TC cycles together with both Comparison Variants of the A cycle. Explanation of some of the surrounding areas:

- Area (a-2A-3A-b-a) is ~ with the (v) sp. heat release on the A cycle in the 1st Comparison Variant.
- Area (a-2A-3Ap-b-a) is ~ with the (p) sp. heat release on the A cycle in the 2nd Comparison Variant.
- Area (a-2O-3O-b-a) is ~ with the (v) sp. heat release on the O cycle.
- Area (b-4O-1O-a-b) is ~ with the (v) sp. heat discharged on both A and O cycles.
- Area (1TC-2TC-3TC-1TC) is ~ with the sp. technical work w_{t1TC_2TC} consumed by the Compressor (C) for pre-compressing the air
- Area (3TC-1TC-4TC-3TC) is ~ with the sp. technical work w_{t3TC_4TC} carried out by the Turbine (T).
- The areas enclosed within the cycles are ~ with the sp. work performed on the cycles. The numerical values from the top of Figure A1-3-3 confirm and support the visual estimates.

Conclusion

Depending on the estimated heat release type in the Atkinson cycle, the improvement of IFCE between the Atkinson and Otto cycles, are as follows:

Isochoric heat release in A cycle

$$\frac{\eta_{thA\_v} - \eta_{thO\_v}}{\eta_{thO\_v}} = 31.2\%$$

Isobaric heat release in A cycle

$$\frac{\eta_{thA\_p} - \eta_{thO\_v}}{\eta_{thO\_v}} = 13.5\%$$

The IFCE comparison between the Atkinson cycle and the Gas Turbine (TC) cycle is very much stronger:

$$\frac{\eta_{thA\_v} - \eta_{thTC\_p}}{\eta_{thTC\_p}} = 122.3\%$$

$$\frac{\eta_{thA\_p} - \eta_{thTC\_p}}{\eta_{thTC\_p}} = 92.2\%$$

Even the IFCE comparison between the Otto cycle and the Gas Turbine (TC) cycle is very unfavorable for the TC cycle:

$$\frac{\eta_{thO\_v} - \eta_{thTC\_p}}{\eta_{thTC\_p}} = 69.4\%$$

All these IFCE (efficiency) comparisons show that the Gas Turbine cycle of aircraft engines, such as turboprop and turbofan, have to be rigorously reconsidered.

Using a VCSR engine, as the CORE instead of the burn chamber of the turbofan or turboprop aero engines will enables the following:
a) A huge increase in efficiency, thus drastically reducing the specific fuel consumption,
b) A much greater bypass flow, e.g. well over 20%,
c) A simpler compensation of the altitude flight by the variable VCR,
d) The use of various fuels, such as gaseous or liquefied Hydrogen, biofuels, CNG, LPG or even Kerosene, either pure or in any mixture.

Thermodynamic properties of the air, reference state and other common values

Environment state (Index 0)

$T_0 := 273.15 \cdot K$ Temperature

$p_0 := 1 \cdot bar$ Pressure

$s_0 := 6.7763 \cdot \frac{kJ}{kg \cdot K}$ air specific entropy

$\kappa := 1.2765$ Isentropic Exponent averaged per engine cycles, a more realistical value than 1.4 of air in environment state

$R := 287.2 \cdot \frac{J}{kg \cdot K}$ Gas Constant of Air (as Ideal Gas)

Further conventions:
All three cycles are ideal, i.e.:
$dj = 0$ thus reversible, and
$d\left(\frac{c^2}{2}\right) = 0$ the variation of specific kinetic energy is neglected here

Foot Indices:
p = isobaric
v = isochoric
c = compression
e = expansion
t = technical
Head Index:
° = Ideal Gas

Some usefull thermodynamical formulas:

Specific Heat Capacities

$c°_v = \frac{R}{\kappa - 1}$ $c°_p = c°_v + R$ $c°_p = \frac{\kappa \cdot R}{\kappa - 1}$ $\frac{c°_p}{c°_v} = \kappa$

$c°_v := \frac{R}{\kappa - 1}$ $c°_v = 1.039 \frac{kJ}{kg \cdot K}$ $c°_p := \frac{\kappa \cdot R}{\kappa - 1}$ $c°_p = 1.326 \frac{kJ}{kg \cdot K}$

Specific Entropy Equations

$s(T,p) = s_0 + c°_p \cdot \ln\left(\frac{T}{T_0}\right) - R \cdot \ln\left(\frac{p}{p_0}\right)$ $s(T,v) = \left(s_0 + c°_v \cdot \ln\left(\frac{T}{T_0}\right)\right) + R \cdot \ln\left(\frac{v}{v_0}\right)$

State Equation (**SE**)
$p \cdot v = R \cdot T$ or
$p \cdot V = m \cdot R \cdot T$

Calorical Equations (**CE**)
$du = c°_v \cdot dT$
$dh = c°_p \cdot dT$

Specific Enthalpy definition, and its differential
$h = u + p \cdot v$
$dh = du + p \cdot dv + v \cdot dp$
$dh = du - dw_v + dy$
$dw_t = dy + dj + d\left(\frac{c^2}{2}\right)$
$dw_t = dy$ in agreement with the left conventions

1.LoT Energy balance differential & integral, First law of thermodynamic
$du = dq + dw_v + dj$ $u_2 - u_1 = q_{12} + w_{v12} + j_{12}$

2.LoT Entropy balance differential, Second law of thermodynamic
$ds = \frac{dq + dj}{T} = \frac{du - dw_v}{T} = \frac{dh - dy}{T}$

True Atkinson Cycle (Index A)

$\varepsilon_{cA} = \varepsilon_{cO}$ identical VCR volumetric compression ratios in Atkinson & Otto cycles

$\varepsilon_{cA} = \frac{v_{1A}}{v_{2A}}$ VCR of Atkinson cycle

$\varepsilon_{eA} = \frac{v_{4A}}{v_{2A}} = \frac{v_{4O}}{v_{2A}}$ Volumetric Expansion Ratio VER of Aktinson cycle, i.e.

$\gamma = \frac{\varepsilon_{eA}}{\varepsilon_{cA}} = \frac{v_{4A}}{v_{2A}} \cdot \frac{v_{2A}}{v_{1A}} = \frac{v_{4A}}{v_{1A}}$ VER to VCR ratio also expansion to compression strokes ratio of Atkinson cycle

$\gamma = \frac{v_{4O}}{v_{1A}} = \frac{\varepsilon_{cO} \cdot v_{2O}}{\varepsilon_{cA} \cdot v_{2A}} = \frac{v_{1O}}{v_{1A}} = \frac{v_{2O}}{v_{2A}}$ other derived dependencies

$\varepsilon_{eA} = \varepsilon_{cA} \cdot \gamma$ $v_{1A} = \frac{v_{4A}}{\gamma} = \frac{v_{4O}}{\gamma} = \frac{v_{2O} \cdot \varepsilon_{cO}}{\gamma} = \frac{v_{1O}}{\gamma}$

Otto Cycle (Index O)

$\varepsilon_{cA} = \varepsilon_{cO}$

$\varepsilon_{cO} = \frac{v_{1O}}{v_{2O}} = \frac{v_{4O}}{v_{2O}}$ VCR of Otto cycle

$v_{4O} = v_{4A}$ identical cylinder displacemal in both Otto- and Atkinson-cycles

identical states 1 in both Otto and Brayton cycles, thus:

$p_{1O} = p_{1TC}$ $T_{1O} = T_{1TC}$ $v_{1O} = v_{1TC}$

Because state 1A lies on the isentropic state changing 1O-2O, it follows
$m_{1A} = m_{1O} = m_{1TC}$ the proof is presented below to states 1A, 1O, 1TC

Brayton Cycle (Index TC) for Turbocharger (TC) states

Brayton cycle has a different VCR!!!!

$\varepsilon_{cTC} = \frac{v_{1TC}}{v_{2TC}} = \frac{v_{4TC}}{v_{3TC}}$ and with:
$v_{2TC} = v_{1A}$
$v_{1TC} = v_{1O}$

$\varepsilon_{cTC} = \frac{v_{1O}}{v_{1A}} = \gamma$

TrueAtkinson Cycle (Index A)

Otto Cycle (Index O)

Brayton Cycle (Index TC) for Turbocharger (TC) cycle part

Description of the state changes on all three cycles, referred to 1O as reference state

1A-2A	isentropic Compression:	$s_{1A} = s_{2A}$,
2A-3A	isochoric Heat Release:	$v_{2A} = v_{3A}$ Combust. simulation
3A-4A	isentropic Expansion,	$s_{3A} = s_{4A}$
4A-1A	Atkinson-cycle is closed over the Turbocharger (TC) cycle i.e. the Atkinson cycle substitues here the heat release on the Brayton TC cycle.	

1O-2O	isentropic Compression:	$s_{1O} = s_{2O}$
2O-3O	isochoric Heat Release:	$v_{2O} = v_{3O}$
3O-4O	isentropic Expansion:	$s_{3O} = s_{4O}$
4O-1O	isochoric Exhaust to entvir.	$v_{4O} = v_{1O}$

1TC-2TC	isentropic Compression:	$s_{1TC} = s_{2TC}$
2TC-3TC	**assumed** isobaric Heat Release:	$p_{2TC} = p_{3TC}$
3TC-4TC	isentropic Expansion:	$s_{3TC} = s_{4TC}$
4TC-1TC	isobaric Exhaust to entvir.	$p_{4TC} = p_{1TC}$

State 1A in Atkinson-cycle $p_{1A}, T_{1A}, v_{1A}, V_{1A}, m_{1A}, s_{1A}$

State 1O in Otto-cycle, all states are given: $p_{1O}, T_{1O}, v_{1O}, V_{1O}, m_{1O}, s_{1O}$

$p_{1O} \cdot V_{1O}^{\kappa} = p_{1A} \cdot V_{1A}^{\kappa}$

State 1TC in TC-cycle $p_{1TC}, T_{1TC}, v_{1TC}, m_{1TC}, s_{1TC}$

$p_{1O} = p_{1TC}$ $T_{1O} = T_{1TC}$ $v_{1O} = v_{1TC}$

The gas mass is in all cycles equal. Proof:

1O-1A-2O-2A isentropic compression

it applies: $p_{1A} = p_{1O} \cdot \left(\frac{V_{1O}}{V_{1A}}\right)^{\kappa}$ $T_{1A} = T_{1O} \cdot \left(\frac{V_{1O}}{V_{1A}}\right)^{\kappa - 1}$

with $\gamma = \frac{V_{1O}}{V_{1A}}$ it results $p_{1A} = p_{1O} \cdot \gamma^{\kappa}$ $T_{1A} = T_{1O} \cdot \gamma^{\kappa - 1}$

$m_{1A} = \frac{p_{1A} \cdot V_{1A}}{R \cdot T_{1A}} = \frac{p_{1O} \cdot \gamma^{\kappa} \cdot \frac{V_{1O}}{\gamma}}{R \cdot T_{1O} \cdot \gamma^{\kappa - 1}} = \frac{p_{1O} \cdot V_{1O}}{R \cdot T_{1O}} = m_{1O}$

from state equation **SE** in the states 1A and 1O it results identical gas mass:

$m_{1O} = \frac{p_{1O} \cdot V_{1O}}{R \cdot T_{1O}}$ and because the state 1O and 1TC are identical, it results:

$m_{1TC} = m_{1O} = m_{1A}$

1.LoT on 1O-1A $u_{1A} - u_{1O} = w_{v1O\_1A} + q_{1O\_1A}$

where $q_{1O\_1A} = 0$ isentropic => adiabatical

CE $u_{1A} - u_{1O} = c°_v \left(T_{1A} - T_{1O}\right)$ $u_{1O} = c°_v \cdot T_{1O}$

specific volume change work $w_{v1O\_1A} = c°_v \cdot \left(T_{1A} - T_{1O}\right)$

related to u_{1O} $w^*_{v1O\_1A} = \gamma^{\kappa - 1} - 1$ $w^*_{v1O\_1A} = \frac{w_{v1O\_2A}}{u_{1O}}$

Figure A1-3-1. Thermodynamic background and proof of the Efficiency formulas. Part 1.

State 2A, Isentropic Compression (1A-2A), 1A & 2A lie on (1O-2O)

$p_{2A} = p_{1A}\cdot\varepsilon_{cA}^{\kappa} = p_{1O}\cdot(\varepsilon_{cA}\cdot\gamma)^{\kappa}$ $v_{2A} = \frac{v_{1A}}{\varepsilon_{cA}} = \frac{v_{1A}}{\varepsilon_{cA}}$

$T_{2A} = T_{1A}\cdot\varepsilon_{cA}^{\kappa-1} = T_{1O}\cdot(\varepsilon_{cA}\cdot\gamma)^{\kappa-1} = T_{1O}\cdot\varepsilon_{cA}^{\kappa-1}$

$s_{2A} = s_{1A} = s_{1O}$

1.LoT on 1A-2A $u_{2A} - u_{1A} = w_{v1A\_2A} + q_{1A\_2A}$

where $q_{1A\_2A} = 0$ isentropic => adiabatical

CE $u_{2A} - u_{1A} = c°_v\cdot(T_{2A} - T_{1A})$

specific volume change work $w_{v1A\_2A} = c°_v\cdot(T_{2A} - T_{1A})$

related to u_{1O} $w^*_{v1A\_2A} = \gamma^{\kappa-1}\cdot(\varepsilon_{cA}^{\kappa-1} - 1)$

State 3A, Isochoric Heat Release (2A-3A)

The pressure Increase δ_{pA_v} due to isochoric combustion is identical in both A & O cycles

$\delta_{pA\_v} = \frac{p_{3A}}{p_{2A}} = \frac{T_{3A}}{T_{2A}}$ it folows with respect of: $\delta_{pA\_v} = \delta_{pO\_v}$ $\delta_{pTC\_p} = 1$

$\varepsilon_{cA} = \varepsilon_{cO}$ $\varepsilon_{cTC} = \gamma$

$v_{3A} = v_{2A}$ $p_{3A} = p_{2A}\cdot\delta_{pA\_v}$

$p_{2A}\cdot v_{2A} = R\cdot T_{2A}$ $p_{3A}\cdot v_{3A} = R\cdot T_{3A}$

$T_{3A} = T_{2A}\cdot\delta_{pA\_v} = T_{1O}\cdot(\varepsilon_{cA}\cdot\gamma)^{\kappa-1}\cdot\delta_{pA\_v}$

1.LoT on 2A-3A $u_{3A} - u_{2A} = w_{v2A\_3A} + q_{2A\_3A}$

where $w_{v2A\_3A} = 0$ isochoric, no volume variation

CE $u_{3A} - u_{2A} = c°_v(T_{3A} - T_{2A})$

specific released heat $q_{2A\_3A} = c°_v\cdot(T_{3A} - T_{2A})$

$q_{2A\_3A} = c°_v\cdot T_{1A}\cdot\varepsilon_{cA}^{\kappa-1}\cdot(\delta_{pA\_v} - 1)$

related to u_{1O} $q^*_{2A\_3A} = (\varepsilon_{cA}\cdot\gamma)^{\kappa-1}\cdot(\delta_{pA\_v} - 1)$

$s_{3A} = s_0 + c°_p\cdot\ln\left(\frac{T_{3A}}{T_0}\right) - R\cdot\ln\left(\frac{p_{3A}}{p_0}\right)$

State 4A, Isentropic Expansion (3A-4A), 4A lies on (3O-4O)

$p_{4A} = \frac{p_{3A}}{\varepsilon_{cA}^{\kappa}} = \frac{p_{3A}}{(\varepsilon_{cA}\cdot\gamma)^{\kappa}}$ $v_{4A} = v_{3A}\cdot\varepsilon_{cA} = v_{1A}\cdot\gamma$

$T_{4A} = \frac{T_{3A}}{\varepsilon_{cA}^{\kappa-1}} = \frac{T_{2A}\cdot\delta_{pA}}{(\varepsilon_{cA}\cdot\gamma)^{\kappa-1}} = T_{1O}\cdot\delta_{pA\_v}$ $s_{4A} = s_{3A} = s_{3O}$

1.LoT on 3A-4A $u_{4A} - u_{3A} = w_{v3A\_4A} + q_{3A\_4A}$

where $q_{3A\_4A} = 0$ isentropic => adiabatical

CE isochoric $u_{4A} - u_{3A} = c°_v(T_{4A} - T_{3A})$

specific volume change work $w_{v3A\_4A} = c°_v\cdot(T_{4A} - T_{3A})$

related to u_{1O} $w^*_{v3A\_4A} = \delta_{pA\_v}\cdot\left[1 - (\varepsilon_{cA}\cdot\gamma)^{\kappa-1}\right]$

State 1A, Complete Atkinson cycle: Isentropic expantion in TC Turbine (4A-4TC), Isobaric Exhaust and Heat Discharge over TC Turbine (4TC-1TC), Isentropic compression (1TC-2TC) in TC Compressor and Filling the cylinders (2TC-1A)

1.LoT on 4A-1O $u_{1O} - u_{4A} = w_{v4A\_1O} + q_{4A\_1O}$

where $w_{v4A\_1O} = 0$ no piston work needed for that state change

CE isochoric $u_{1O} - u_{4A} = c°_v(T_{1O} - T_{4A})$ thus

specific isochoric discharged heat $q_{4A\_1O} = c°_v(T_{1O} - T_{4A})$

related to u_{1O} $q^*_{4A\_1O} := (1 - \delta_{pA\_v})$

State 2O, Isentropic Compression (1O-2O)

$p_{2O} = p_{1O}\cdot\varepsilon_{cO}^{\kappa} = p_{1O}\cdot\left(\frac{v_{1O}}{v_{2O}}\right)^{\kappa}$ $v_{2O} = \frac{v_{1O}}{\varepsilon_{cO}}$

$T_{2O} = T_{1O}\cdot\varepsilon_{cO}^{\kappa-1}$ $s_{2O} = s_{1O}$

1.LoT on 1O-2O $u_{2O} - u_{1O} = w_{v1O\_2O} + q_{1O\_2O}$

where $q_{1O\_2O} = 0$ isentropic => adiabatical

CE $u_{2O} - u_{1O} = c°_v(T_{2O} - T_{1O})$

specific volume change work $w_{v1O\_2O} = c°_v\cdot(T_{2O} - T_{1O})$

related to u_{1O} $w^*_{v1O\_2O} = \varepsilon_{cO}^{\kappa-1} - 1$

State 3O, Isochoric Heat Release (2O-3O)

The pressure Increase δ_{pO_v} due to isochoric combustion

$\delta_{pO\_v} = \frac{p_{3O}}{p_{2O}} = \frac{T_{3O}}{T_{2O}}$ $\delta_{pA\_v} = \delta_{pO\_v}$ $\delta_{pTC\_p} = 1$

$\varepsilon_{cA} = \varepsilon_{cO}$ $\varepsilon_{cTC} = \gamma$

$v_{3O} = v_{2O}$ $p_{3O} = p_{2O}\cdot\delta_{pO\_v}$

$p_{2O}\cdot v_{2O} = R\cdot T_{2O}$ $p_{3O}\cdot v_{3O} = R\cdot T_{3O}$

$T_{3O} = T_{2O}\cdot\delta_{pO} = T_{1O}\cdot\varepsilon_{cO}^{\kappa-1}\cdot\delta_{pO\_v}$

1.LoT on 2O-3O $u_{3O} - u_{2O} = w_{v2O\_3O} + q_{2O\_3O}$

where $w_{v2O\_3O} = 0$ isochoric

CE $u_{3O} - u_{2O} = c°_v(T_{3O} - T_{2O})$

specific released heat $q_{2O\_3O} = c°_v\cdot(T_{3O} - T_{2O})$

$q_{2O\_3O} = c°_v\cdot T_{1O}\cdot\varepsilon_{cO}^{\kappa-1}\cdot(\delta_{pO\_v} - 1)$

related to u_{1O} $q^*_{2O\_3O} = \varepsilon_{cO}^{\kappa-1}\cdot(\delta_{pO\_v} - 1)$

$s_{3O} = s_0 + c°_p\cdot\ln\left(\frac{T_{3O}}{T_0}\right) - R\cdot\ln\left(\frac{p_{3O}}{p_0}\right)$

State 4O, Isentropic Expansion (3O-4O)

$p_{4O} = \frac{p_{3O}}{\varepsilon_{cO}^{\kappa}} = p_{3O}\cdot\left(\frac{v_{3O}}{v_{4O}}\right)^{\kappa}$ $v_{4O} = v_{1O}$

$\varepsilon = \varepsilon_{eO}$

$T_{4O} = \frac{T_{3O}}{\varepsilon_{cO}^{\kappa-1}} = T_{1O}\cdot\delta_{pO\_v}$ $s_{4O} = s_{3O}$

1.LoT on 4O-3O $u_{4O} - u_{3O} = w_{v4O\_3O} + q_{4O\_3O}$

where $q_{4O\_3O} = 0$ isentropic => adiabatical

CE isochoric $u_{4O} - u_{3O} = c°_v(T_{4O} - T_{3O})$

specific volume charge work $w_{v4O\_3O} = c°_v\cdot(T_{4O} - T_{3O})$

related to u_{1O} $w^*_{v3O\_4O} = \delta_{pO\_v}\cdot(1 - \varepsilon^{\kappa-1})$

State 1O, Complete Otto cycle: Isochoric Heat Discharge (4O-1O) and Exhaust to ambient

The pressure Increase δ_{pO_v} due to Combustion 2O-3O is the same for pressure decrease on Exhaust 4O-1O

$\delta_{pO\_v} = \frac{p_{4O}}{p_{1O}} = \frac{p_{3O}}{p_{1O}\cdot\varepsilon_{cO}^{\kappa}} = \frac{p_{3O}}{p_{2O}}$ $\delta_{pO\_v} = \frac{T_{4O}}{T_{1O}}$

where $T_{1O} = \frac{T_{2O}}{\varepsilon_{cO}^{\kappa-1}}$ $T_{4O} = \frac{T_{2O}\cdot\delta_{pO\_v}}{\varepsilon_{cO}^{\kappa-1}}$

specific isochoric discharged heat $q_{4O\_1O} = c°_v(T_{1O} - T_{4O})$

related to u_{1O} $q^*_{4O\_1O} := (1 - \delta_{pO\_v})$

State 2TC, Isentropic flow Compression (1TC-2TC) in TC compressor (C), identical with (1O-2A)

$p_{2TC} = p_{1TC}\cdot\varepsilon_{cTC}^{\kappa} = p_{1TC}\cdot\left(\frac{v_{1TC}}{v_{2TC}}\right)^{\kappa}$ $v_{2TC} = \frac{v_{1TC}}{\varepsilon_{cTC}}$

$T_{2TC} = T_{1TC}\cdot\varepsilon_{cTC}^{\kappa-1}$ $s_{2TC} = s_{1TC}$

1.LoT on 1O-2A $h_{2TC} - h_{1TC} = w_{t1TC\_2TC} + q_{1TC\_2TC}$

where $q_{1TC\_2TC} = 0$ isentropic = adiabatical

CE $h_{2TC} - h_{1TC} = c°_p(T_{2TC} - T_{1TC})$

specific technical work of C $w_{t1TC\_2TC} = c°_p\cdot(T_{2TC} - T_{1TC})$

related to u_{1O} $w^*_{t1TC\_2TC} = \kappa\cdot(\varepsilon_{cTC}^{\kappa-1} - 1)$

State 3TC, Isobaric Heat Release (2TC-3TC)

No pressure increase δ_{pTC_p} due to the assumed isobaric combustion

$p_{3TC} = p_{2TC}$ isobaric $\delta_{pTC\_p} = 1$

For a suitable comparison of the efficiencies of the Otto & Atkinson Cycles, it is necessary to respect some conditions: All three cycles are designed so that the temperature on entering the turbine (T) i.e. at the Exhaust beginning reaches about 1000°C. See e) comparison condition.

$T_{3TC} = T_{4O} = T_{4A}$ $\delta_{pTC} = \delta_{pA\_v} = \delta_{pO\_v}$

The states 3TC, 4O & 4A are identical $\varepsilon_{cTC} = \gamma$

1.LoT on 2TC-3TC $h_{3TC} - h_{2TC} = w_{t2TC\_3TC} + q_{2TC\_3TC}$

where $w_{t2TC\_3TC} = 0$ isobaric

CE $h_{3TC} - h_{2TC} = c°_p(T_{3TC} - T_{2TC})$

specific released heat $q_{2TC\_3TC} = c°_p\cdot(T_{3TC} - T_{2TC})$

$q_{2TC\_3TC} = c°_p\cdot(T_{3TC} - T_{1TC}\cdot\varepsilon_{cTC}^{\kappa-1})$

related to u_{1O} $q^*_{2TC\_3TC} = \kappa\cdot(\delta_{pTC} - \varepsilon_{cTC}^{\kappa-1})$

$s_{3TC} = s_0 + c°_p\cdot\ln\left(\frac{T_{3TC}}{T_0}\right) - R\cdot\ln\left(\frac{p_{3TC}}{p_0}\right)$

State 4TC, Isentropic flow Expansion (3TC-4TC) in T

$p_{4TC} = \frac{p_{3TC}}{\varepsilon_{cTC}^{\kappa}} = p_{1TC} = p_{1O} = p_0$ $v_{4TC} = \frac{v_{3TC}}{\varepsilon_{cTC}}$

$T_{4TC} = \frac{T_{3TC}}{\varepsilon_{cTC}^{\kappa-1}}$ with $\delta_{pTC} = \delta_{pA\_v} = \delta_{pO\_v}$

$s_{4TC} = s_{3TC}$

1.LoT on 1TC-2TC $h_{4TC} - h_{3TC} = w_{t3TC\_4TC} + q_{3TC\_4TC}$

where $q_{3TC\_4TC} = 0$ isentropic = adiabatical

CE isobaric $h_{4TC} - h_{3TC} = c°_p(T_{4TC} - T_{3TC})$

specific technical work of T $w_{t3TC\_4TC} = c°_p\cdot(T_{4TC} - T_{3TC})$

related to u_{1O} $w^*_{t3TC\_4TC} = \kappa\cdot\delta_{pTC}\cdot\left(\frac{1}{\varepsilon_{cTC}^{\kappa-1}} - 1\right)$

State 1TC, Complete TC cycle part: Isobaric Exhaust and Heat Discharge (4TC-1TC) over TC Turbine (T)

$p_{4TC} = p_{1TC} = p_{1O}$ isobaric

In the Brayton cycle the released heat is only assumed for an adequate comparison to the Atkinson & Otto cycles. All cycles are designed so that the temperature on entering the turbine, at the start of Exhaust, reaches about 1000°C.

$\varepsilon_{cTC} = \gamma$ $T_{3TC} = T_{4A} = T_{4O}$ $T_{1TC} = T_{1O}$

specific isobaric discharged heat $q_{4TC\_1TC} = c°_p\cdot(T_{1O} - T_{4TC})$

rel. to u_{1O} $q^*_{4TC\_1TC} = \kappa\cdot\left(1 - \frac{\delta_{pTC}}{\varepsilon_{cTC}^{\kappa-1}}\right) = \kappa\cdot\left(1 - \frac{\delta_{pTC}}{\gamma^{\kappa-1}}\right)$

Figure A1-3-2. Thermodynamic background and proof of the Efficiency formulas. Part 2.

Numerical value results for the folowing parameter: $\varepsilon_{cA} := 10$ $\gamma = 3.249$ $\delta_{pA\_v} = 4.5$ $\varepsilon_{cO} = 10$ $\delta_{pO\_v} = 4.5$ $\varepsilon_{cTC} = 3.249$ $\gamma = 3.249$ $\delta_{pTC} := \delta_{pO\_v}$

$q^*_{4A\_1O} := \left(1 - \delta_{pA\_v}\right)$ $q^*_{4A\_1O} = -3.5$

$q^*_{2A\_3A} := \left(\varepsilon_{cA}\cdot\gamma\right)^{\kappa-1}\cdot\left(\delta_{pA\_v} - 1\right)$ $q^*_{2A\_3A} = 9.164$

$w^*_{v1O\_1A} := \gamma^{\kappa-1} - 1$ $w^*_{v1O\_1A} = 0.385$

$w^*_{v1A\_2A} := \gamma^{\kappa-1}\cdot\left(\varepsilon_{cA}^{\kappa-1} - 1\right)$ $w^*_{v1A\_2A} = 1.233$

$w^*_{v3A\_4A} := \delta_{pA\_v}\cdot\left[1 - \left(\varepsilon_{cA}\cdot\gamma\right)^{\kappa-1}\right]$ $w^*_{v3A\_4A} = -7.282$

Review of the energy balance on A cycle

$q^*_{4A\_1O} + q^*_{2A\_3A} + w^*_{v1A\_2A} + w^*_{v3A\_4A} + w^*_{v1O\_1A} = 0$

IFCE, Thermodynamical efficiency of Atkinson-cycle

$w^*_{vA} = w^*_{v1A\_2A} + w^*_{v3A\_4A} + w^*_{v1O\_1A}$

$w^*_{vA} = \left(\delta_{pA} - 1\right)\cdot\left[\left(\varepsilon_{cA}\cdot\gamma\right)^{\kappa-1} - 1\right]$

1st evidence for IFCE of Atkinson cycle with isochoric heat release

$\eta_{thA\_v} = \dfrac{-w^*_{vA}}{q^*_{2A\_3A}} = \dfrac{-\left(\delta_{pA\_v} - 1\right)\cdot\left[\left(\varepsilon_{cA}\cdot\gamma\right)^{\kappa-1} - 1\right]}{\left(\varepsilon_{cA}\cdot\gamma\right)^{\kappa-1}\cdot\left(\delta_{pA\_v} - 1\right)}$

$\eta_{thA\_v} = \dfrac{-w^*_{vA}}{q^*_{2A\_3A}} = 1 - \dfrac{1}{\left(\varepsilon_{cA}\cdot\gamma\right)^{\kappa-1}}$

2nd evidence for IFCE of Atkinson cycle with isochoric heat release

$\eta_{thA\_v} = 1 - \dfrac{\left|q^*_{4A\_1O}\right|}{q^*_{2A\_3A}} = 1 - \dfrac{\delta_{pA\_v} - 1}{\left(\varepsilon_{cA}\cdot\gamma\right)^{\kappa-1}\cdot\left(\delta_{pA\_v} - 1\right)}$

$\eta_{thA\_v} := \left[1 - \dfrac{1}{\left(\varepsilon_{cA}\cdot\gamma\right)^{\kappa-1}}\right]$ $\eta_{thA\_v} = 0.618$

$q^*_{4O\_1O} := \left(1 - \delta_{pO\_v}\right)$ $q^*_{4O\_1O} = -3.5$

$q^*_{2O\_3O} := \varepsilon_{cO}^{\kappa-1}\cdot\left(\delta_{pO\_v} - 1\right)$ $q^*_{2O\_3O} = 6.616$

$w^*_{v1O\_2O} := \varepsilon_{cO}^{\kappa-1} - 1$ $w^*_{v1O\_2O} = 0.89$

$w^*_{v3O\_4O} := \delta_{pO\_v}\cdot\left(1 - \varepsilon_{cO}^{\kappa-1}\right)$ $w^*_{v3O\_4O} = -4.006$

Review of the energy balance on O cycle

$q^*_{4O\_1O} + q^*_{2O\_3O} + w^*_{v1O\_2O} + w^*_{v3O\_4O} = 0$

IFCE, Thermodynamical efficiency of Otto-cycle

$w^*_{vO} = w^*_{v1O\_2O} + w^*_{v3O\_4O}$

$w^*_{vO} = \left(\delta_{pO} - 1\right)\cdot\left(\varepsilon_{cO}^{\kappa-1} - 1\right)$

1st evidence for IFCE of Otto cycle with isochoric heat release

$\eta_{thO\_v} = \dfrac{-w^*_{vO}}{q^*_{2O\_3O}} = \dfrac{-\left(\delta_{pO\_v} - 1\right)\cdot\left(\varepsilon_{cO}^{\kappa-1} - 1\right)}{\varepsilon_{cO}^{\kappa-1}\cdot\left(\delta_{pO\_v} - 1\right)}$

$\eta_{thO\_v} = \dfrac{-w^*_{vO}}{q^*_{2O\_3O}} = 1 - \dfrac{1}{\varepsilon_{cO}^{\kappa-1}}$

2nd evidence for IFCE of Otto cycle with isochoric heat release

$\eta_{thO\_v} = 1 - \dfrac{\left|q^*_{4O\_1O}\right|}{q^*_{2O\_3O}} = 1 - \dfrac{\delta_{pO\_v} - 1}{\varepsilon_{cO}^{\kappa-1}\cdot\left(\delta_{pO\_v} - 1\right)}$

$\eta_{thO\_v} := \left(1 - \dfrac{1}{\varepsilon_{cO}^{\kappa-1}}\right)$ $\eta_{thO\_v} = 0.471$

$q^*_{4TC\_1TC} := \kappa\cdot\left(1 - \dfrac{\delta_{pTC}}{\varepsilon_{cTC}^{\kappa-1}}\right)$ $q^*_{4TC\_1TC} = -2.871$

$q^*_{2TC\_3TC} := \kappa\cdot\left(\delta_{pTC} - \varepsilon_{cTC}^{\kappa-1}\right)$ $q^*_{2TC\_3TC} = 3.976$

$w^*_{t1TC\_2TC} := \kappa\cdot\left(\varepsilon_{cTC}^{\kappa-1} - 1\right)$ $w^*_{t1TC\_2TC} = 0.492$

$w^*_{t3TC\_4TC} := \kappa\cdot\left(\dfrac{\delta_{pTC}}{\varepsilon_{cTC}^{\kappa-1}} - \delta_{pTC}\right)$ $w^*_{t3TC\_4TC} = -1.597$

Review of the energy balance on TC cycle

$q^*_{4TC\_1TC} + q^*_{2TC\_3TC} + w^*_{t1TC\_2TC} + w^*_{t3TC\_4TC} = 0$

IFCE, Thermodyn. efficiency of Brayton cycle

$w^*_{tTC} = w^*_{t1TC\_2TC} + w^*_{t3TC\_4TC}$

$w^*_{tTC} = \kappa\cdot\left(\delta_{pTC} - \varepsilon_{cTC}^{\kappa-1}\right)\cdot\left(\dfrac{1}{\varepsilon_{cTC}^{\kappa-1}} - 1\right)$

1st evidence for IFCE of Brayton cycle with isobaric heat release

$\eta_{thTC\_p} = \dfrac{-w^*_{tTC}}{q^*_{2TC\_3TC}} = 1 - \dfrac{1}{\varepsilon_{cTC}^{\kappa-1}}$

2nd evidence for IFCE of Brayton cycle with isobaric heat release

$\eta_{thTC\_p} = 1 - \dfrac{\left|q^*_{4TC\_1TC}\right|}{q^*_{2TC\_3TC}} = 1 - \dfrac{1}{\varepsilon_{cTC}^{\kappa-1}}$

$\eta_{thTC\_p} := \left(1 - \dfrac{1}{\varepsilon_{cTC}^{\kappa-1}}\right)$ $\eta_{thTC\_p} = 0.278$

State 3Ap, on the Atkinson cycle, in the 2 nd Comparison Variant, with Isobaric Heat Release (2A-3Ap), where (3Ap overlapes 3O)

No pressure Increase! $\delta_{pA\_p} = 1$ due to pure **isobaric** combustion on A cycle.

$\delta_{pA\_p} = \dfrac{p_{3Ap}}{p_{2A}} = 1$

The isobaric heat release on the A cycle, i.e. like that from an ideal Diesel cycle, leads to the lowest efficiency
The states 3Ap and 3O becomes overlapped.
This type of heat release represents the worst case scenario.

it folows:

$v_{3Ap} = v_{3O} = \dfrac{v_{1O}}{\varepsilon_{cO}}$ $p_{3Ap} = p_{2A}\cdot\delta_{pA\_p} = p_{2A} = p_{3O}$

$p_{2A}\cdot v_{2A} = R\cdot T_{2A}$ $p_{3Ap}\cdot v_{3Ap} = R\cdot T_{3Ap}$ $T_{3Ap} = T_{3O}$

$s_{3Ap} = s_0 + c^\circ_p\cdot\ln\left(\dfrac{T_{3Ap}}{T_0}\right) - R\cdot\ln\left(\dfrac{p_{3Ap}}{p_0}\right)$

$T_{3Ap} = T_{1O}\cdot\varepsilon_{cA}^{\kappa-1}\cdot\delta_{pO\_v}$ $v_{2A} = \dfrac{v_{2O}}{\gamma}$ $v_{3O} = v_{2O}$ $p_{1O}\cdot v_{1O} = R\cdot T_{1O}$ $R = c^\circ_v\cdot(\kappa - 1)$

1.LoT on 2A-3Ap $u_{3Ap} - u_{2A} = w_{v2A\_3A} + q_{2A\_3A}$

specific volume change work
isobaric ==>
related to u_{1O} $w_{v2A\_3Ap} = -p_{2A}\cdot\left(v_{3O} - v_{2A}\right) = -p_{1O}\cdot v_{1O}\cdot\left(\varepsilon_{cA}\cdot\gamma\right)^{\kappa-1}\cdot(\gamma - 1)$

$w^*_{v2A\_3Ap} = \dfrac{w_{v2A\_3Ap}}{c^\circ_v\cdot T_{1O}} = (\kappa - 1)\cdot\left(\varepsilon_{cA}\cdot\gamma\right)^{\kappa-1}\cdot(1 - \gamma)$

$w^*_{v2A\_3Ap} := (\kappa - 1)\cdot\left(\varepsilon_{cA}\cdot\gamma\right)^{\kappa-1}\cdot(1 - \gamma)$ $w^*_{v2A\_3Ap} = -1.628$

CE isobaric $h_{3Ap} - h_{2A} = c^\circ_p\left(T_{3Ap} - T_{2A}\right)$ $T_{2A} = T_{1O}\cdot\left(\varepsilon_{cA}\cdot\gamma\right)^{\kappa-1}$

specific isobaric released heat $q_{2A\_3Ap} = c^\circ_p\cdot\left(T_{3Ap} - T_{2A}\right)$

$q_{2A\_3Ap} = \kappa\cdot c^\circ_v\cdot\left[T_{1O}\cdot\varepsilon_{cA}^{\kappa-1}\cdot\delta_{pO\_v} - T_{1O}\cdot\left(\varepsilon_{cA}\cdot\gamma\right)^{\kappa-1}\right]$

related to u_{1O} $q^*_{2A\_3Ap} = \dfrac{q_{2A\_3Ap}}{c^\circ_v\cdot T_{1O}}$ after some operation it results:

isobaric ==>
related to u_{1O} $q^*_{2A\_3Ap} = \kappa\cdot\left(\varepsilon_{cA}\cdot\gamma\right)^{\kappa-1}\cdot\left(\dfrac{\delta_{pA\_v}}{\gamma^{\kappa-1}} - 1\right)$ additional p Footindex!

$q^*_{2A\_3Ap} := \kappa\cdot\left(\varepsilon_{cA}\cdot\gamma\right)^{\kappa-1}\cdot\left(\dfrac{\delta_{pA\_v}}{\gamma^{\kappa-1}} - 1\right)$ $q^*_{2A\_3Ap} = 7.515$

Only for comparison:

isochoric ==>
related to u_{1O} $q^*_{2A\_3A} = \left(\varepsilon_{cA}\cdot\gamma\right)^{\kappa-1}\cdot\left(\delta_{pA\_v} - 1\right)$ without any additional Footindex

$q^*_{2A\_3A} := \left(\varepsilon_{cA}\cdot\gamma\right)^{\kappa-1}\cdot\left(\delta_{pA\_v} - 1\right)$ $q^*_{2A\_3A} = 9.164$

1st evidence for IFCE of Atkinson cycle with isobaric heat release

$\eta_{thA\_p} = 1 - \dfrac{\left|q^*_{4A\_1O}\right|}{q^*_{2A\_3Ap}} = 1 - \dfrac{\delta_{pA\_v} - 1}{\kappa\cdot\left(\varepsilon_{cA}\cdot\gamma\right)^{\kappa-1}\cdot\left(\dfrac{\delta_{pA\_v}}{\gamma^{\kappa-1}} - 1\right)}$

The pressure Increase δ_{pA_v} due to isochoric combustion is identical in both A & O cycles

Numerical values:

$\eta_{thA\_p} := 1 - \dfrac{\delta_{pA\_v} - 1}{\kappa\cdot\left(\varepsilon_{cA}\cdot\gamma\right)^{\kappa-1}\cdot\left(\dfrac{\delta_{pA\_v}}{\gamma^{\kappa-1}} - 1\right)}$ $\eta_{thA\_p} = 0.534$ $\delta_{pA\_v} = 4.5$

2nd evidence for IFCE of Atkinson cycle with isobaric heat release

$w^*_{vAp} := \left(w^*_{v1A\_2A} + w^*_{v2A\_3Ap} + w^*_{v3O\_4O} + w^*_{v1O\_1A}\right)$ $w^*_{vAp} = -4.016$

$\eta_{thA\_p} := \dfrac{-w^*_{vAp}}{q^*_{2A\_3Ap}}$ $\eta_{thA\_p} = 0.534$

Figure A1-3-3. Thermodynamic background and proof of the Efficiency formulas. Part 3.

Appendix 2. Comparison of the real cycles:

Comparison of the thermal efficiencies for the real cycles of the true Atkinson (A) and the classic gasoline Otto (O) ICE Seiliger (S), both turbocharged & hydrogen fueled, while maintaining the same VCR values, expansion stroke lengths, maximum gas mass and AFR, λ = 1, (thus under the same conditions).

The classic Otto ICE - considered here - is **hypothetical** because it offers the variation of its volumetric compression ratio (VCR) by means of a symmetrical crank drive (e.g. like that of a CFR octane-testing engine).

The comparison was done using the AVL BOOST simulation tool. The simulation model used below is developed for a 3-cylinder engine with hydrogen-direct-injection GasDI, two stage turbocharging and air intercooling. The displacement volume of this engine is near 1 liter.

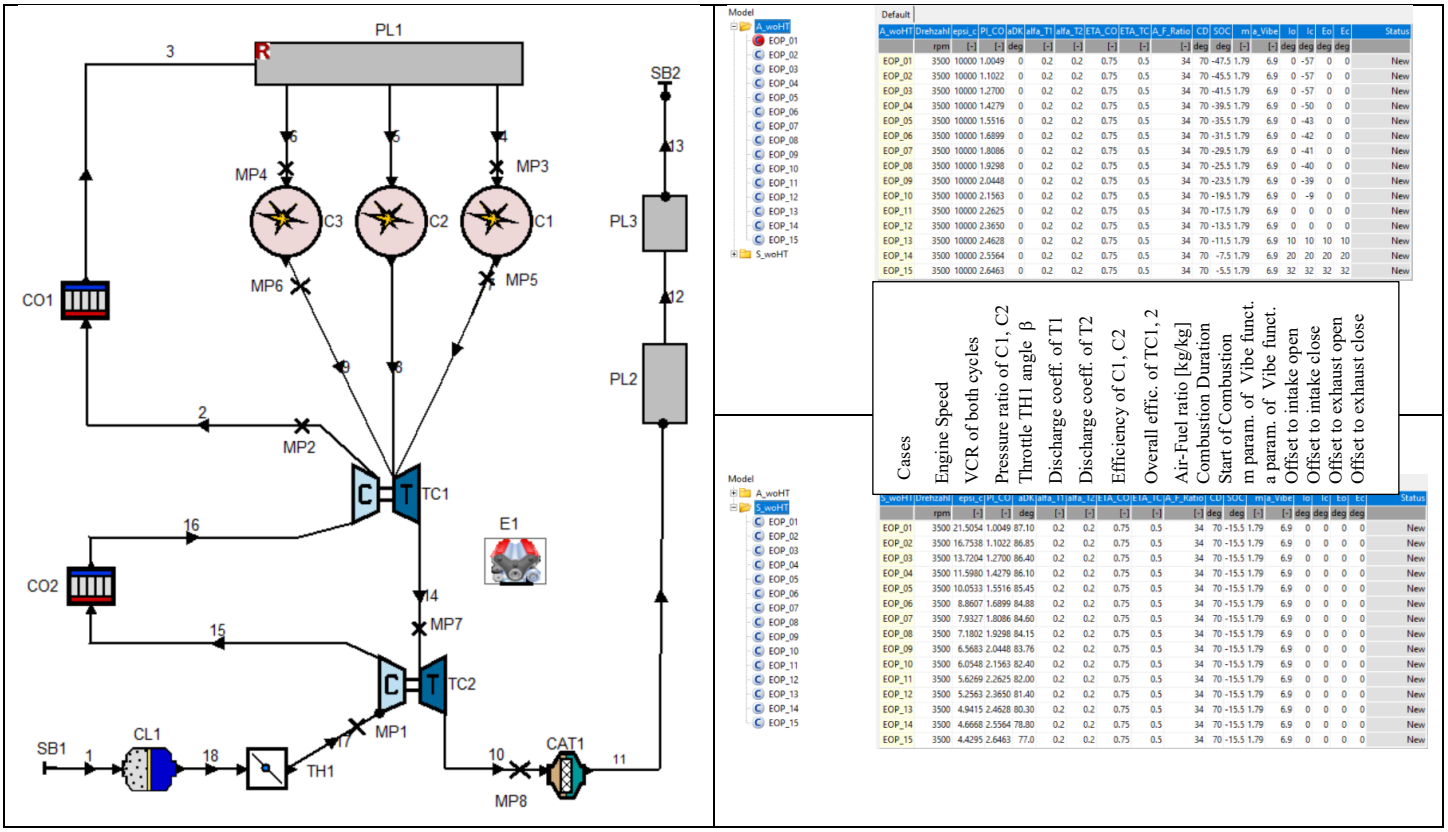

Figure A2-1. Simulation Model in AVL BOOST tool on the left. The simulated cases (top Table) of the true Atkinson (A) cycles and (bottom Table) of the classical Seiliger (S) cycles are presented on the right side.

In the top Table of the simulated cases from Fig. A2-1, the VCR values of the true Atkinson cycles are the same as those of the Seiliger cycle. The values 10000 introduced there for (A) are only formal, i.e. they are not effective. The AVL BOOST tool has the possibility to simulate cycles with a user-defined piston motion. This gives the user freedom to simulate an unconventional powertrain, like VCSR. For a user-defined piston motion, the relative piston position should be specified over crank angle. In BOOST, the relative piston position is defined as the distance of the piston from the TDC position relative to the full stroke. Zero degree crank angle corresponds to the Firing TDC of the selected cylinder.

However, the true Atkinson cycle features strokes of various length. The BOOST tool makes in the background a recalculation of the given user-defined piston motions using the set VCR value, the crank mechanism geometry, and modified the user-defined piston motion inadequately. To avoid this alteration of the user-defined piston motion, the VCR is for true Atkinson cycles formally set to 10000 or more. This huge VCR value can by the way influence the computed values for the heat transfer models in the cylinders.

For this reason, **the heat transfer in the cylinders is completely deactivated in this comparison study**, i.e. the simulation is carried out only for **adiabatic** cycles. However, the frictions FMEP in the crank mechanism are considered and set identical in both cycles, as shown in Fig. A2-2.

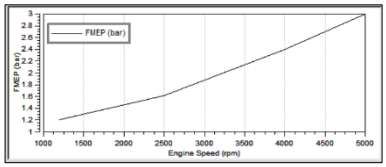

Figure A2-2. Friction values FMEP of the true Atkinson and the Seiliger cycles (on the left side) and Throttle flow coefficients (on the right side) considered in the Simulation Model in AVL BOOST®.

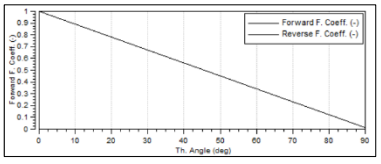

The VCSR crank mechanism is presented in Fig. 3-1 to Fig. 3-5. The eccentric crank (EC) of the VCSR mechanism for the true Atkinson cycle and the classical crankshaft for the classical Seiliger cycle have the same rotation speed n. The Crank Disks (CD) of the VCSR have only half of it.

The comparison between the true Atkinson and classical Seiliger cycles is presented in the following figures in 15 Engine Operation Points (EOP). The figures demonstrate the new kind, namely Ultra Downsizing (UD), of Load Control (LC) of the VCSR engine – working according to the true Atkinson cycles – from small load 1st EOP to large load 15th EOP. Meanwhile, the engine speed remains unchanged at 3500 rpm.

The load control, at constant speed, of classic motors takes place in the following variants:

a) The quality of the air-fuel mixture AFR of the Diesel ICE is varied for the load control. The sucked air mass with some exhaust gases from EGR remains nearly constant, but the injected fuel mass is varied for load control. The resulting AFR is always higher than one or $\lambda > 1$, i.e. the air-fuel mixture is lean. Lean air-fuel ratios favor the generation of NOx emissions and simultaneously hinder their reduction in the common 3-way catalysts.
b) The quantity of the air-fuel mixture of the Gasoline ICE is varied by means of the throttle valve (see TH1 in the BOOST model of Fig. A2-1) or intake valve throttling for the load control. The quality of the air-fuel mixture remains constant, mostly stoichiometric, i.e. AFR or $\lambda = 1$. Thus, the reduction of NOx emissions in the common 3-way catalysts is assured.

In contrast to the load controls a) and b) of the classic ICE, the UD LC of the VCSR ICE takes place in a new, special way see [**1**], [**2**] and Patents DE102013003682B4, EP 2 772 624 B1, which tries to retain the advantages of the classic types, while avoiding their disadvantages.

The Ultra Downsizing UD Load Control LC of the VCSR ICE uses the following strategy; see Figure A2-EOPs-01-15 and the Claim 8 of the EP Patent:

a) Only compressed air is sucked into the cylinders.
b) The fuel, preferably hydrogen, but also CNG or other liquid or gaseous fuels in pure or mixed form, are injected or blown in directly and sequentially in the cylinders. A dual fuel injection, with MPI in intake channels only for liquid fuels, like gasoline, methanol or other volatile fuels is also possible see [**23**].
c) The quality of the air-fuel mixture remains constant, mostly stoichiometric, i.e. AFR or $\lambda = 1$. Thus, the reduction of some possible raw NOx emissions is assured by means of the common 3-way catalysts.
d) The VCR can be varied by means of a rotational adjustment of the Ring Gear RG see [**1**] and Fig. 3-1 to Fig. 3-5.
e) High VCR values lead to low loads because the intake stroke becomes shorter and thus less air mass is sucked in. See for example the simulation results of the 1st EOP in Figure A2-EOP-01. In addition, the exhaust stroke is shorter and therefore the emptying of the cylinders remains incomplete. This affords in fact an internal exhaust gas recirculation EGR. The exhaust gases have lower temperature and mass flow values. The turbine produces low power for driving the compressor. Thus, the boost pressure remains at a lower level.
f) Low VCR values lead to high loads because the intake stroke becomes longer and thus more air mass is sucked in. See for example the simulation results of the 15th EOP in Figure A2-EOP-15. In addition, the exhaust stroke is longer and therefore the emptying of the cylinders becomes nearly complete. The exhaust gases have higher temperature and mass flow values. The turbine produces more power for driving the compressor. Thus, the boost pressure reaches a higher level.

Short description of the following Figures.

1. The top-left diagram of each EOP depicts the variations of the displacement volume (V) versus crank angle (CA).
- The VCR is defined as the quotient of the V in Gasex. BDC to V in TDC.
- The VER is defined as the quotient of the V in BDC to V in TDC.
- The Parameter γ is defined as the quotient of VER to VCR and thus of V in TDC to V in Gasex. BDC.

2. The top-right diagram each EOP depicts the variations of the cylinder pressure (p) versus V in natural logarithmic coordinates. Because of the kinematic of the VCSR crank mechanism, the angular positions of the TDC of the true Atkinson cycle migrate in relation to the TDC of the Seiliger cycle. That produces a slow translation of the curves in these diagrams, but the correspondence to the curves of Figure A1-2 from Appendix 1 remains obvious. The variation of the strokes described above under e) and f) for load control is clearly observable.
3. The middle-left diagram of each EOP depicts the variations of the cylinder gas mass (m) versus V. The maximum values on the cycles are indicated there for an easy comparison. The variation of the strokes described above under e) and f) for load control is also clearly observable.
4. The middle-right diagram of each EOP depicts the variations of the indicated fuel conversion efficiency IFCE (i.e. of the volumetric work integral divided by the released heat on the cycle) versus V. These diagrams depict the losses and gains in volumetric work along the strokes. The end values are included. The advantage of a long expansion stroke of the real Atkinson cycle is obvious.
5. The bottom-left diagram of each EOP depicts the variations of the cylinder absolute gas Temperature (T) versus absolute (S = m*s) entropy flow dS/dt. The areas within the diagrams are energy flows in Watt released into the cylinder or exchanged between the gas from the cylinder and the exterior. The lower consumed power (i.e. exergy flow) on the compression strokes and the greater released power on the expansion strokes of the real Atkinson cycles are clearly shown. The lost energy flow during exhaust is clearly depicted. This energy flow does not produce volumetric work at the piston, but it drives the TC-compressor. The usual T,s diagram from Figure A1-2 does not work adequately here because of gas mass variation during the exhaust and intake processes. The T,s diagram is adequate only for closed cycles, i.e. with constant mass, or open cycles, with constant mass flow. In the true Atkinson cycle the exergy part of the exhausted energy flow is much lower (indicated by its lower temperature) because of their consumption on the extended expansion, compared with the Seiliger cycle.
6. The bottom-right diagram of each EOP depicts the variations of the cylinder pressure p versus V and the cylinder temperature (T) versus V in the usual coordinates.
7. An example of the heat transfer influence can be won from the Figure A2-EOP-15_nonad and A2-EOPs-01-15_nonad (i.e. NONadiabatic).

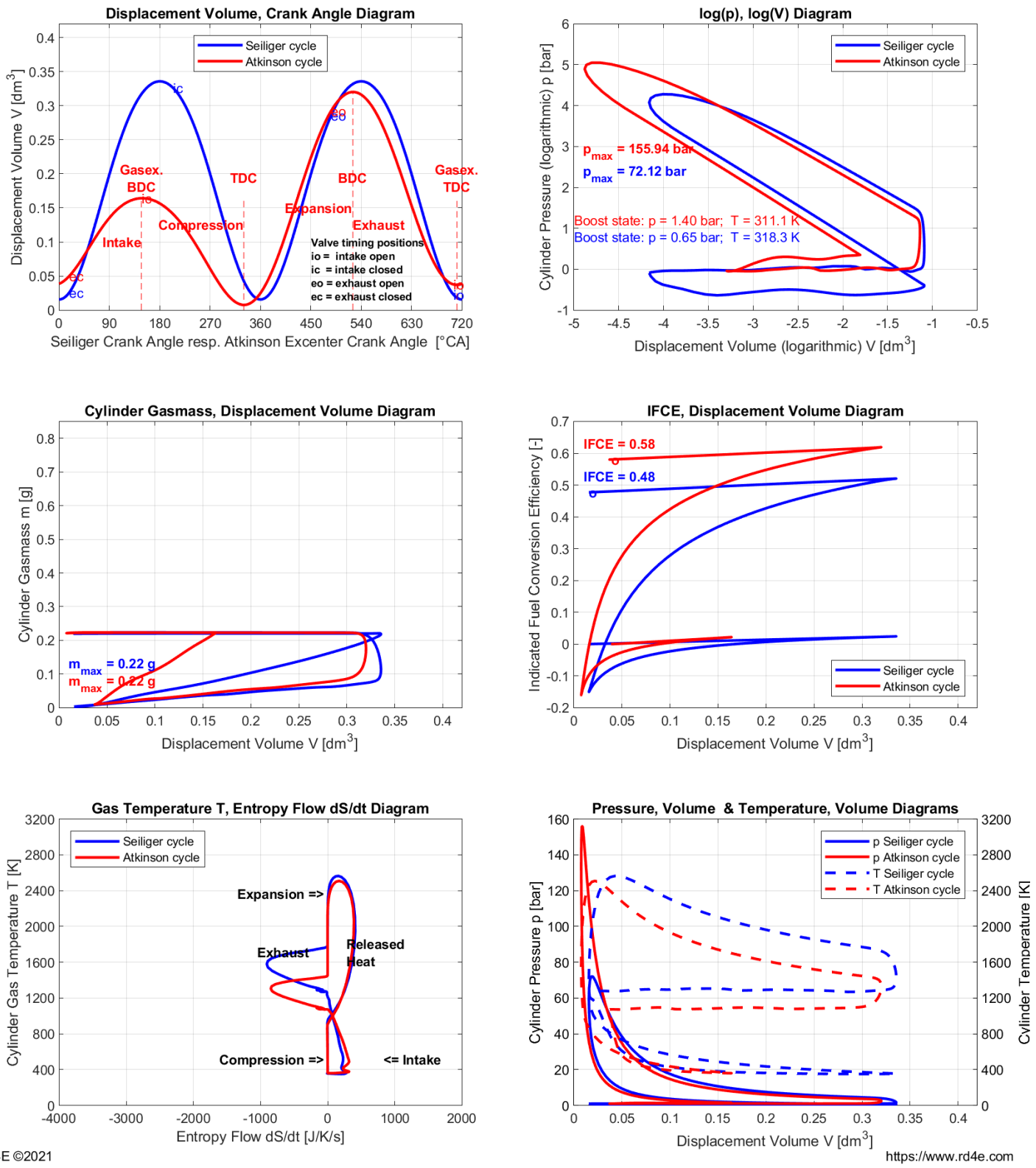

Figure A2-EOP-01. Simulation results of the true Atkinson and the Seiliger cycles by using the AVL BOOST tool. The Summary files for A & S are linked here, to examine all mean values of the simulation parameters.

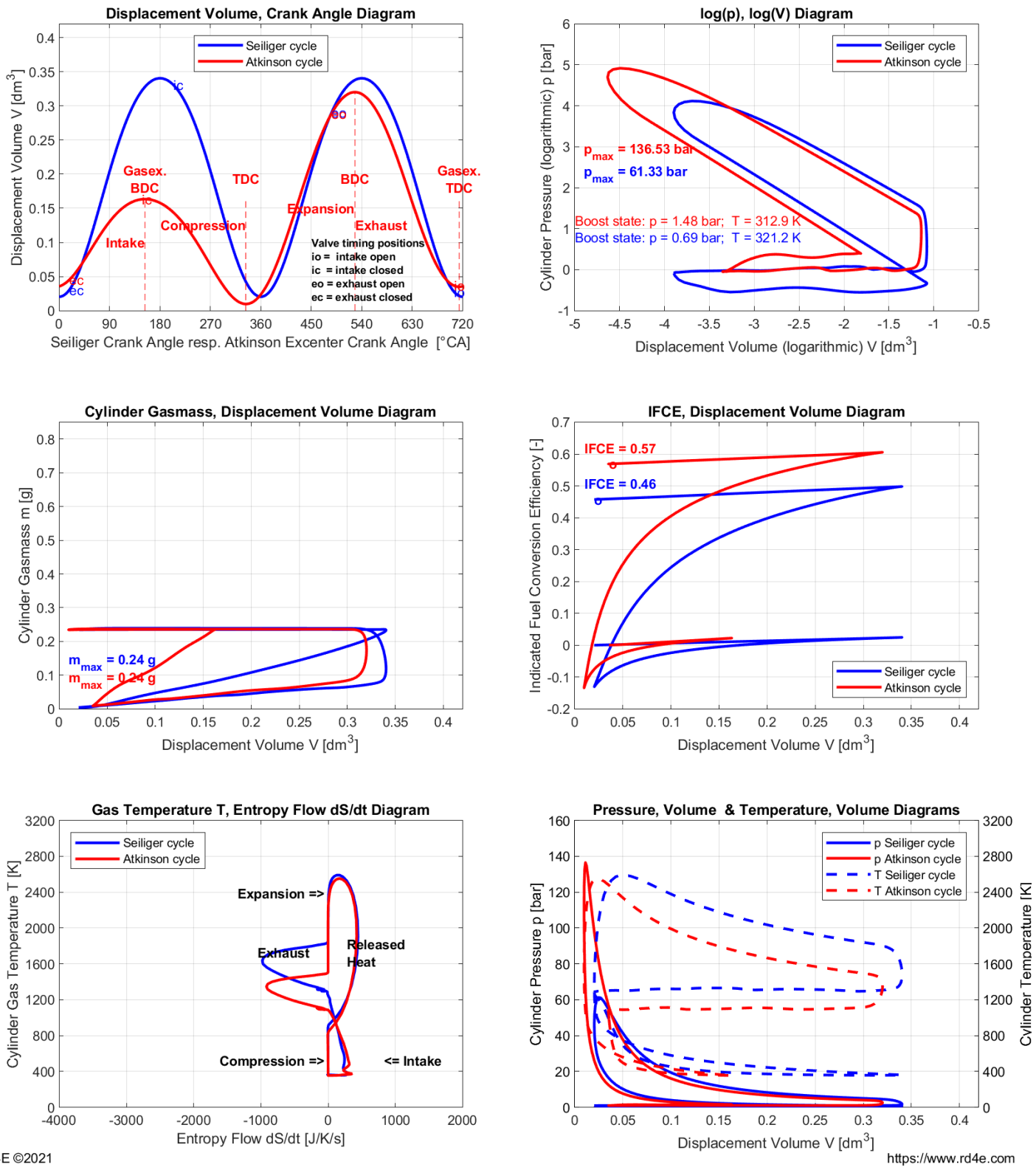

Figure A2-EOP-02. Simulation results of the true Atkinson and the Seiliger cycles by using the AVL BOOST tool. The Summary files for A & S are linked here, to examine all mean values of the simulation parameters.

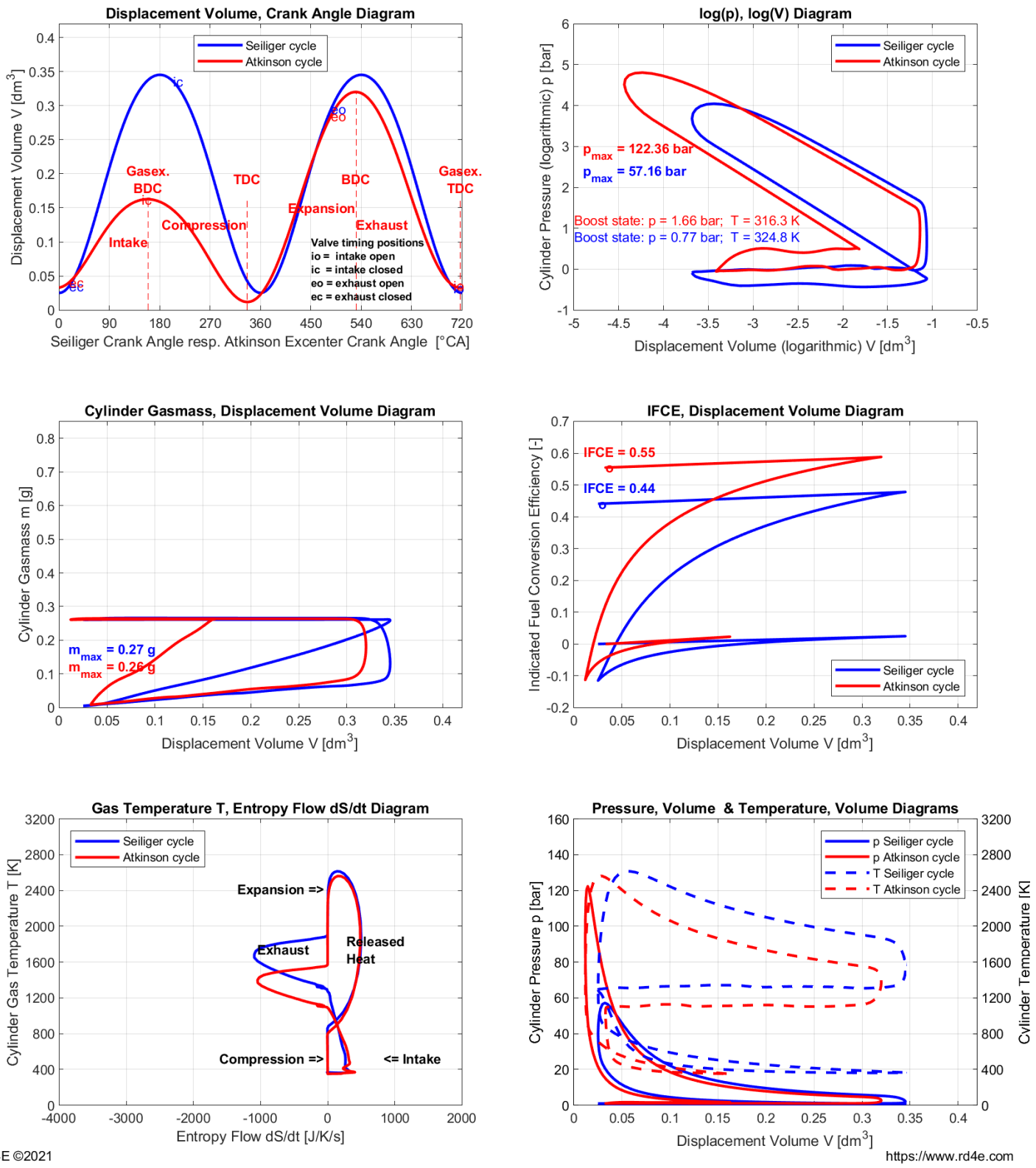

Figure A2-EOP-03. Simulation results of the true Atkinson and the Seiliger cycles by using the AVL BOOST tool. The Summary files for A & S are linked here, to examine all mean values of the simulation parameters.

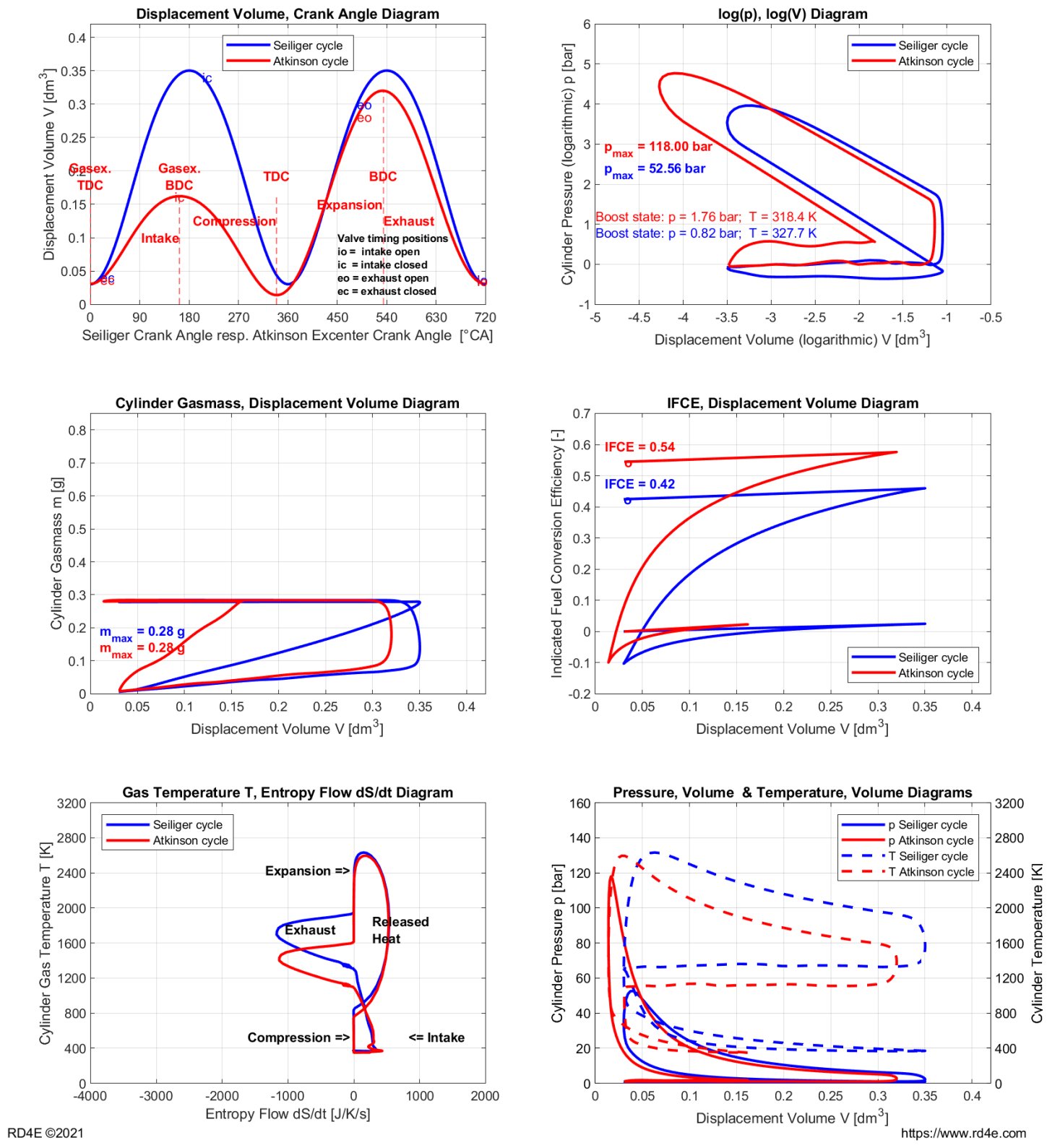

Figure A2-EOP-04. Simulation results of the true Atkinson and the Seiliger cycles by using the AVL BOOST tool. The Summary files for A & S are linked here, to examine all mean values of the simulation parameters.

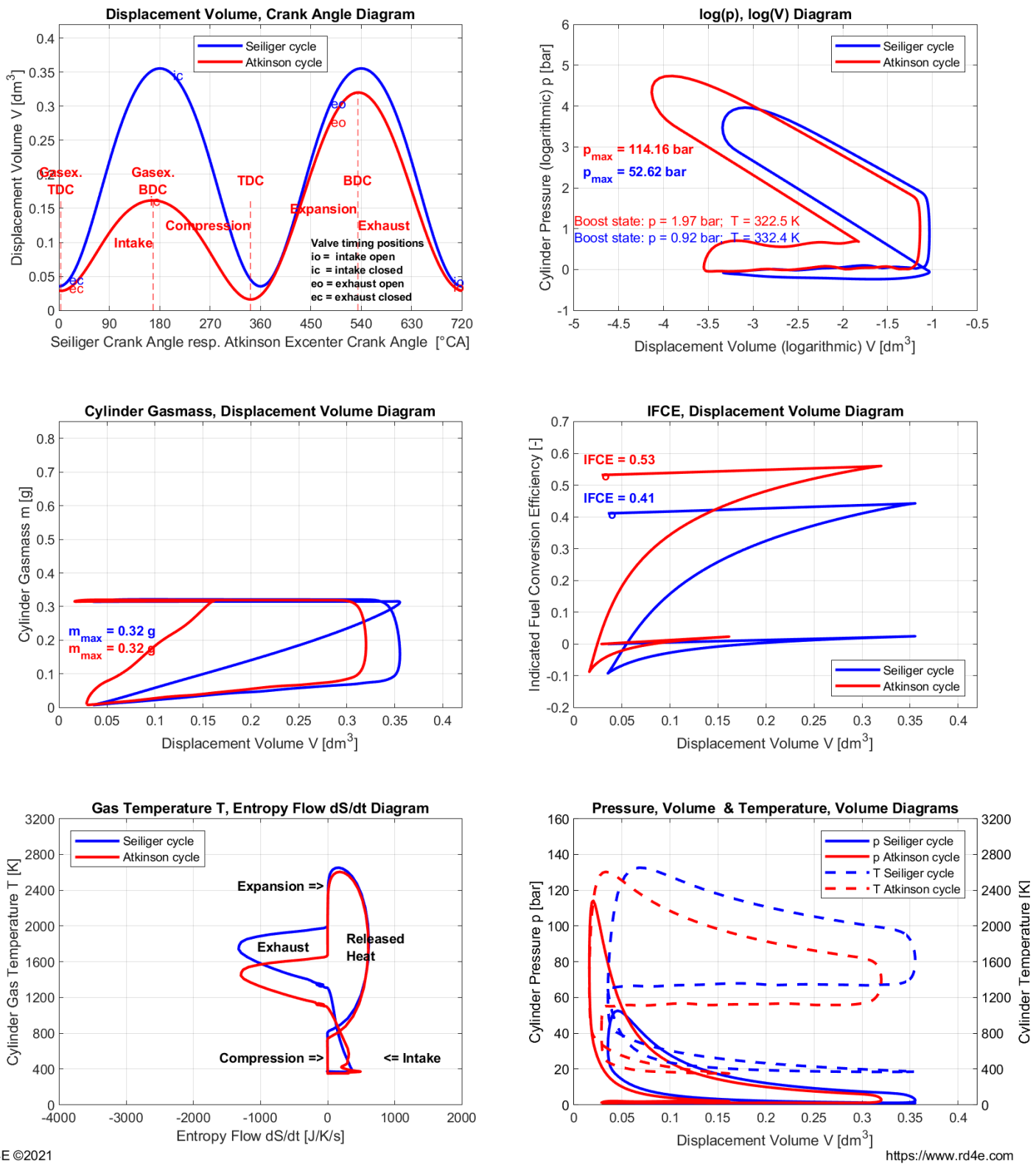

Figure A2-EOP-05. Simulation results of the true Atkinson and the Seiliger cycles by using the AVL BOOST tool. The Summary files for A & S are linked here, to examine all mean values of the simulation parameters.

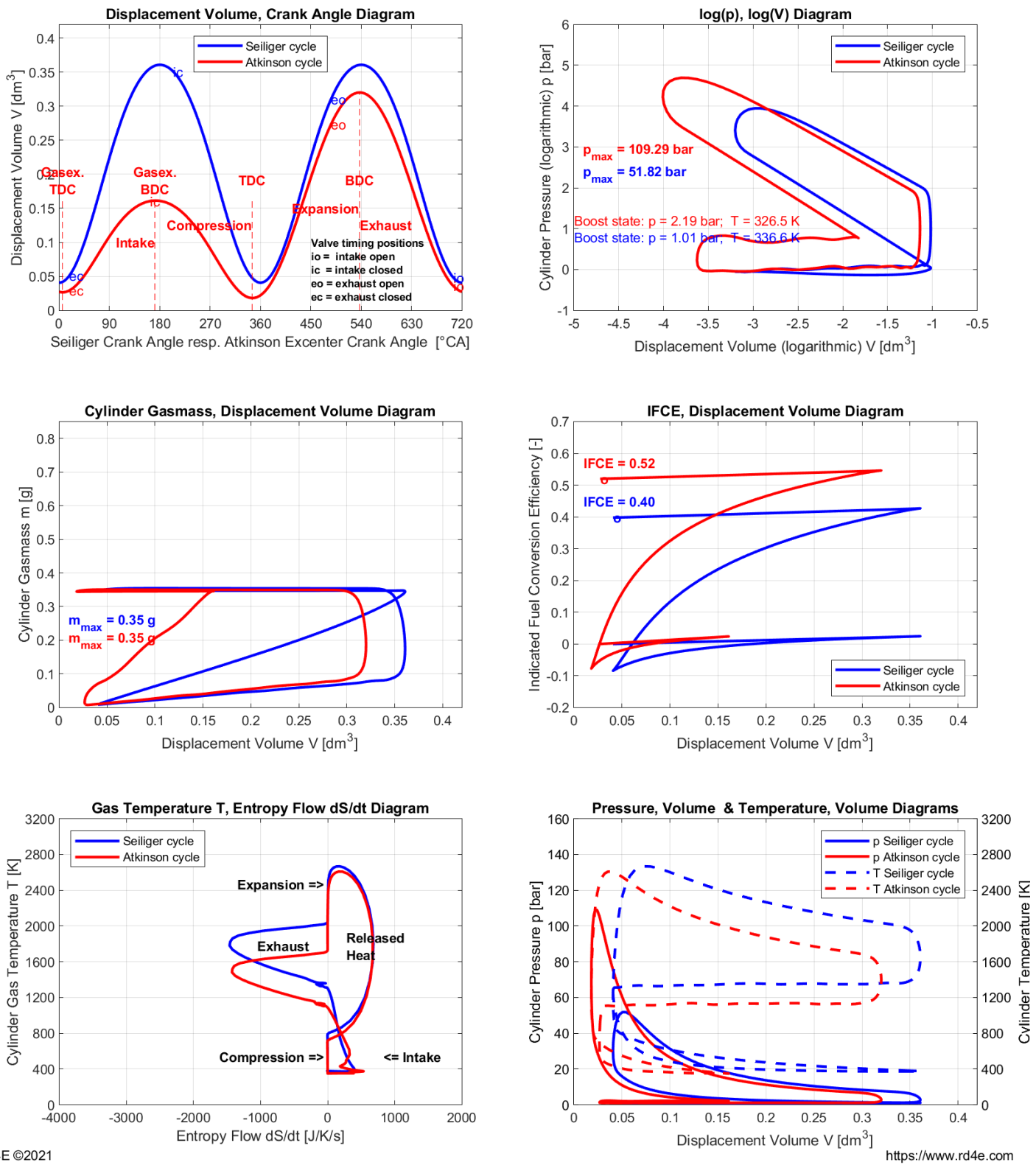

Figure A2-EOP-06. Simulation results of the true Atkinson and the Seiliger cycles by using the AVL BOOST tool. The Summary files for A & S are linked here, to examine all mean values of the simulation parameters.

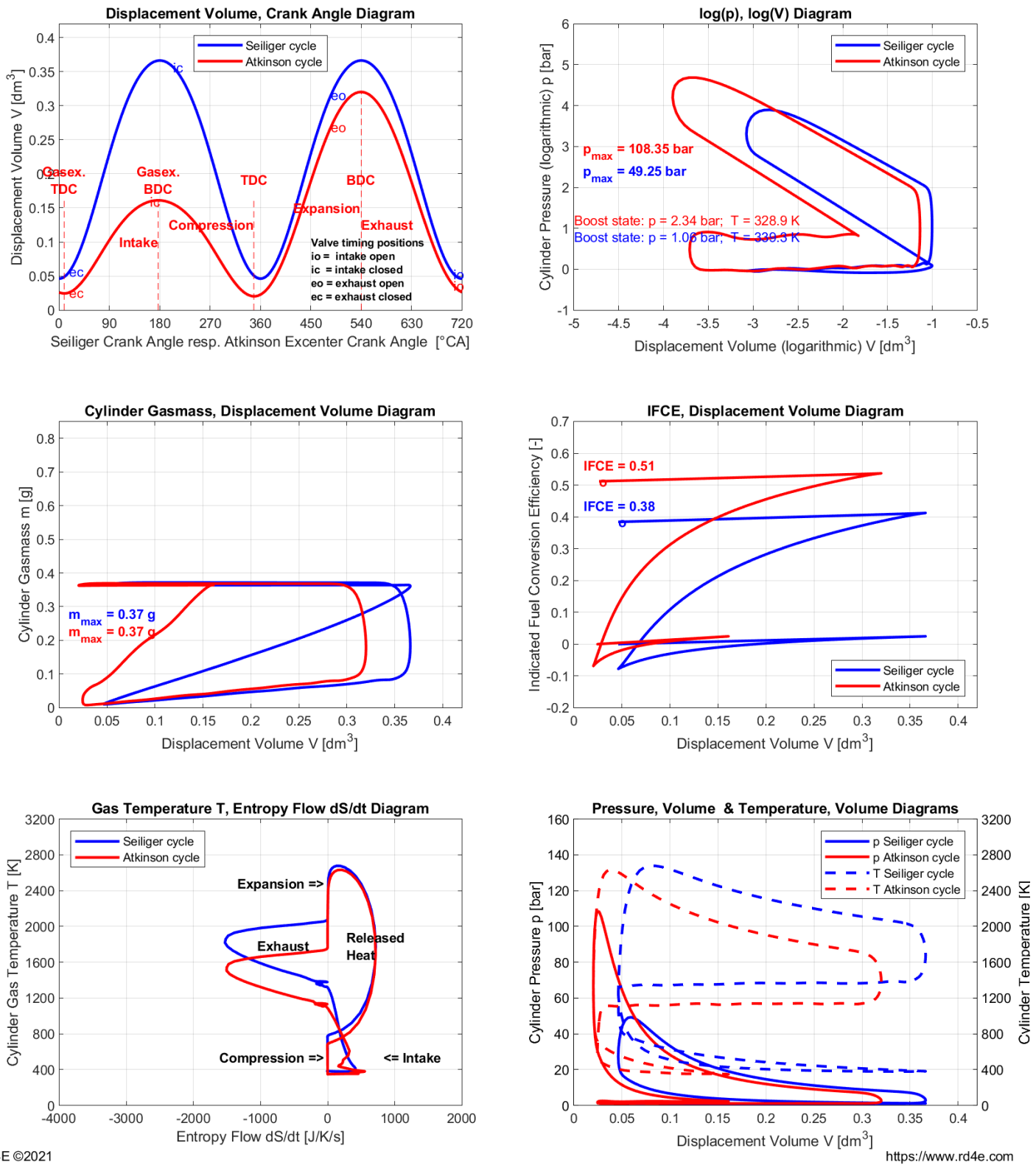

Figure A2-EOP-07. Simulation results of the true Atkinson and the Seiliger cycles by using the AVL BOOST tool. The Summary files for A & S are linked here, to examine all mean values of the simulation parameters.

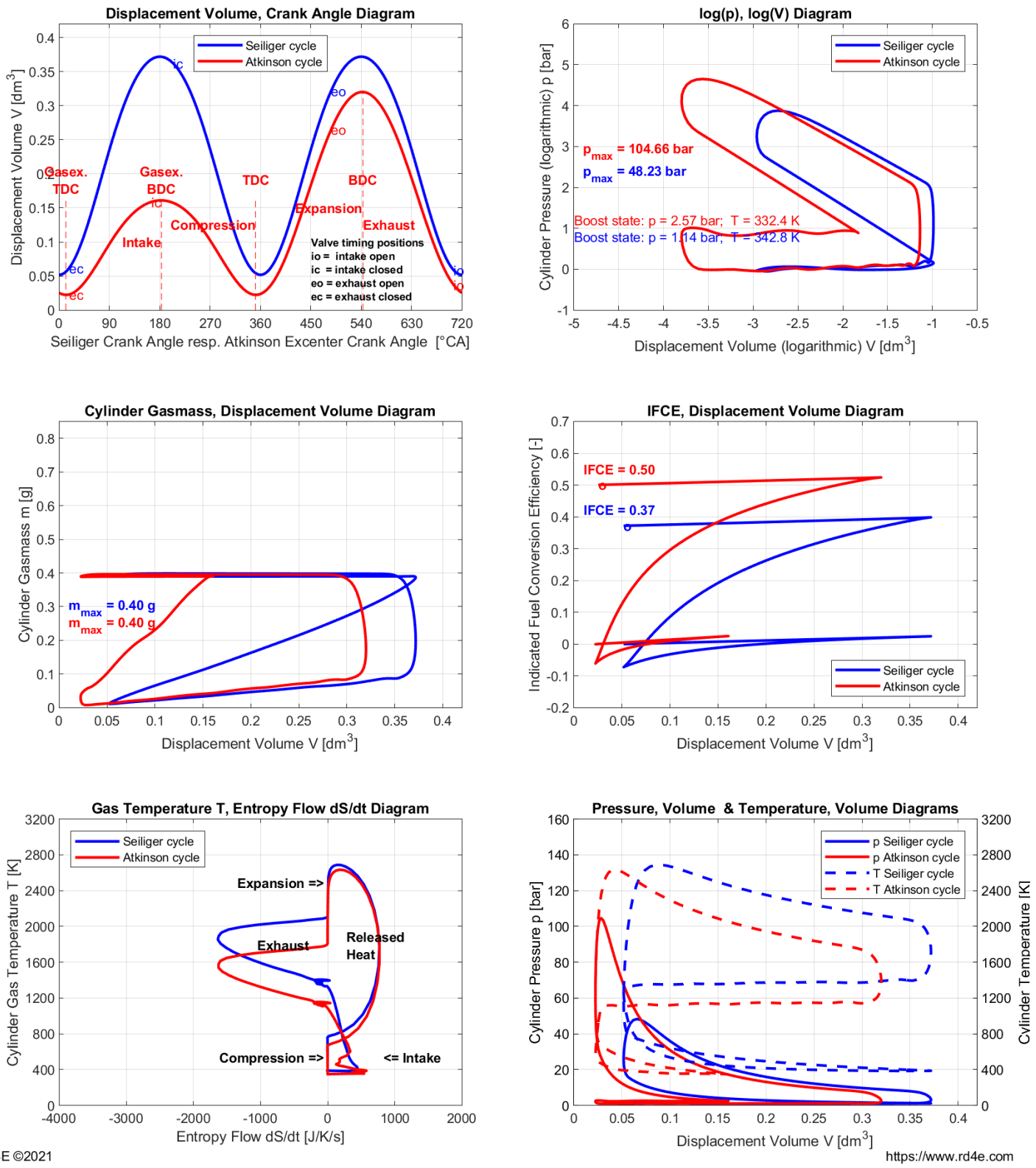

Figure A2-EOP-08. Simulation results of the true Atkinson and the Seiliger cycles by using the AVL BOOST tool. The Summary files for A & S are linked here, to examine all mean values of the simulation parameters.

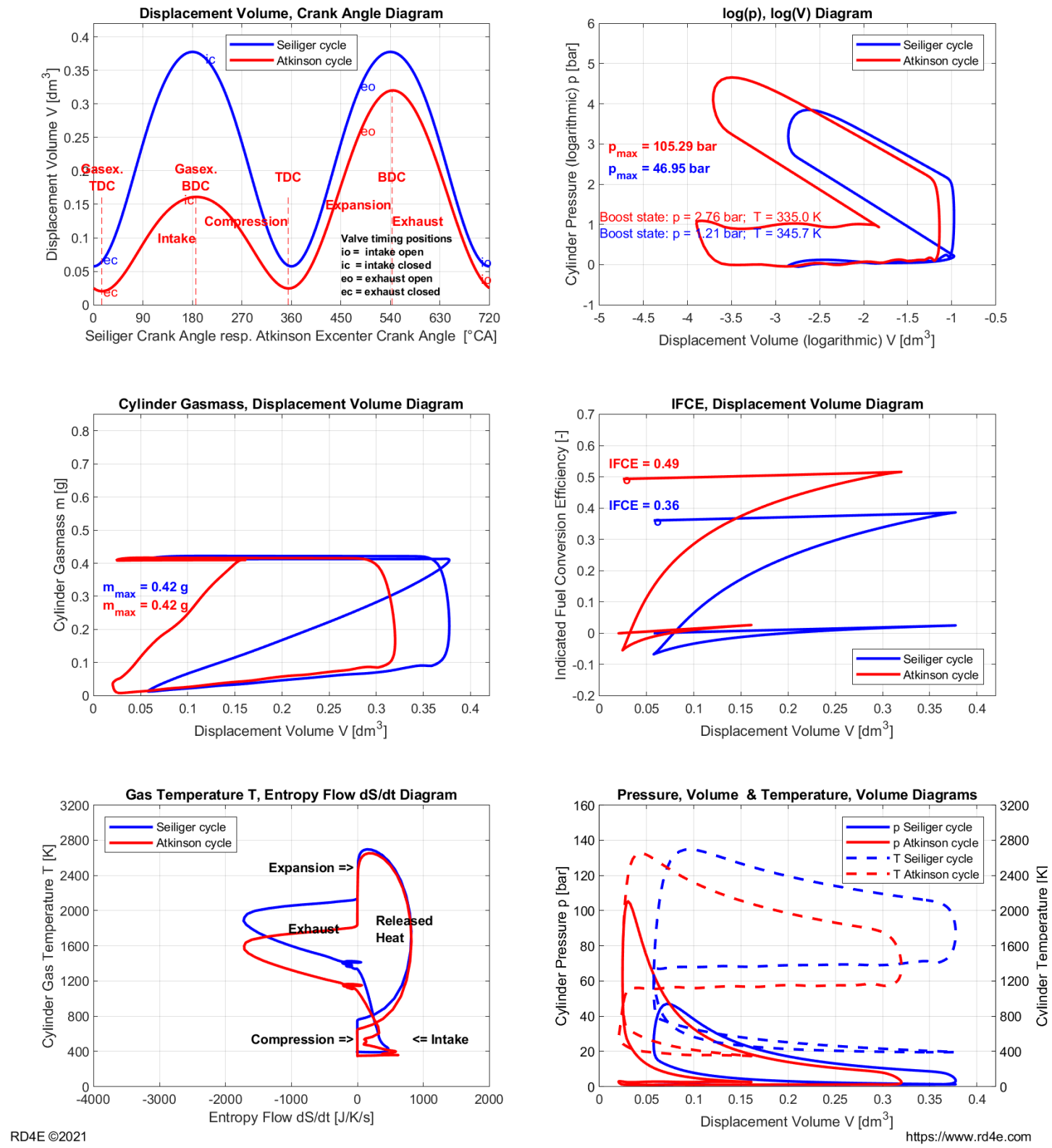

Figure A2-EOP-09. Simulation results of the true Atkinson and the Seiliger cycles by using the AVL BOOST tool. The Summary files for A & S are linked here, to examine all mean values of the simulation parameters.

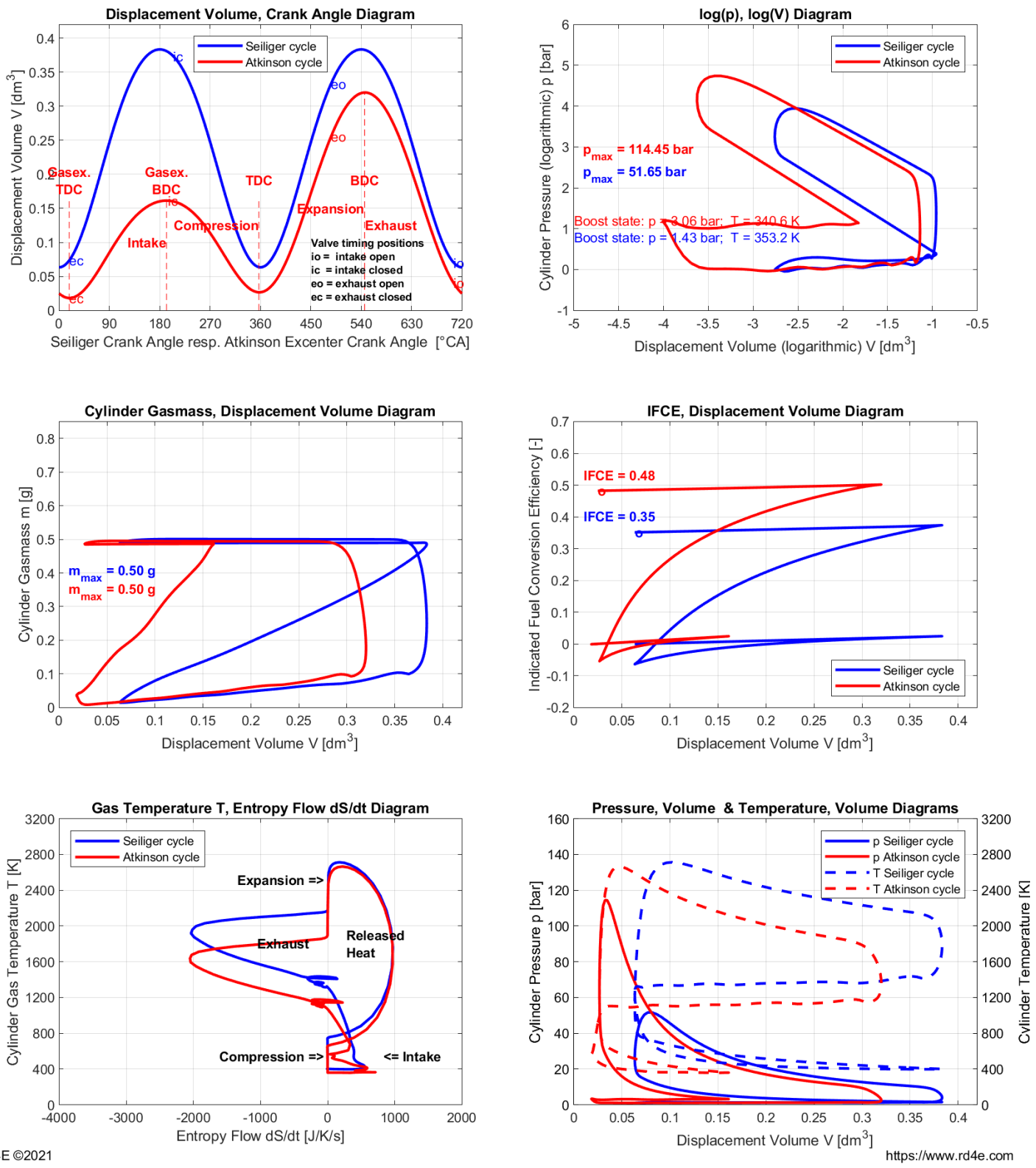

Figure A2-EOP-10. Simulation results of the true Atkinson and the Seiliger cycles by using the AVL BOOST tool. The Summary files for A & S are linked here, to examine all mean values of the simulation parameters.

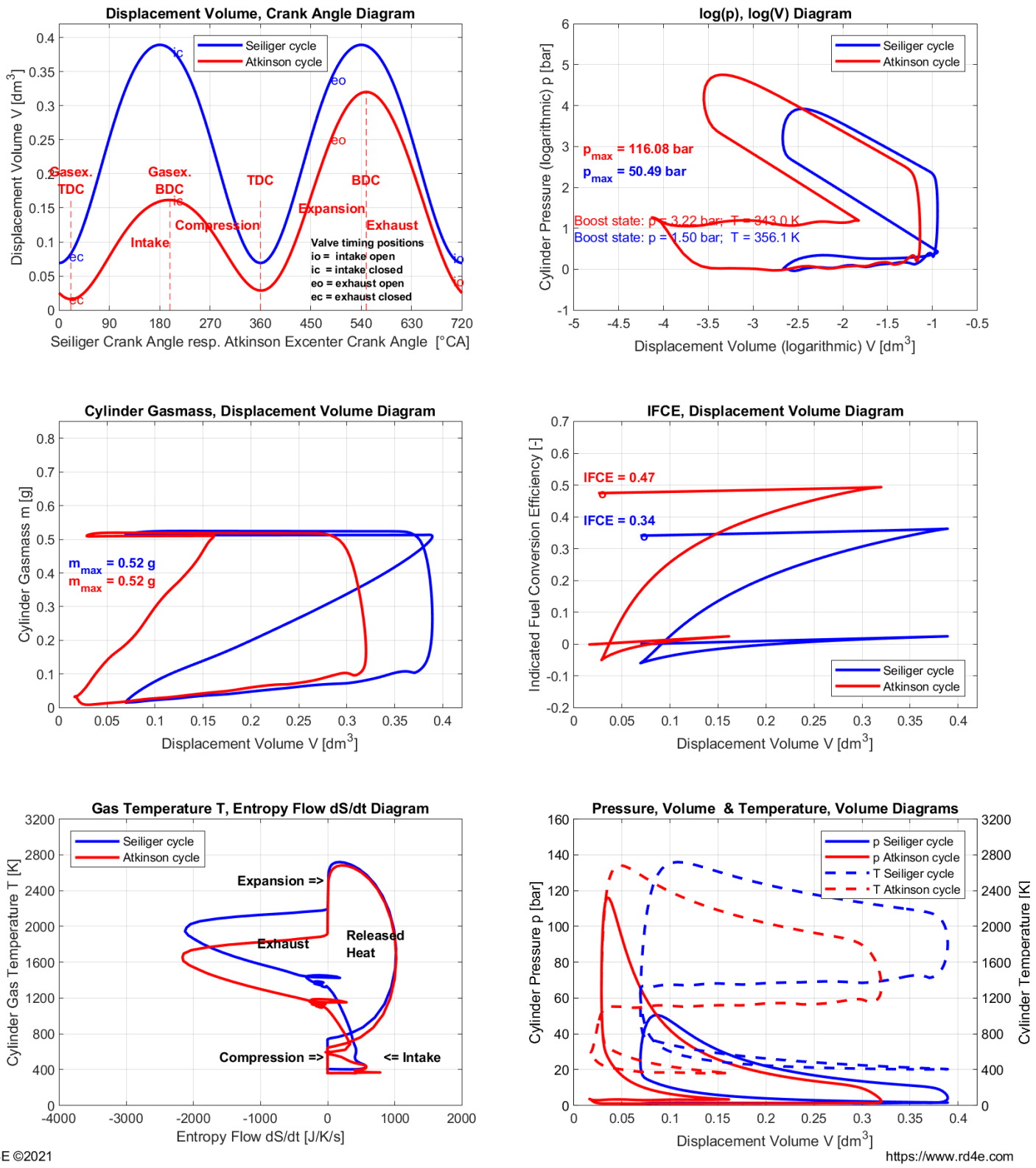

Figure A2-EOP-11. Simulation results of the true Atkinson and the Seiliger cycles by using the AVL BOOST tool. The Summary files for A & S are linked here, to examine all mean values of the simulation parameters.

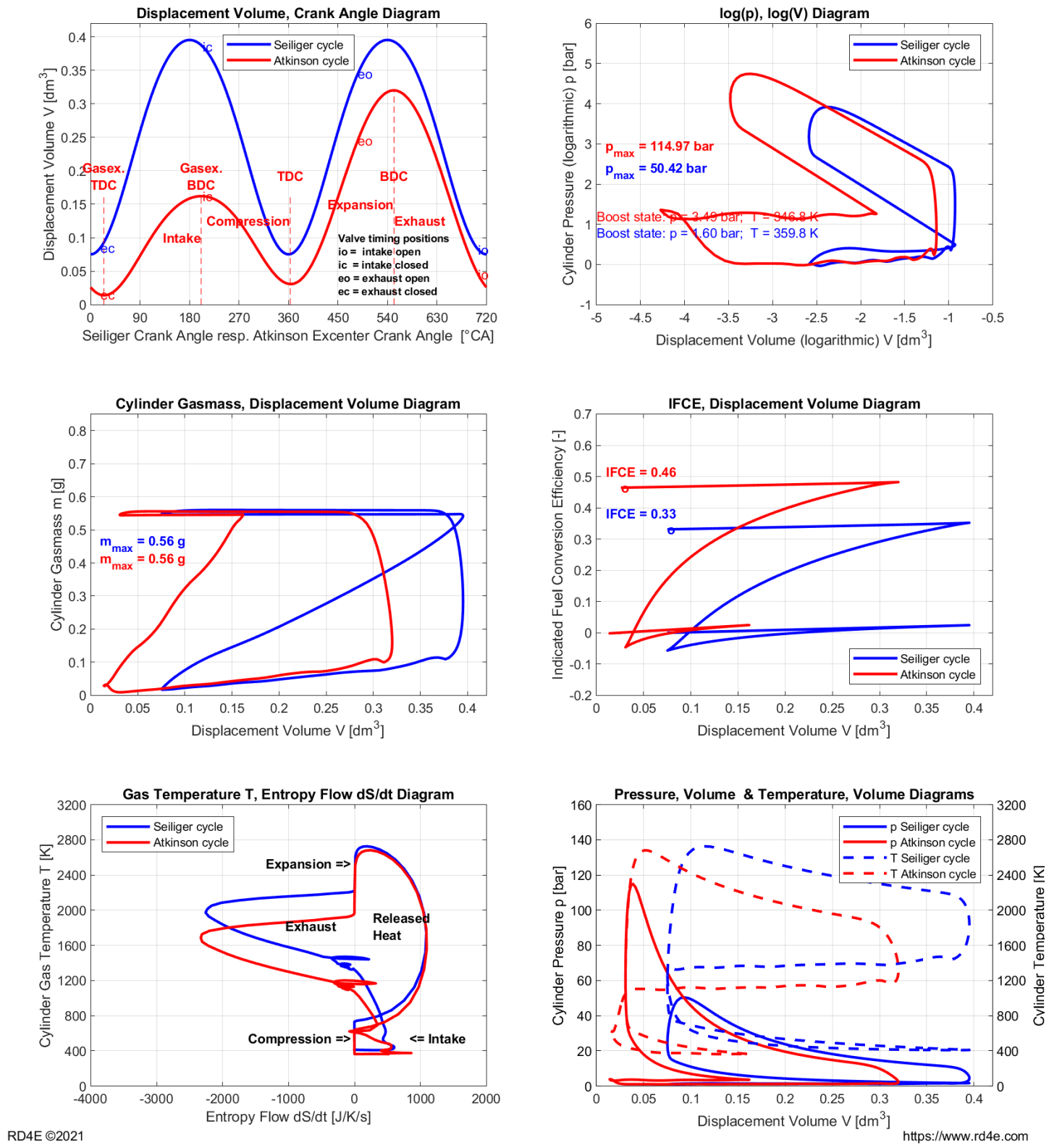

Figure A2-EOP-12. Simulation results of the true Atkinson and the Seiliger cycles by using the AVL BOOST tool. The Summary files for A & S are linked here, to examine all mean values of the simulation parameters.

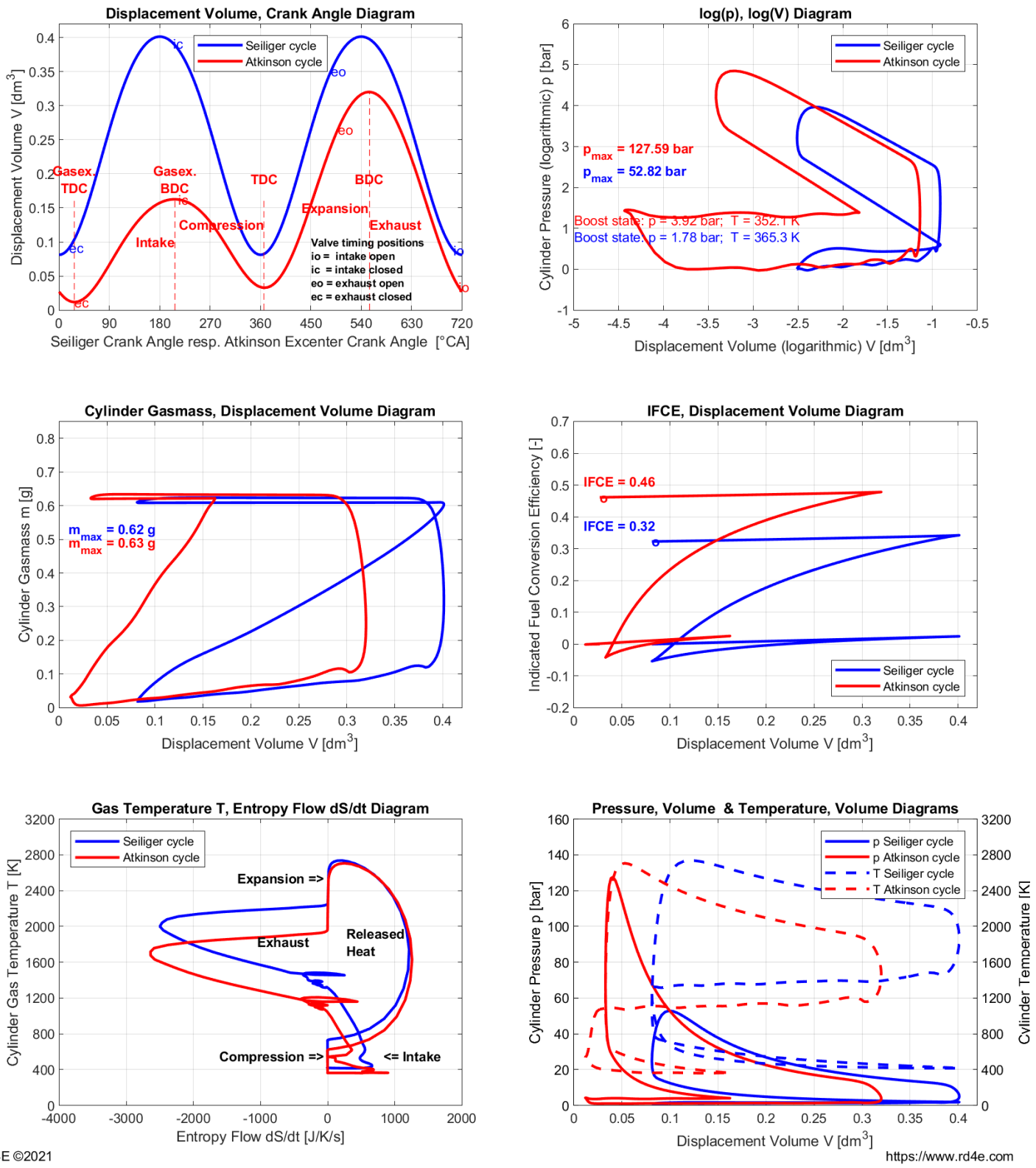

Figure A2-EOP-13. Simulation results of the true Atkinson and the Seiliger cycles by using the AVL BOOST tool. The Summary files for A & S are linked here, to examine all mean values of the simulation parameters.

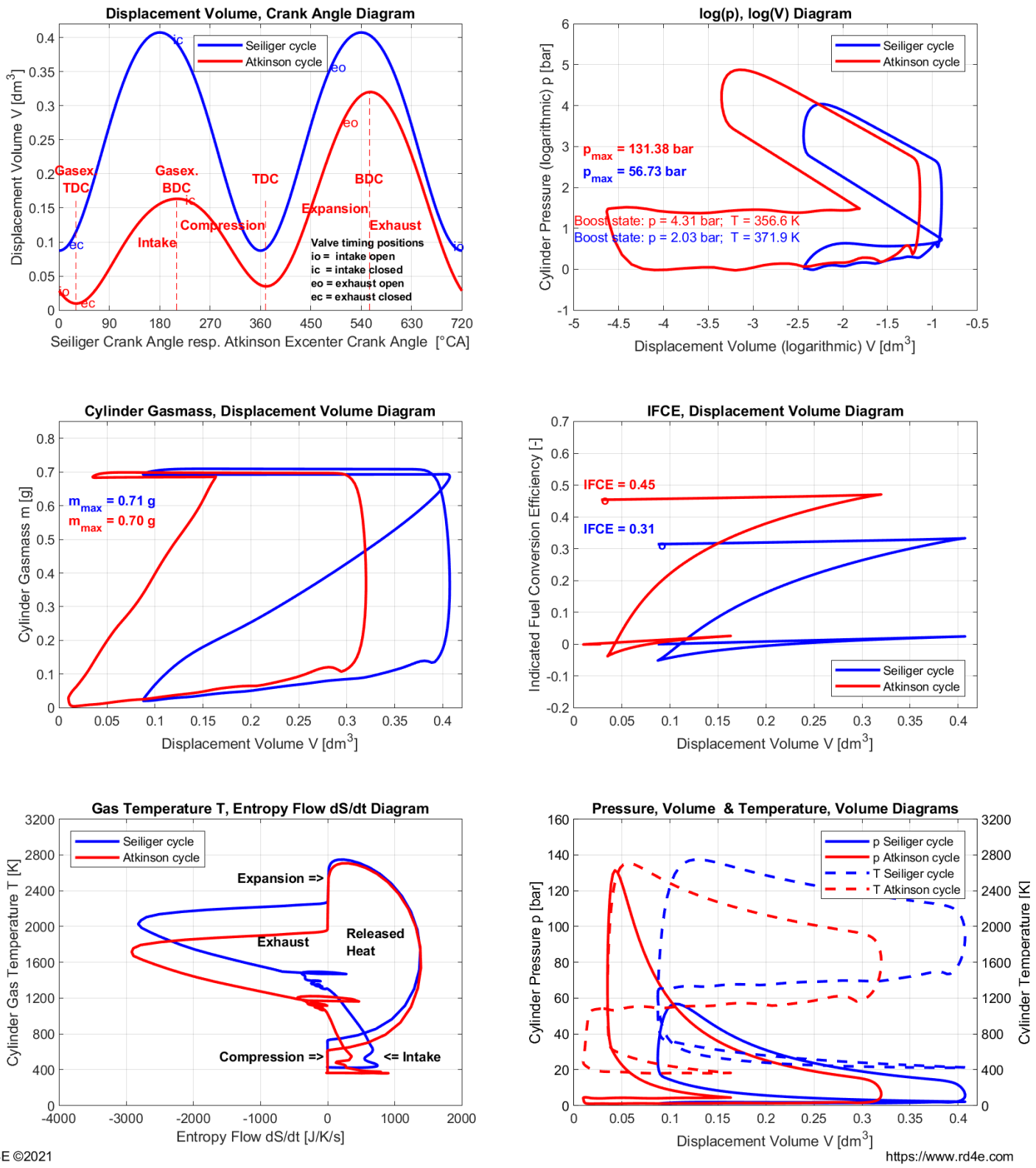

Figure A2-EOP-14. Simulation results of the true Atkinson and the Seiliger cycles by using the AVL BOOST tool. The Summary files for A & S are linked here, to examine all mean values of the simulation parameters.

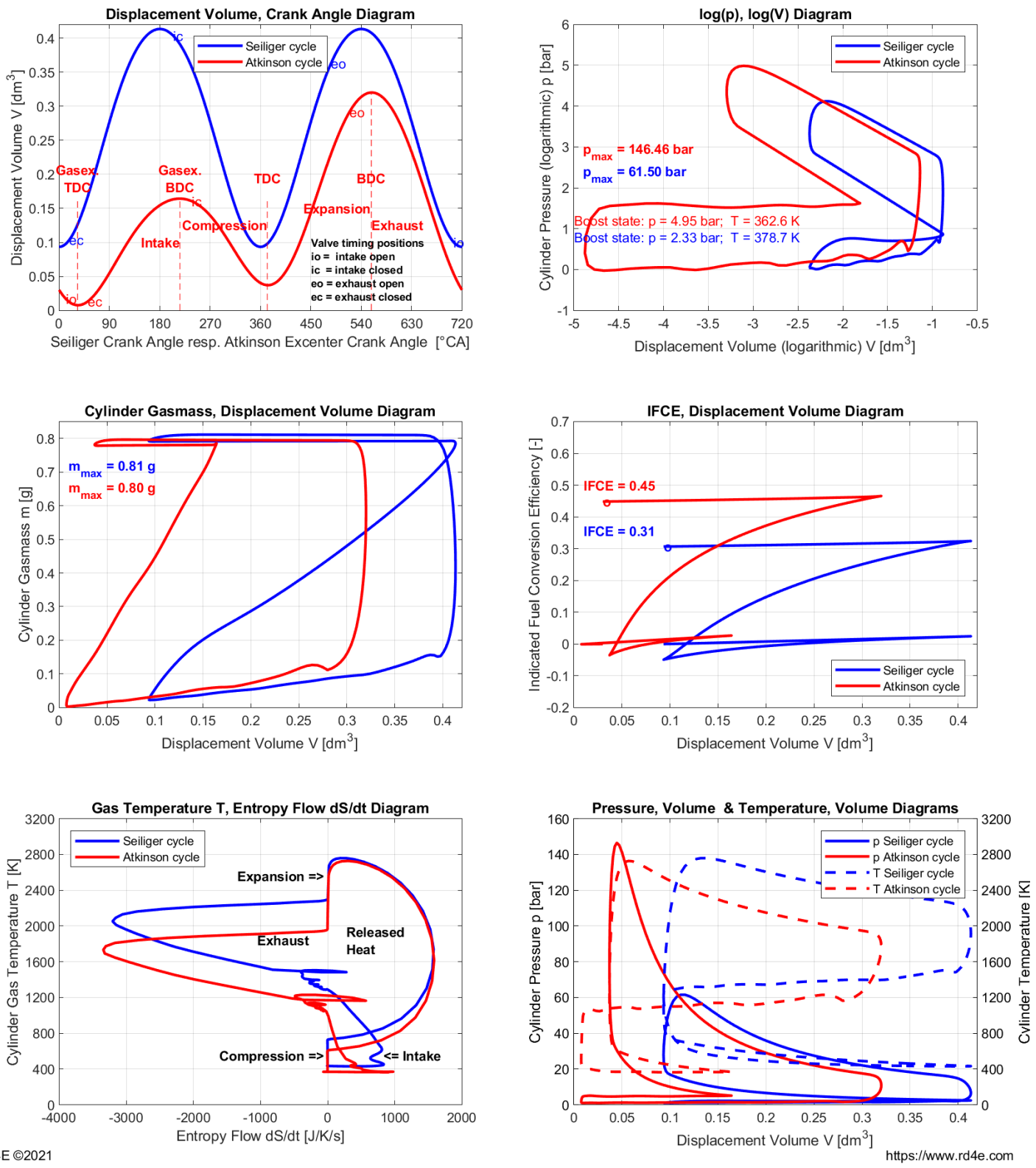

Figure A2-EOP-15. Simulation results of the true Atkinson and the Seiliger cycles by using the AVL BOOST tool. The Summary files for A & S are linked here, to examine all mean values of the simulation parameters.

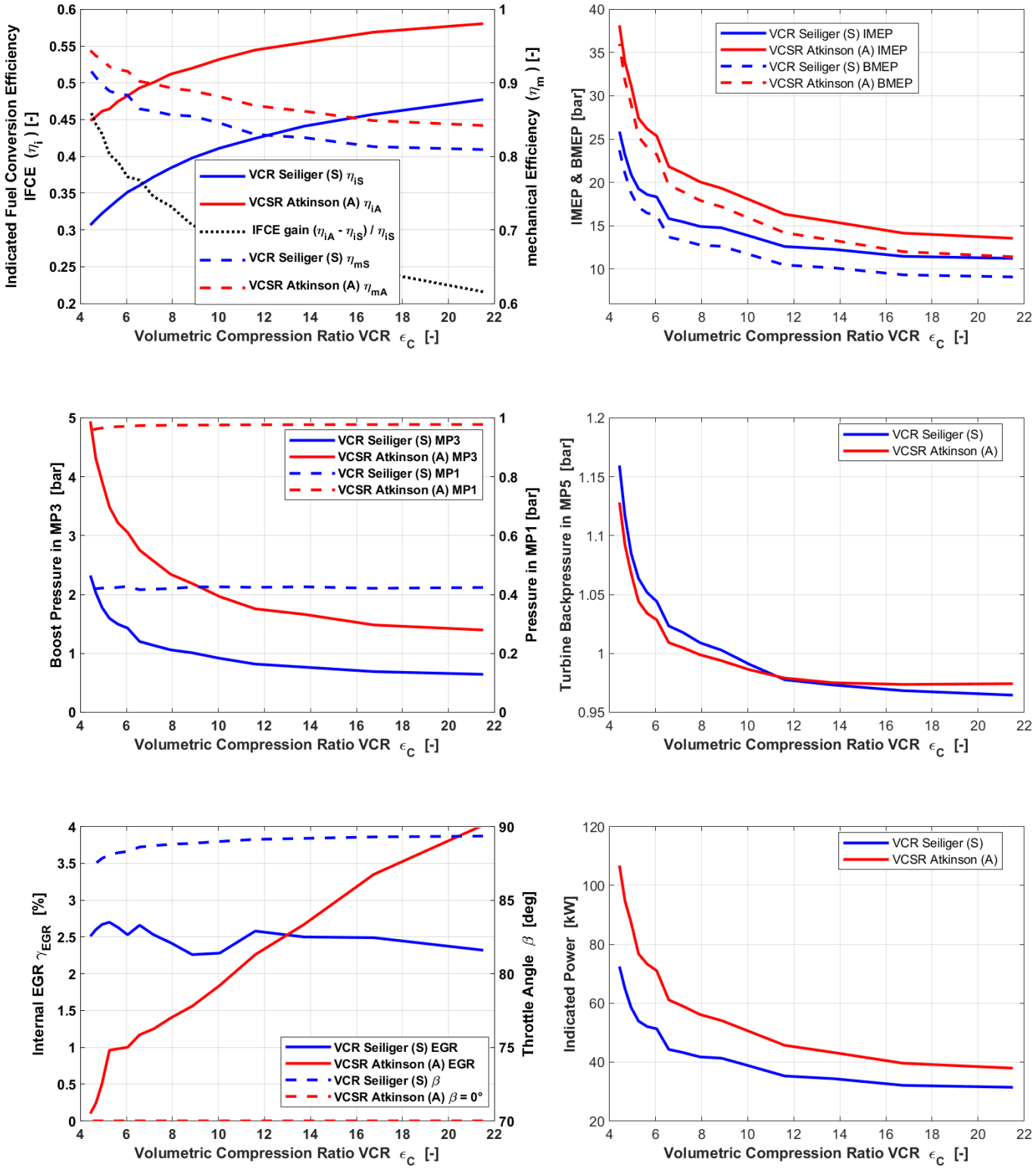

Figure A2-EOPs-01-15. Ultra Downsizing (UD) Load Control (LC) example

15th EOP, NONadiabatic & FMEP = 2.12 bar, H_2-fueled ICE, working according to Seliger and Atkinson cycles, with identical: VCR ϵ_C = 4.43, expansion stroke lengths & maximum gas mass, AFR λ = 1; γ of Atkinson cycle = 1.95 or 7° RG setting

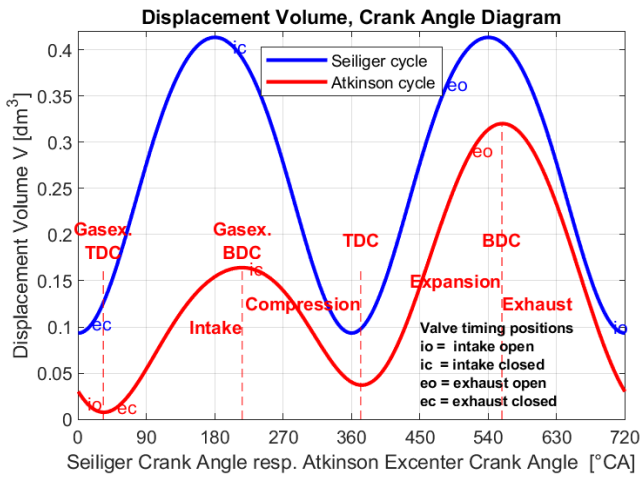

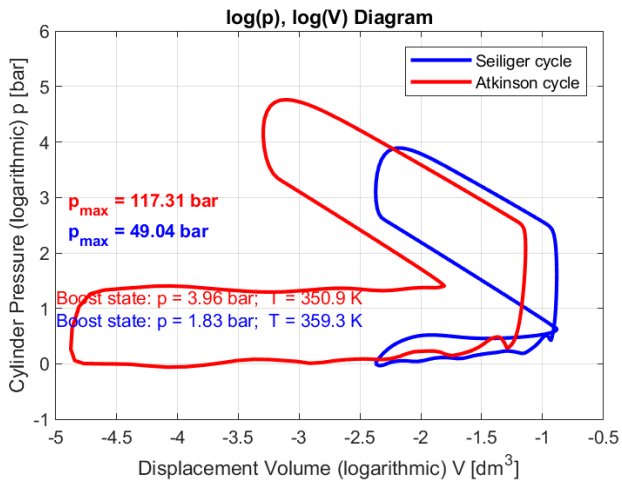

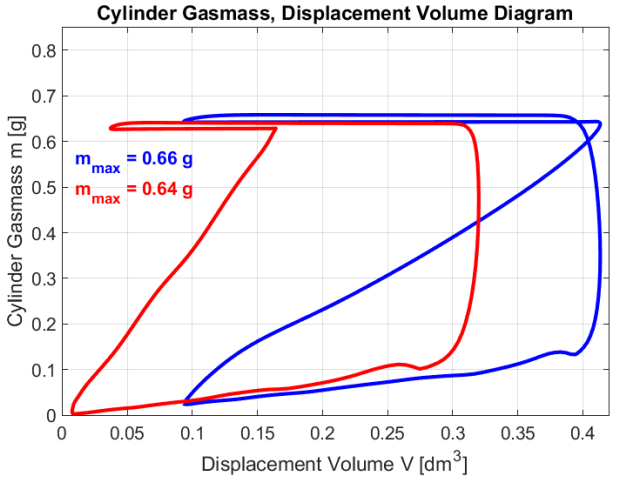

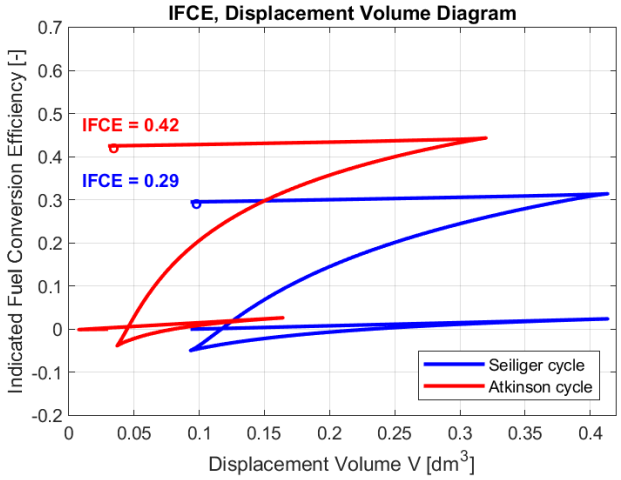

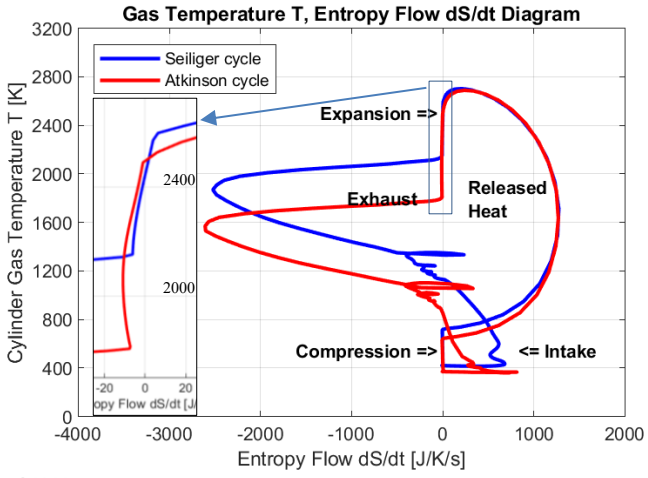

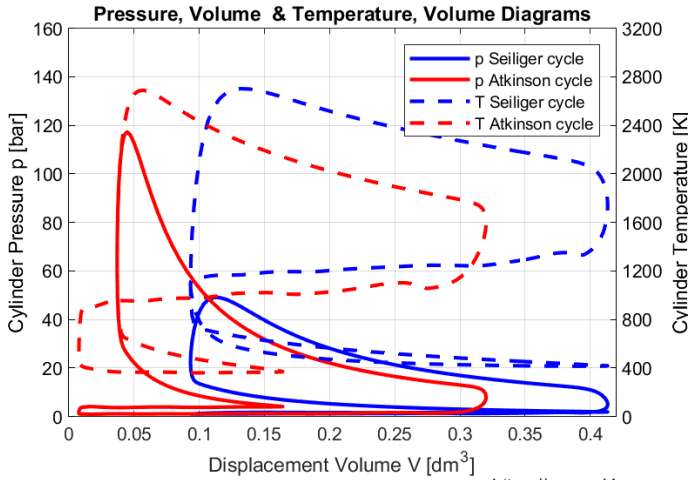

Figure A2-EOP-15_**nonad**. Simulation results of the true Atkinson and the Seiliger cycles by using the AVL BOOST tool. The Summary files for A & S are linked here, to allow the examination of all the mean values of the simulation parameters. The heat transfer in the cylinder energy balance of the A cycle in [%] is identical to that of the S cycle. The heat transfer model in AVL Boost used here is that of Bargende (a two zone model).

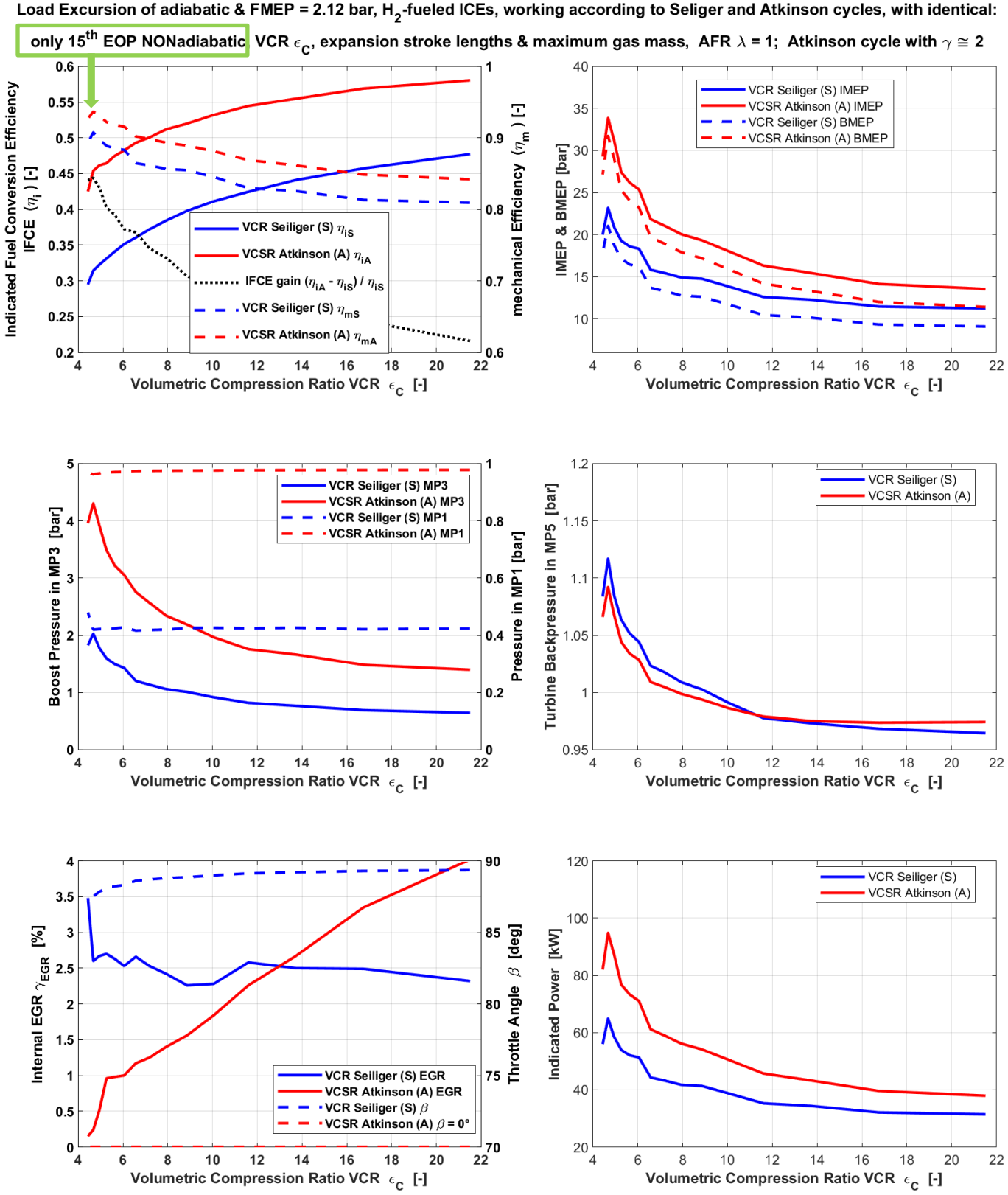

Figure A2-EOPs-01-15_nonad. Ultra Downsizing (UD) Load Control (LC) illustration. Exemplary only 15th EOP is nonadiabatic simulated here, whereby the heat transfer in the cylinder energy balance of the A cycle in [%] is identical to that of the S cycle. The 15th EOP can be used as reference and makes possible estimations of the heat transfer influence in the other EOPs as well. Further considerations about the heat transfer on the ICE with extended expansion can be found in [26].

Conclusion

A brief history of ICE development: A rule of thumb for engineers in the ICE area is:

1. From the energy released from the combustion of the fuel in the cylinder:
   I. A first third is delivered as mechanical work to the drive and determines the effective efficiency,
   II. A second third is dissipated as cooling heat into the environment and is completely lost,
   III. The last third is carried away with the exhaust gases and is almost completely lost. Only a small fraction is returned via turbocharging.
2. Since my college years, I have always tried to improve this classification of the released energy of the fuel on the side of mechanical work, and thus of the effective efficiency.
3. In the 1970 - 1980s, the R&D specialists in ICE, especially from the USA, tried to reduce the second third by building adiabatic ICEs. The aim was to convert this second third mainly into mechanical work. The efforts to coat all the inner parts of the cylinder with ceramic were enormous. The oil lubrication should also have been replaced by a possible gas lubrication due to the excessively high temperatures of the components, which ultimately did not work out.
4. In 1975, in my diploma thesis, by simulating the ICE cycle processes, I proved that the building adiabatic ICE only makes a small contribution to increasing the degree of efficiency. The energy saved on the cooling side does not move - as hoped - to the first third, but mostly to the last third, which is not the desired outcome. This means that the exhaust gases are exhausted at a much higher temperature, while the efficiency, on the other hand, hardly improves. The result not only surprised me as an inexperienced young engineer, but also my supervisor and later my doctoral supervisor.
5. From the last third, i.e. the enthalpy of the exhaust gases, only a small fraction can be recovered via turbocharging. The classic design of the ICE did not allow for better results because the excessive increase in the cylinder temperature and pressure pushed the thermal and mechanical loads on the engine components above safety threshold. As a result, the engineers have limited the degree of turbocharging, via either Waste Gate, VTG or Miller and quasi Atkinson cycles (see [25] for details).
6. All measures listed in 5. as solutions to limiting the thermal and mechanical loads aim to dissipate a large part of the enthalpy of the exhaust gases into the environment without making use of it. Miller and quasi Atkinson do not have any efficiency advantages (see also [2] and [25]). Any additional unnecessary movement of the gas mass in the cylinder reduces the efficiency. This was clearly recognized (i.e. by approx. 10% improvement) when the automotive industry switched from pre-chamber engines to direct injection engines.
7. The direct consequence of these attempts is: the pre-compression of the air in the turbochargers must be fully utilized in order to achieve real heat recovery. This means that the compression in the cylinder should only start from this pre-compression state, i.e. the unnecessary part of the pre-compression as a piston stroke must be omitted and the VCR should be variably adjustable. More details about are presented in Appendix 1.
8. The VCSR crank drive and the Ultra Downsizing UD Load Control LC emerged as solutions to the facts described above after many years of research. With these improvements to the ICE, it is possible for the first time to achieve large amounts of heat recovery from the enthalpy of the exhaust gases. Only in this constructive and operational variant would an **adiabatic** building of the ICE really make sense.

The comparison of the presented simulation results from the figures:

a) A2-EOP-15 and A2-EOP-15_nonad (nonadiabatic) and
b) A2-EOPs-01-15 and A2-EOPs-01-15_nonad

shows by way of example and clearly in the 15th EOP what and how much can be recovered from the saved cooling heat and the enthalpy of the exhaust gases via the VCSR UD LC solution.